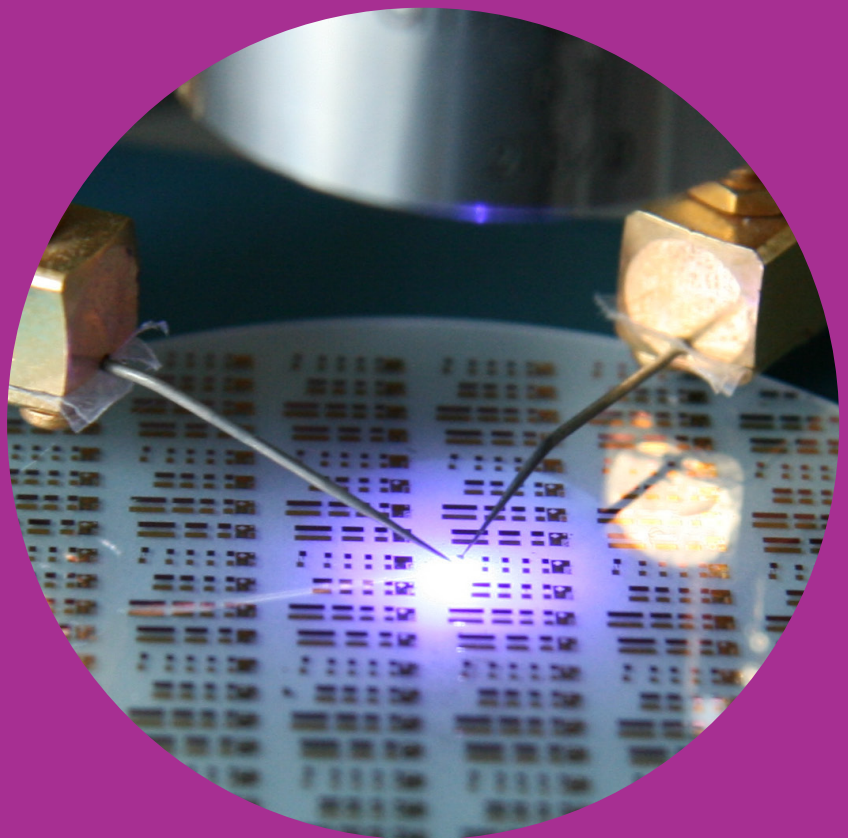


From computational models to improved light-emitting diodes and new devices

Pyry Kivisaari



From computational models to improved light-emitting diodes and new devices

Pyry Kivisaari

A doctoral dissertation completed for the degree of Doctor of Science (Technology) to be defended, with the permission of the Aalto University School of Science, at a public examination held at the lecture hall M232 of the main building of Aalto University on the 10th of December 2014 at 12.

Aalto University
School of Science
Department of Biomedical Engineering and Computational Science

Supervising professor

Jukka Tulkki

Thesis advisor

Dr. Jani Oksanen

Preliminary examiners

Prof. Seppo Honkanen, University of Eastern Finland

Prof. Dr. Mackillo Kira, Philipps-Universität Marburg, Germany

Opponent

Dr. Joachim Piprek, NUSOD Institute, USA

Aalto University publication series

DOCTORAL DISSERTATIONS 198/2014

© Pyry Kivisaari

ISBN 978-952-60-5991-4 (printed)

ISBN 978-952-60-5992-1 (pdf)

ISSN-L 1799-4934

ISSN 1799-4934 (printed)

ISSN 1799-4942 (pdf)

<http://urn.fi/URN:ISBN:978-952-60-5992-1>

Unigrafia Oy

Helsinki 2014

Finland



Author

Pyry Kivisaari

Name of the doctoral dissertation

From computational models to improved light-emitting diodes and new devices

Publisher School of Science**Unit** Department of Biomedical Engineering and Computational Science**Series** Aalto University publication series DOCTORAL DISSERTATIONS 198/2014**Field of research** Computational Engineering**Manuscript submitted** 8 September 2014**Date of the defence** 10 December 2014**Permission to publish granted (date)** 18 November 2014**Language** English **Monograph** **Article dissertation (summary + original articles)****Abstract**

The rapid evolution of III-Nitride light-emitting diodes (LEDs) has started a solid-state lighting revolution leading to dramatic improvements in the efficiency of lighting and enabling a significant reduction in global energy consumption. Despite the progress, the operation of commercial LEDs can still be notably increased if the remaining challenges related to LED efficiency and efficiency droop, i.e., the decrease in efficiency at high input powers in particular, are solved.

This thesis studies the factors affecting the performance of LEDs by using theoretical models and numerical simulations based on semiconductor transport equations and by analyzing measurement data and experiments. The main goal of the thesis is to generate new insight for understanding the present challenges of LED performance and for developing new device concepts for next-generation LEDs. The work has resulted, e.g., in the experimental demonstration of a fundamentally new current injection method, new insight on the droop mechanisms and current transport losses in LEDs, and better understanding of the potential benefits of polarization doping in LEDs.

Results of this thesis can be used to design LEDs with higher efficiency and decreased droop, to develop next-generation LEDs that better exploit the possibilities offered by large light-emitting surfaces and nanowire light emitters, and to reduce transport losses in LEDs to improve carrier spreading and reduce the operating voltage.

Keywords light-emitting diodes, efficiency droop, numerical simulation, device physics**ISBN (printed)** 978-952-60-5991-4**ISBN (pdf)** 978-952-60-5992-1**ISSN-L** 1799-4934**ISSN (printed)** 1799-4934**ISSN (pdf)** 1799-4942**Location of publisher** Helsinki**Location of printing** Helsinki**Year** 2014**Pages** 183**urn** <http://urn.fi/URN:ISBN:978-952-60-5992-1>

Tekijä

Pyry Kivisaari

Väitöskirjan nimi

Laskennallisista malleista paranneltuihin ledeihin sekä uusiin fotonikkakomponentteihin

Julkaisija Perustieteiden korkeakoulu**Yksikkö** Lääketieteellisen tekniikan ja laskennallisen tieteen laitos**Sarja** Aalto University publication series DOCTORAL DISSERTATIONS 198/2014**Tutkimusala** Laskennallinen tekniikka**Käsikirjoituksen pvm** 08.09.2014**Väitöspäivä** 10.12.2014**Julkaisuluvan myöntämispäivä** 18.11.2014**Kieli** Englanti **Monografia** **Yhdistelmäväitöskirja (yhteenvedo-osa + erillisartikkelit)****Tiivistelmä**

III-V-ryhmän nitrideihin perustuvien ledikomponenttien kehitys on mahdollistanut niiden nopean yleistymisen valaistussovelluksissa. Tämä on johtamassa merkittäviin parannuksiin valaistuksen energiatehokkuudessa sekä mahdollistamassa globaalin energiankulutuksen vähentämisen. Nopeasta kehityksestä huolimatta kaupallisten ledien toimintaa voidaan vielä merkittävästi parantaa, jos haasteet niiden hyötysuhteessa ja erityisesti hyötysuhteen pienemisessä suurilla tehoilla saadaan ratkaistua.

Tämän väitöskirjan päätavoite on parantaa käsitystä nykyisten ledirakenteiden ongelmista ja kehittää uusia laitekonsepteja seuraavan sukupolven ledeille. Väitöskirjassa tutkitaan ledien toimintaan vaikuttavia tekijöitä teoreettisilla malleilla, niiden numeerisella ratkaisulla sekä kokeellisten tulosten analysoinnilla. Tutkimustyö on johtanut mm. perustavanlaatuisesti uuden virransyöttömenetelmän esittelemiseen ja sen toimivuuden todentamiseen kokeellisesti, parantuneeseen ymmärrykseen ledien hyötysuhteen tehoriippuvuudesta ja virrankuljetuksesta sekä uusiin käsityksiin polarisaatiolla seostettujen ledirakenteiden tarjoamista hyödyistä.

Väitöskirjan tuloksia voidaan käyttää apuna nykyisten ledien virrankuljetuksen ja -leviämisen tehostamisessa, niiden hyötysuhteen parantamisessa varsinkin suurta valotehoa vaativissa sovelluksissa sekä uuden sukupolven ledien kehitystyössä. Väitöskirjassa esitetyt uudet laitekonseptit voivat mahdollistaa esimerkiksi kirkkaasti säteilevien laaja-alaisten nanolankarakenteiden aiempaa paremman hyödyntämisen.

Avainsanat ledit, ledien hyötysuhde, numeerinen mallintaminen, komponenttifysiikka**ISBN (painettu)** 978-952-60-5991-4**ISBN (pdf)** 978-952-60-5992-1**ISSN-L** 1799-4934**ISSN (painettu)** 1799-4934**ISSN (pdf)** 1799-4942**Julkaisupaikka** Helsinki**Painopaikka** Helsinki**Vuosi** 2014**Sivumäärä** 183**urn** <http://urn.fi/URN:ISBN:978-952-60-5992-1>

Preface

This work has been carried out at the Department of Biomedical Engineering and Computational Science (BECS) of Aalto University. I would like to express my warmest gratitude to my thesis instructor, Dr. Jani Okanen, for the guidance, encouragement, and challenging projects throughout my doctoral studies. I am also extremely grateful to my supervisor, Professor Jukka Tulkki, for the supportive research environment and all the valuable advice, to Professor Harri Lipsanen for helpful discussions and encouragement, and to all my colleagues at Aalto, especially Toufik Sadi, Kimmo Säaskilahti, Teppo Häyrynen, Oskari Heikkilä, Lauri Rittanen, Sami Suihkonen, Mikko Partanen, Ville Saarikivi, and Teemu Laakso. My thanks also go to the IT section of BECS for letting my simulations run uninterrupted and to Eeva, Katja and Susanna for sorting out all my bureaucratic issues.

I carried out part of my doctoral research at the Solid State Lighting & Energy Electronics Center (SSLEEC) of the University of California, Santa Barbara (UCSB). I'm extremely grateful to Professors James Speck, Shuji Nakamura, and Steven DenBaars for this wonderful opportunity and the inspiring research environment at SSLEEC. Yukina Warner is gratefully acknowledged for helping me out with nearly everything at UCSB, and my big thanks also go to my colleagues in Santa Barbara, especially Siddha Pimputkar, Paul Von Dollen, Steven Griffiths, Thomas Malkowski, Andrew Espenlaub, Sooyoung Moon, Masao Kita, Robert Farrell, Sang Ho Oh, Karine Hestroffer, and Audrius Alkauskas.

I participated in Aalto University's 'Bit Bang' doctoral course for two consecutive years, first as a student and then as one of the course tutors. I'm indebted for all the learning and experience gained during the courses to Professors Yrjö Neuvo and Erkki Ormala and to all my other Bit Bang friends, especially Elina, Evgenia and Somaya, who also didn't want to

leave Bit Bang after just one year.

Thanks to all my friends in Dominante choir, conductor Seppo Murto in particular, for countless unforgettable experiences in vocal music during the last ten years.

Special thanks go to my closest friends and family, who provide the best life experiences and the most valuable support.

Otaniemi, November 18, 2014,

Pyry Kivisaari

This work has been supported financially by the Graduate School in Electronics, Telecommunications and Automation (GETA), Academy of Finland, Aalto University's Multidisciplinary Institute of Digitalisation and Energy (MIDE), Aalto Energy Efficiency Programme (AEF), Emil Aaltonen Foundation, Foundation for Technology Promotion (Tekniikan edistämissäätiö), Oskar Öflund Foundation, Ulla Tuominen Foundation, Walter Ahlström Foundation, and Jenny and Antti Wihuri Foundation.

Contents

Preface	i
Contents	iii
List of Publications	v
Summary of article contents	vii
Author's contribution	ix
Symbols and abbreviations	xi
1. Introduction	1
1.1 Background	1
1.2 Objectives & scope	2
1.3 Properties of III-N materials	3
1.3.1 Material growth and device fabrication	4
1.3.2 Atomic structure and built-in polarization	6
1.3.3 Bandstructure and electrical properties	7
1.4 State-of-the-art III-N LEDs	10
2. Modeling of III-Nitride optoelectronic devices	13
2.1 Semiclassical carrier transport	13
2.1.1 Boltzmann transport equation	14
2.1.2 Drift-diffusion model	14
2.1.3 Drift-diffusion model parameters	16
2.1.4 Monte Carlo model	18
2.2 Carrier scattering	21
2.2.1 Radiative interband scattering	21
2.2.2 Nonradiative recombination	27
2.2.3 Interband transitions in QWs	28

2.2.4	Intraband scattering	30
2.3	Efficiency of III-N LEDs	33
2.3.1	Efficiency definitions	34
2.3.2	Models for efficiency droop	35
3.	Results and discussion	39
3.1	Performance of typical III-N LEDs	39
3.1.1	Current transport in heterostructures	39
3.1.2	Measurement of internal efficiencies	46
3.1.3	Auger recombination, hot electrons and droop	51
3.2	Physics of new III-N devices	57
3.2.1	Current injection by bipolar diffusion	57
3.2.2	Polarization-doped LED structures	63
3.3	Discussion	67
3.3.1	Implications and future research	67
3.3.2	Reliability and accuracy of results	68
4.	Conclusions	69
	Bibliography	71
	Publications	81

List of Publications

This thesis consists of an overview and of the following publications which are referred to in the text by their Roman numerals.

I Pyry Kivisaari, Jani Oksanen, and Jukka Tulkki. Effects of lateral current injection in GaN multi-quantum well light-emitting diodes. *Journal of Applied Physics*, 111, 103120, May 2012.

II Pyry Kivisaari, Jani Oksanen, and Jukka Tulkki. Effects of direct lateral Current Injection on the Performance, Overall Efficiency and Emission Distribution in GaN LED structures: a 2D Computational Study. *MRS Proceedings*, 1370, June 2011.

III Pyry Kivisaari, Lauri Riuttanen, Jani Oksanen, Sami Suihkonen, Muhammad Ali, Harri Lipsanen, and Jukka Tulkki. Electrical measurement of internal quantum efficiency and extraction efficiency of III-N light-emitting diodes. *Applied Physics Letters*, 101, 021113, July 2012.

IV Pyry Kivisaari, Toufik Sadi, Jani Oksanen, and Jukka Tulkki. Monte Carlo–drift-diffusion simulation of electron current transport in III-N LEDs. *Proceedings of SPIE*, 8980, 898003, February 2014.

V Toufik Sadi, Pyry Kivisaari, Jani Oksanen, and Jukka Tulkki. On the correlation of the Auger generated hot electron emission and efficiency droop in III-N LEDs. *Applied Physics Letters*, 105, 091106, September 2014.

- VI** Pyry Kivisaari, Jani Oksanen, and Jukka Tulkki. Diffusion-assisted current spreading for III-nitride light-emitting applications. *Proceedings of SPIE*, 8625, 862528, February 2013.
- VII** Pyry Kivisaari, Jani Oksanen, and Jukka Tulkki. Current injection to free-standing III-N nanowires by bipolar diffusion. *Applied Physics Letters*, 103, 031103, July 2013.
- VIII** Lauri Riuttanen, Pyry Kivisaari, Henri Nykänen, Olli Svensk, Sami Suihkonen, Jani Oksanen, Jukka Tulkki, and Markku Sopanen. Diffusion injected multi-quantum well light-emitting diode structure. *Applied Physics Letters*, 104, 081102, February 2014.
- IX** Pyry Kivisaari, Jani Oksanen, and Jukka Tulkki. Polarization doping and the efficiency of III-nitride optoelectronic devices. *Applied Physics Letters*, 103, 211118, November 2013.
- X** Lauri Riuttanen, Pyry Kivisaari, Nikolai Mäntyoja, Jani Oksanen, Muhammad Ali, Sami Suihkonen, and Markku Sopanen. Recombination lifetime in InGaN/GaN based light emitting diodes at low current densities by differential carrier lifetime analysis. *Physica Status Solidi C*, 10, 327–331, March 2013.

Summary of article contents

Publications I and II investigate current transport and related losses that prevent ideal carrier spreading in the MQW regions of typical high-efficiency III-N LEDs. The publications discuss the origins of these losses and present an example structure to decrease them. Improved carrier spreading in MQW regions is shown to reduce the bias voltage required to operate the LED and to move the peak efficiency towards higher input powers. Albeit Publications I and II study very similar structures with differences only in the polarization and band offset parameters, there are significant differences in the resulting performance, highlighting that the phenomena observed in the papers are very sensitive to the material parameters.

Publication III demonstrates and investigates a method to estimate the internal quantum efficiency and extraction efficiency of III-N LEDs from an electroluminescence measurement. The method only requires a measurement of the external quantum efficiency near its peak and does not require low temperature measurements, simulations, or detailed information about the structure. The method is also applied to study the effect of growth conditions on the device efficiency.

Publications IV and V combine the Monte Carlo and drift-diffusion models and introduce a Monte Carlo–drift-diffusion model to study carrier transport in III-N LEDs. In the model, hole transport is described by the drift-diffusion model, while electrons are simulated with the Monte Carlo model. The Monte Carlo model is free from quasi-equilibrium approximations and therefore the MCDD model directly includes the physics of hot electrons, which are generated mainly through Auger processes and relaxed due to various intraband scattering processes. Publications IV and

V show that Auger recombination affects the LED efficiency through both nonradiative recombination and hot-electron leakage current, supporting the theory that Auger recombination is the major cause of the efficiency droop.

Publications VI and VII introduce and analyze a new current injection concept where electrons and holes are injected to light-emitting InGaN wires using bipolar diffusion. **Publication VIII** presents a successful experimental demonstration of bipolar diffusion for a planar III-N MQW LED. Once developed further, bipolar diffusion could enable, e.g., arbitrarily large unpierced emitting areas and efficient nanowire or plasmonic emitters. Large-area LEDs and LEDs based on nanowires and plasmonic gratings offer promising solutions, e.g., to decrease the efficiency droop of LEDs.

Publication IX analyzes current transport, recombination, and potential efficiency improvements in polarization-doped III-N QW LED structures where graded material layers are used instead of impurity doping. The potential benefits for LED structures discussed in the publication include large hole densities, decreased quantum-confined Stark effect and smaller efficiency droop through better electron-hole overlap. Polarization doping could be particularly advantageous when coupled to bipolar diffusion injection.

Publication X analyzes preliminary small-signal measurements in III-N MQW LEDs at small current densities to estimate carrier lifetimes. Estimating carrier lifetimes gives information about the nonradiative and radiative recombination processes, the capacitance of the LED heterostructure, and their dependence on the operating point.

Author's contribution

The author wrote the first draft for **Publications I, II, III, IV, VI, VII, and IX.**

The author performed all the calculations and analysis of the numerical results in **Publications I, II, VI, VII, and IX.**

The author performed all the calculations and analysis of the measurement data in **Publication III** and participated actively in the analysis of measurement results in **Publications VIII and X.**

The author designed the coupled Monte Carlo–drift-diffusion simulation model and performed the analysis and simulations in collaboration with Dr. Toufik Sadi in **Publications IV and V** and contributed actively to writing the manuscript for **Publication V.**

Symbols and abbreviations

III-N	III-Nitride
α	First-order nonparabolicity constant
α_P	Absorption coefficient
\hat{a}	Unit polarization vector
A	Shockley-Read-Hall recombination coefficient
A_0	Amplitude of the vector potential
A_{ar}	Active region area
A_{cv}	Einstein's spontaneous emission coefficient
A_p	p-contact area
A_{qw}	Cross-section area of a QW
A	Vector potential
AR	Active region
β	Second-order nonparabolicity constant
B	Net radiative recombination coefficient
B_{vc}	Einstein's absorption coefficient
B_{cv}	Einstein's stimulated emission coefficient
BTE	Boltzmann transport equation
χ	Lattice strain
c	Speed of light
C	Auger recombination coefficient
δ	Kronecker delta
d	Thickness of the active region
D	Electric displacement field
D_n	Diffusion constant of electrons
D_p	Diffusion constant of holes
η_{EQE}	External quantum efficiency
η_{EXE}	Extraction efficiency

η_{INJ}	Injection efficiency
η_{IQE}	Internal quantum efficiency
η_{RAD}	Radiative efficiency
η_{VTG}	Voltage efficiency
η_{WPE}	Wall-plug efficiency
ε	Permittivity
ε_0	Permittivity in vacuum
ε_r	Relative permittivity
e	Elementary charge
\mathcal{E}	Electric field
E	Energy
E_c	Conduction band edge energy
E^c	Energy of a conduction band state
E_{Fn}	Conduction band quasi-Fermi level
E_{Fp}	Valence band quasi-Fermi level
E_{ij}	Deformation potential tensor
E_v	Valence band edge energy
E^v	Energy of a valence band state
EBL	Electron blocking layer
EL	Electroluminescence
ϕ	Electrostatic potential
ϕ_{cn}	n th subband envelope wave function of the conduction band in a QW
ϕ_{vm}	m th subband envelope wave function of the valence band in a QW
f	Carrier distribution function
$\mathcal{F}_{1/2}$	Fermi integral of the order 1/2
$g(\hbar\omega)$	Gain
g_c	Density of states in the conduction band
g_r	Reduced density of states of the conduction and valence bands
g_v	Density of states in the valence band
$\mathcal{G}(\mathbf{k}_i, \mathbf{k}_f)$	Overlap factor between initial and final electron states
\hbar	Reduced Planck's constant
H	Hamiltonian
H', \mathcal{H}'	Perturbation Hamiltonian
\mathcal{H}'_{cv}	Perturbation matrix element of the conduction and valence band states

HVPE	Hydride vapor phase epitaxy
I	Injection current
I_{cv}	Overlap integral between conduction and valence band envelope wave functions
ITO	Indium tin oxide
J	Scalar current density
J_{leak}	Scalar leakage current density
\mathbf{J}_n	Electron current density
\mathbf{J}_p	Hole current density
k	Scalar wavenumber
\mathbf{k}	Wavevector
k_B	Boltzmann's constant
\mathbf{k}_f	Wavevector of the final state
\mathbf{k}_i	Wavevector of the initial state
\mathbf{k}_p	Photon wavevector
\mathbf{k}_t	Transverse wavevector
λ	Wavelength
L_{ar}	Distance between the active region and the edge of the depletion region
L_p	Distance between the p-contact and the edge of the depletion region
LED	Light-emitting diode
μ_n	Electron mobility
μ_p	Hole mobility
m_0	Electron mass
m^*	Scalar effective mass
m_c^*	Scalar effective mass for conduction band
m_r^*	Reduced effective mass
m_v^*	Scalar effective mass for valence band
MOVPE	Metalorganic chemical vapor deposition
MQW	Multi-quantum well
∇_k	Nabla operator with respect to wavevector
∇_r	Nabla operator with respect to position
n	Electron density

n_1	Electron density when the Fermi level coincides with a trap state
n_i	Intrinsic carrier concentration
n_p	Electron density at the edge of the p-type depletion region at zero bias
n_{ph}	Photon number
n_r	Refractive index
$N(\hbar\omega)$	Photon density of states
N_a	Ionized acceptor density
N_d	Ionized donor density
N_{op}	Phonon occupation number for optical phonons
N_q	Phonon occupation number for acoustic phonons
NWR	Freestanding nanowire emitter structure
ω	Angular frequency
Ψ_c	Wave function of a conduction band state
Ψ_v	Wave function of a valence band state
ψ	General solution to Schrödinger's equation
p	Hole density
p_1	Hole density when the Fermi level coincides with a trap state
p	Momentum operator
p_{cv}	Momentum matrix element of the conduction and valence band Bloch functions
P	Photocurrent density of an LED
P_m	Photocurrent density corresponding to maximum η_{EQE}
P_{out}	Optical output power
P _{pz}	Piezoelectric polarization
P _{sp}	Spontaneous polarization
P _{tot}	Total internal polarization
\mathcal{P}	Spectral intensity of light
PL	Photoluminescence
PSS	Patterned sapphire substrate
q	Phonon wavenumber
q	Phonon wavevector
QCSE	Quantum-confined Stark effect
QW	Quantum well
ρ	Material density

\mathbf{r}	Position vector
r_{ff}	Random number $\in (0, 1)$ used to generate free flights
r_s	Random number $\in (0, 1)$ used to select a scattering process
\mathbf{R}	Linear combination of lattice vectors
R	Net recombination rate density
R_{abs}	Spectral absorption rate density
R_{sp}	Spectral spontaneous emission rate density
R_{st}	Spectral stimulated emission rate density
\mathcal{R}_{nr}	Nonradiative recombination rate
\mathcal{R}_{rad}	Net radiative recombination rate
\mathcal{R}_{rec}	Net recombination rate
SRH	Shockley-Read-Hall
t	Time
t_{ff}	Free-flight time
T	Temperature
TFFC	Thin film flip-chip
TVJ	Transverse-vertical junction
$u_{n\mathbf{k}}$	Bloch function
$u_{c\mathbf{k}}$	Conduction band Bloch function
u_l	Longitudinal sound velocity
$u_{v\mathbf{k}}$	Valence band Bloch function
$U(\mathbf{r})$	Potential energy created by the crystal
$U_{ext}(\mathbf{r})$	External potential energy
\mathbf{v}	Velocity
\bar{v}	Average velocity
V	Volume
V_a	Applied voltage
W	Transition rate
W_{max}	Maximum transition rate
W_{ss}	Self-scattering rate
W_{tot}	Total scattering rate
ξ	Phonon polarization

1. Introduction

1.1 Background

Efficient use of energy plays a key role in decreasing the global dependence on fossil fuels and in enabling sustainable development. Effective harnessing of renewable energy is becoming increasingly feasible both due to technological development in production, storage, and high-efficiency use of energy, and due to long-term commitments of countries to reduce their emissions. For example, The European Union is committed to reducing greenhouse gas emissions to 80-95 % below the levels of 1990 by 2050. Both energy efficiency and renewable energy sources are expected to have a crucial role in reaching these goals [1]. Also, as an encouraging example, Germany has recently been able to cover more than 25 % of its quarter-year electricity demand [2] and almost 75 % of its temporary electricity demand [3] with a combination of solar, wind, hydro-, and bioenergy.

Photonics and optoelectronics offer some of the most promising and scalable solutions to low-carbon energy production and efficient energy use. The U.S. Department of Energy envisions solar energy to cover 14 % of the U.S. electricity needs by 2030 and 27 % by 2050 [4]. General lighting, on the other hand, accounts for around 16 % of the residential and commercial electricity use in the United States [5]. LED lighting is predicted to reduce the energy consumption of lighting in the US by 19 % and 46 % by 2020 and 2030, respectively. Even with the increasing global demand, the deployment of LEDs is expected to reduce the global electricity consumption of lighting [6]. LED lighting is already rapidly being adopted in lighting applications throughout the globe. In the US the market penetration of LEDs is predicted to more than triple by 2020 [6]. In China, the

market penetration of LEDs grew from 3.3 % to 8.9 % only between 2012 and 2013 [7].

Today's LED lamps predominantly use GaN-based LED chips emitting blue light that is converted to white light using yellow phosphors. The fast progress in p-type doping, material quality, InGaN multi-quantum well structures, and light extraction have made III-N LEDs the driving force of solid-state lighting, challenging all other lighting technologies [8–10]. Currently the best commercial LEDs reach wall-plug efficiencies of 75 % at normal operating conditions [11], and the price of high-quality LED chips is steadily decreasing. However, in order to meet the future projections for LED lighting, further improvements in the cost-effectiveness of these technologies are needed, calling for further breakthroughs in their material quality, efficiency, operation, and integration in general.

The most important bottleneck in further development of high-efficiency LEDs is presently their efficiency droop, i.e., the decrease of the efficiency from its peak value even in state-of-the-art LEDs when the input power is increased. The efficiency droop has been studied actively for almost ten years [12–28], and so far the only widely accepted general conclusion is that the droop has a monotonous dependence on the excess carrier density of the active region [29]. Most frequently the droop has been suggested to be caused by Auger recombination, different forms of electron leakage, and defect-related mechanisms.

1.2 Objectives & scope

This doctoral thesis aims at (1) generating sufficient physical insight to understand the main limitations of present-day LED structures, (2) developing new unconventional III-N light-emitting device solutions to improve the efficiency and functionality of LEDs, and (3) establishing and strengthening the collaboration between computational and experimental research groups. To reach these goals, operation of LEDs is studied using physical models that provide a good balance between being sufficiently detailed and realistic, yet relatively simple to implement and interpret. In addition to modeling, operation of LEDs is studied by analyzing and designing experiments and new devices.

Results obtained for conventional LEDs highlight the challenges of carrier spreading in multi-quantum well structures, provide characterization tools to measure internal parameters of LEDs, and provide detailed in-

formation about the relationship between Auger recombination and the efficiency droop. The results of this work mainly support the belief that Auger recombination is the fundamental cause of the efficiency droop, albeit many other factors affect the magnitude of the droop as well. This suggests that the most effective way to decrease the droop is by designing devices that operate closer to their optimal excess carrier densities than present-day state-of-the-art LEDs.

To improve the operation and efficiency of LED structures, new device concepts based on bipolar diffusion injection and polarization doping have been introduced and studied. Based on the computational and experimental results, bipolar diffusion may allow improving the efficiency by creating LEDs with very large emitting areas and improved nanostructure active regions. On the other hand, polarization doping is expected to provide small transport losses and reduced quantum-confined Stark effect due to improved electron-hole overlap, thereby enabling higher efficiency and smaller droop than present-day structures.

The work involves a close collaboration with experimentalists in the topics related to characterizing LEDs, comparing experimental results with theoretical models, and fabricating and testing new device structures based on the simulations. The physical models used in the thesis are frequently used to interpret and aid experimental work, and their validity is eventually only confirmed by comparing with experiments.

1.3 Properties of III-N materials

This Subsection briefly reviews the growth, atomic structure, and the most important physical properties of III-N materials and structures. This thesis focuses on structures grown using metalorganic vapor-phase epitaxy (MOVPE) either on sapphire or native GaN substrates, and therefore MOVPE and bulk GaN growth are reviewed briefly in Subsection 1.3.1. The wurtzite crystal structure of III-N materials and the resulting intrinsic polarization are described in Subsection 1.3.2. An overview of the electronic structure of III-Nitride materials is given in Subsection 1.3.3 to illustrate the effective mass approximation used in the drift-diffusion simulations and the nonparabolic dispersion relation used in the Monte Carlo simulations. Bandstructure is also needed to calculate rates for intra- and interband scattering, which are very relevant for device physics.

1.3.1 Material growth and device fabrication

III-N LED structures are typically grown on sapphire (Al_2O_3) or native GaN substrates using Metalorganic vapor phase epitaxy (MOVPE, also known as metalorganic chemical vapor deposition, MOCVD). Ideally, semiconductor materials are grown on native substrates as is the case for conventional III-V materials such as GaAs and InP. However, due to challenges in high-quality GaN substrate fabrication, sapphire, silicon or silicon carbide are commonly used as substrates in epitaxial growth of GaN [30].

MOVPE growth is based on using metalorganic precursors that contain the source materials needed for growing III-N structures. These precursors are kept in temperature controlled containers. A controlled flow of a carrier gas, typically hydrogen or nitrogen, flows through the containers and becomes saturated with the precursor materials. After being saturated with the precursor materials, the carrier gas flows further to the reactor chamber, where the substrate is kept in a high temperature. The precursor materials decompose and react in the vicinity of the heated substrate, resulting in the growth of a crystalline III-N material.

Traditionally III-N devices are fabricated on sapphire substrates. Due to the different lattice parameters between sapphire and GaN, the initial GaN layers have a low crystal quality and contain a high density of dislocations. Under suitable growth conditions, the defect density can be significantly reduced by growing a buffer layer that allows some of the defects to cancel each other [31]. The resulting crystal still has a relatively large density of dislocations, although this is typically not severely detrimental for device operation. On the other hand, high-quality growth on Sapphire is possible only in the crystal direction that has a very large intrinsic polarization. Due to these restrictions, III-N devices are increasingly grown on native GaN substrates, which are prepared with one of the bulk GaN growth techniques. The major techniques to grow bulk GaN substrates are hydride vapor phase epitaxy (HVPE), ammonothermal method, and solution growth techniques, mainly by using Na flux [32].

HVPE, also known as chloride transport chemical vapor deposition (CVD), is a very similar growth method as MOVPE. Similarly to MOVPE, in HVPE the Nitrogen atoms are transported to the growth chamber using ammonia. In contrast to MOVPE, however, the HVPE does not use met-

alorganic precursors to transport the Gallium atoms, but they are transported as gallium monochloride, which is formed by reacting HCl gas with Ga metal at 800-900 °C [33]. The substrate in HVPE is still typically foreign, e.g., SiC or sapphire, and it needs to be removed after growth. In comparison to MOVPE, HVPE allows much higher growth rates.

Another emerging technique to grow bulk GaN is the ammonothermal method that, unlike HVPE, takes place in a closed reactor under extremely high pressure of 100-400 MPa and controlled spatial temperature gradient around 500 °C. The basic ammonothermal method exploits the strong reduction of the solubility of GaN in basic solutions of ammonia under high pressure as the temperature increases [34]. A basic ammonothermal reactor has high-temperature and low-temperature regions. During growth, GaN dissolves from the source material (usually polycrystalline GaN) to the supercritical ammonia in the low-temperature region of the reactor. The low-temperature region is located above the high-temperature region so that due to its higher density, ammonia flows downward to the high-temperature region through gravitational forces, creating a continuous convective flow between the two regions. GaN is released and attached to the seed crystal due to the decreased solubility in the high-temperature region, and after releasing GaN, the heated ammonia flows upward to the low-temperature region, enabling a continuous growth process. The ammonothermal method is being studied actively to, e.g., develop high-quality GaN substrates with nonpolar or semipolar orientations [35]. Fig. 1.1 shows a sample of GaN grown at UCSB by the basic ammonothermal method using Na as mineralizer [36]. The sample was grown on an HVPE GaN substrate and later thinned and polished by the author to enable optical characterization.

In addition to HVPE and ammonothermal methods, recently also a liquid-phase Na flux growth method has gained considerable interest to enable growing large bulk GaN crystals [37]. Like the ammonothermal method, the Na flux method uses a closed reactor where GaN crystals are grown from solutions containing Na and Ga in a nitrogen gas environment. However, in contrast to the ammonothermal method, the Na flux growth takes place under a constant temperature around 850 °C and does not need pressures higher than approx. 5 MPa [38].

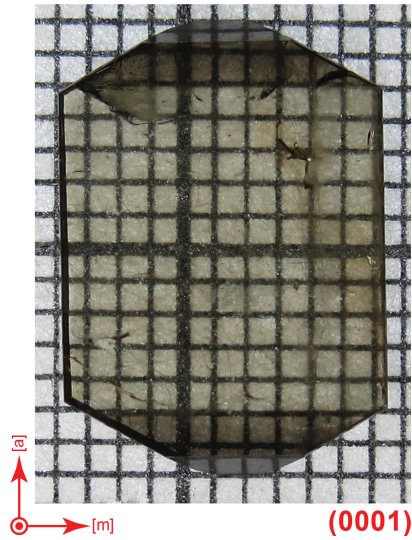


Figure 1.1. A sample of bulk GaN on a millimeter paper with a 1 mm grid size, grown with the basic ammonothermal method using Na as mineralizer. The sample was grown by Dr. Siddha Pimputkar and Mr. Steven Griffiths at University of California, Santa Barbara together with the author. The figure plane is the [0001] (or +c) plane, and perpendicular a- and m-plane vectors are also marked.

1.3.2 Atomic structure and built-in polarization

The growth methods described in the previous Subsection are typically used to grow wurtzite III-N materials, and only wurtzite III-N materials are studied in this thesis. Figure 1.2 shows an illustration of the wurtzite crystal structure of GaN together with the definitions of the a and c lattice constants and the [0001] crystal direction in Bravais-Miller notation. In this case the Ga-face side of the crystal points upward and grey balls represent Ga atoms.

Positions of the Ga and N sublattices relative to each other and ionicity of the bonds cause III-N materials to have a permanent spontaneous polarization aligned with the [0001] axis. Also when III-N materials with lattice mismatch (usually AlGa_xN or InGa_xN) are grown on GaN, their lattices deform to match the interatomic spacing of GaN in the heterostructure plane, resulting in strain. This introduces another polarization component known as piezoelectric polarization.

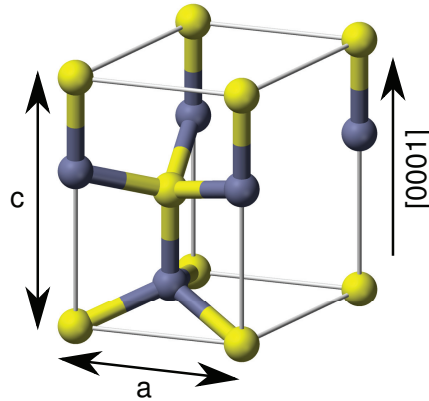


Figure 1.2. Illustration of the hexagonal wurtzite structure of GaN showing the lattice constants a and c and the $[0001]$ crystal orientation in Bravais-Miller notation (also often denoted $+c$ or Ga-face direction). In this case the material is Ga-polar and grey balls are Ga atoms. If grey balls are N atoms, the vector shows the $[000\bar{1}]$ direction (also denoted $-c$ or N-face direction). Positions of the Ga and N sublattices relative to each other and the ionicity of the bonds induce a permanent spontaneous polarization aligned with the $[0001]$ axis, and in strained structures the deformation of the crystal results in an additional piezoelectric polarization. Reprinted from Public Domain.

1.3.3 Bandstructure and electrical properties

The electronic states and the bandstructure of solid crystalline materials follow fundamentally from the well-known (see e.g. Ref. [39]) time-independent Schrödinger's equation, given by

$$\left(\frac{-\hbar^2}{2m_0} \nabla^2 + U(\mathbf{r}) \right) \Psi(\mathbf{r}) = E\Psi(\mathbf{r}), \quad (1.1)$$

where \hbar is the reduced Planck's constant, m_0 is the free-electron mass, $U(\mathbf{r})$ is the electrostatic potential energy created by the atomic structure of the material, \mathbf{r} is the position vector, Ψ is the wave function, and E is the eigenenergy. In ideal crystals, the potential energy $U(\mathbf{r})$ has the same periodicity as the underlying crystal, indicating $U(\mathbf{r}) = U(\mathbf{r} + \mathbf{R})$, where \mathbf{R} is any linear combination of the lattice vectors. It can be shown (see, e.g., Ref. [40]) that in this case the general solution is given by

$$\psi_{n\mathbf{k}}(\mathbf{r}) = \frac{1}{\sqrt{V}} \exp(i\mathbf{k} \cdot \mathbf{r}) u_{n\mathbf{k}}(\mathbf{r}), \quad (1.2)$$

where V is the volume of the crystal and $u_{n\mathbf{k}}(\mathbf{r})$ is a Bloch function for the wave vector \mathbf{k} and n th energy band. The Bloch function $u_{n\mathbf{k}}$ satisfies the $\mathbf{k} \cdot \mathbf{p}$ equation, given by [41]

$$\left\{ \frac{p^2}{2m_0} + \frac{\hbar}{m_0} \mathbf{k} \cdot \mathbf{p} + U(\mathbf{r}) \right\} u_{n\mathbf{k}}(\mathbf{r}) = \left[E_n(\mathbf{k}) - \frac{\hbar^2 k^2}{2m_0} \right] u_{n\mathbf{k}}(\mathbf{r}), \quad (1.3)$$

where \mathbf{p} is the momentum operator and n labels the energy band. The function $u_{n\mathbf{k}}(\mathbf{r})$ has the same periodicity as the crystal, i.e., $u_{n\mathbf{k}}(\mathbf{r}) = u_{n\mathbf{k}}(\mathbf{r} + \mathbf{R})$. Equation (1.2) and the periodicity of $u_{n\mathbf{k}}(\mathbf{r})$ constitute the Bloch theorem which indicates that electronic states in periodic crystals form a continuum of free-electron like states, whose wave functions are weighted by the Bloch functions. The considerations above assume perfect single crystals of infinite size, but for the most part the resulting material parameters can be used to model finite layers forming heterostructures.

Typically the bandstructure of crystalline materials is made of energy bands of allowed states and energy gaps which contain no electronic states. In intrinsic semiconductors under thermodynamic equilibrium, the Fermi level E_F is located roughly in the middle of the bandgap, depending on the densities of states of the bands. At zero temperature ($T = 0$) all the states in the energy bands below the Fermi level (in particular the valence band) are filled with electrons, whereas no electrons are occupying the states in the bands above the Fermi level (in particular the conduction band). At $T > 0$, part of electrons in the valence band are thermally excited to the conduction band, resulting in both valence and conduction bands being partly filled. Since only partly filled bands can conduct electrical current, conduction and valence bands together are responsible for current transport in semiconductors. When the system is not in thermodynamic equilibrium due to e.g. optical or electrical excitation, the conduction and valence bands generally remain in local equilibrium only internally described by their separate quasi-Fermi levels E_{Fn} and E_{Fp} , respectively.

The bandstructure calculated using Eq. (1.1) assumes a perfect crystal. The results remain almost unchanged if a small part of the atoms are replaced with impurity atoms introducing additional weakly bound electronic states in the band gap close to the band edges. These dopant atoms are divided to donors and acceptors. If the impurity state is located close to the conduction band and is occupied by an electron at $T = 0$, it acts as a donor state, and if it is located close to the valence band and is empty at $T = 0$, it acts as an acceptor state. At $T > 0$, part of the electrons of the donors are excited to the conduction band, and part of the valence band electrons are captured by the empty acceptor states. Therefore donor doping increases the electron density, resulting in n-type material, and acceptor doping decreases the electron density in the valence band, resulting in

p-type material. In GaN, Si is typically used as a donor and Mg is used as an acceptor.

Calculating the crystal bandstructure generally involves solving the dispersion relation, i.e., E as a function of \mathbf{k} , and the Bloch functions for the allowed bands. Calculation of the whole bandstructure is burdensome. However, in typical operation conditions of an LED, carrier dynamics takes place very close (only a few tens of meV) to the band edges. Therefore for optoelectronic applications it is often sufficient to know the dispersion relation only close to the band extrema, which in the case of GaN is at the Γ point for both conduction and valence bands. The bandstructure close to the band edges can be described in lowest order using the parabolic band approximation, where the dispersion relation is modeled by a parabola characterized by the effective mass m^* defined as (see, e.g., Ref. [40])

$$m_{ij}^* = \left(\frac{1}{\hbar^2} \frac{\partial^2 E}{\partial k_i \partial k_j} \right)^{-1}, \quad (1.4)$$

where i, j denote perpendicular coordinates. By using the effective mass, the electronic states can be approximated by free-electron states where the electron mass m_0 is replaced by m^* . The effective mass is negative for electron states close to the valence band edge, and there it is convenient to study the presence and movement of empty states instead. These empty states in the valence band are commonly referred to as holes in the semiconductor literature. They can be considered as fermion quasiparticles that have a positive effective mass and positive charge. Effective masses can be obtained using experimental data or by solving Eq. (1.1) close to the Γ point, e.g., using the $\mathbf{k} \cdot \mathbf{p}$ method.

Calculation of the full bandstructure, on the other hand, requires numerical methods. A full bandstructure of GaN single crystal is presented, e.g., in Ref. [42], calculated using empirical pseudopotentials fitted to experimental data. The bandstructure calculated in Ref. [42] is shown in Fig. 1.3, illustrating also the bandgap with no states between the highest valence band states at 0 eV and the lowest conduction band states at approx. 3.4 eV. The dispersion relations close to the edges of the conduction and valence bands have roughly parabolic forms, as assumed in the parabolic band approximation. Details of the conduction band of GaN have also recently been studied experimentally by measuring energy spectra of photoemitted electrons [43].

In situations where modeling of high-energy carriers is required, one

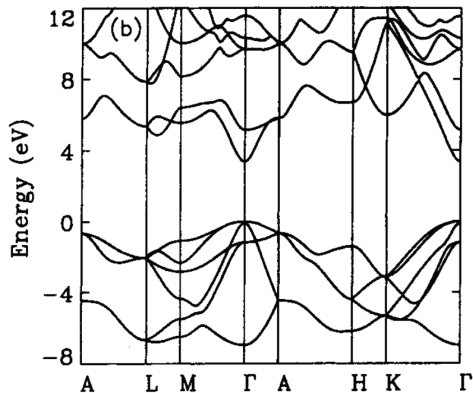


Figure 1.3. Bandstructure of wurtzite GaN as a function of k following the symmetry points inside the Brillouin zone, calculated using empirical pseudopotentials fitted to experimental data. States with $E < 0$ represent the valence band, the region $E \in (0, \sim 3.4)$ represents the bandgap, and states with $E > \sim 3.4$ represent the conduction band. Reprinted from Ref. [42] with publisher's permission.

needs to resort to full bandstructure or approximate it by fitting curves to the most important local energy extrema (also referred to as valleys) of the bands. One possible parametrization is presented in Ref. [44], where the five most important conduction band valleys are described using a nonparabolic model where the dispersion relation close to the valley extremum is given by

$$E(1 + \alpha E + \beta E^2) = \hbar^2 k^2 / 2m^*, \quad (1.5)$$

where the energy E and wavenumber k are measured from the center of the valley, α and β are nonparabolicity constants, \hbar is the reduced Planck's constant, and m^* is the effective mass. Note that the dispersion relation is given for a scalar k value measured from the center of the valley, since the model assumes a spherical bandstructure for III-N alloys. The parabolic approximation corresponding to $\alpha, \beta = 0$ is the most frequently used approximation in optoelectronics due to its accuracy close to the band edges and its simplicity.

1.4 State-of-the-art III-N LEDs

Regardless of the detailed layer structure, present-day state-of-the-art III-N LEDs are made of three functional layers: a homogeneous donor-doped (or n-type) region, a homogeneous acceptor-doped (or p-type) region, and an active region composed of quantum wells with a smaller bandgap than

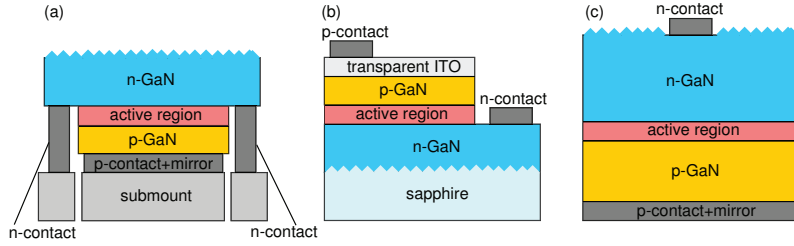


Figure 1.4. Layer structure of (a) the thin film flip-chip (TFFC) LED, (b) LED grown on patterned sapphire substrate (PSS LED), and (c) LED grown on bulk GaN substrate (bulk GaN LED). In (a) and (c), light is extracted through the roughened n-GaN surface whereas in (b), transparent Indium Tin Oxide (ITO) is used to improve light extraction from the p-GaN surface. The TFFC LED is also grown on sapphire, but the sapphire is removed by liftoff. Extraction efficiencies of the order of 80 % have been estimated for all the LED designs shown here [9].

the surrounding region. Applying a bias voltage over the LED causes electrons and holes to flow to the quantum wells where light is generated through radiative recombination. In blue LEDs the quantum wells are composed of $\text{In}_x\text{Ga}_{1-x}\text{N}$, where the molar fraction x is around 15 %. To enable white light, the LED chips are coated with phosphors that convert part of the blue light to longer wavelengths [45].

Figure 1.4 shows three slightly different high-efficiency LED structures: (a) a thin film flip-chip (TFFC) LED where the sapphire substrate has been removed, (b) an LED grown on patterned sapphire substrate (PSS LED), and (c) an LED grown on bulk GaN substrate (bulk GaN LED) [9]. All the structures contain the n-type GaN layer, the active region consisting of InGaN QWs, the p-type GaN layer, metal contacts, and possibly additional mirrors and transparent layers to improve light extraction. Typically an electron-blocking layer (EBL) consisting of AlGaIn is also placed between the active region and p-type GaN to decrease electron leakage. TFFC and PSS LEDs are conventional LED structures that have been commercially available for several years, whereas LEDs grown on bulk GaN form an emerging technology.

The conventional TFFC and PSS LED structures are grown on sapphire substrates using MOVPE. The resulting topmost layer will be p-type GaN, whereas n-type GaN will be located beneath other layers. This ordering of the growth is chosen, e.g., to facilitate current spreading and electrical contacting of p-type GaN which has a lower conductivity than n-GaN, and to improve the radiative efficiency by introducing the Mg dopant atoms only after growing the active region. To enable depositing contacts also on n-GaN, usually dry etching such as inductively coupled plasma (ICP)

is used to reveal the n-type layers.

The only major difference between the TFFC and PSS LED structures is that in TFFC, light is extracted from the n-GaN surface whereas in PSS, light is extracted through a transparent conducting layer, commonly Indium Tin Oxide (ITO), on top of p-GaN or through sapphire. Sapphire substrate is removed from the TFFC LED after the fabrication by laser liftoff, and the surface of n-GaN is roughened to improve light extraction [46]. The PSS LED, on the other hand, is grown on patterned sapphire structure to reduce the number of guided modes, and light extraction from the p-GaN surface is enabled by using a transparent conducting layer [47].

In contrast to the TFFC and PSS LEDs, the bulk GaN LED shown in Fig. 1.4(c) is grown by MOVPE directly on an n-type GaN substrate. LEDs grown on bulk GaN substrates have roughly similar current transport and light extraction properties as those grown on sapphire, but in addition they enable smaller dislocation density and growth on nonpolar or semipolar orientations, which are expected to enable a higher efficiency, reduced droop, and efficient green and even yellow LEDs [48–51]. Bulk GaN LEDs are emerging rapidly due to advances in the fabrication of GaN substrates, and some of the commercial high-efficiency LEDs are already grown directly on GaN [11].

LED technologies shown in Fig. 1.4 differ from each other mainly through their light extraction properties, fabrication techniques, and some material parameters. The current transport in all of them, however, is organized roughly similarly using the typical 1-dimensional current injection scheme, where electrons and holes are injected to the active region from different sides. Therefore their operation can often be well approximated using the same 1-dimensional device models, where only the extraction efficiencies and material parameters may be different. In Publications II, I, IV, and V, mainly the operation of the TFFC LED is modeled, but many of the conclusions can be generalized even for emerging LED technologies grown on bulk GaN. On the other hand, in Publications VI, VII, VIII, and IX, and partly also in Publications II and I, unconventional device concepts are proposed where either the current transport is truly 2-dimensional or the most essential layers for current transport consist of continuously graded materials.

2. Modeling of III-Nitride optoelectronic devices

The objective of this thesis is to develop and employ semiempirical models that are directly applicable in device-level simulations. Parameters for these models are determined either experimentally or by combining experimental data and information from computational models. To give the reader a general overview of the underlying physical concepts and related material parameters, this Section reviews the background of the semiempirical models using lowest-order semiclassical treatment. However, because the actual material parameters used in the simulations are based on experiments, also higher order effects are implicitly accounted for. The experimental determination of model parameters is made separately for materials of which the LED is made. Therefore the parameters are independent on the LED design except for the choice of materials.

This Section is organized as follows. Subsection 2.1 reviews the semiclassical model of carrier transport, Subsection 2.2 discusses the theory of carrier scattering, and Subsection 2.3 summarizes the key figures of merit of optoelectronic devices and modeling of the efficiency droop of III-N LEDs.

2.1 Semiclassical carrier transport

This Subsection reviews the semiclassical model of carrier transport used extensively in the majority of the Publications of this thesis. Modeling of semiclassical carrier transport is based on Boltzmann's transport equation described in Subsection 2.1.1. Drift-diffusion model and the Monte Carlo model, discussed in Subsections 2.1.2-2.1.4, are two extensively used techniques to simplify and solve the semiclassical carrier transport in semiconductor structures. Both of them make use of experimentally verified material parameters.

2.1.1 Boltzmann transport equation

In the semiclassical approximation, carrier transport is governed by the Boltzmann transport equation (BTE) given by (see, e.g., Ref. [52])

$$\frac{\partial f}{\partial t} + \mathbf{v} \cdot \nabla_r f + \frac{-e\mathcal{E}}{\hbar} \cdot \nabla_k f = \left(\frac{\partial f}{\partial t} \right)_{scatt}, \quad (2.1)$$

where $f(\mathbf{k}, \mathbf{r}, t)$ is the carrier distribution function to be solved, \mathbf{v} is the velocity, ∇_r is the nabla operator with respect to position, e is the elementary charge, \mathcal{E} is the electric field, \hbar is reduced Planck's constant, ∇_k is the nabla operator with respect to \mathbf{k} , and $\left(\frac{\partial f}{\partial t} \right)_{scatt}$ is the rate of change of the distribution function due to all the scattering mechanisms that are present in the material [52].

BTE is a semiclassical equation where carriers are considered distinguishable particles that obey the classical equation of motion between scattering events. Quantum effects are included through the dispersion relation of carriers and scattering processes described by $\left(\frac{\partial f}{\partial t} \right)_{scatt}$ that transfer carriers between different states. Note, however, that the interband and intraband scattering processes included in $\left(\frac{\partial f}{\partial t} \right)_{scatt}$ are also responsible for, e.g., photon emission and heat generation and are therefore of great importance for device modeling. They will be described in Subsection 2.2. Note that in Eq. (2.1) it is further assumed that no classical magnetic field is present in the material.

2.1.2 Drift-diffusion model

Drift-diffusion model is the most widely used approximate solution method for the BTE, and it can be used to solve the quasi-equilibrium distributions of conduction band electrons and valence band holes. The main approximation of the drift-diffusion model is that electrons and holes follow Boltzmann statistics, resulting from infinitely fast relaxation within the bands. Therefore it is based on quasi-equilibrium conditions and essentially consists of the current continuity equation and the drift-diffusion equation, both of which can be derived from the BTE. Detailed derivations are presented in Ref. [52], and here we summarize the main assumptions and resulting equations.

The current continuity equation follows from the BTE by integrating Eq. (2.1) over \mathbf{k} and using vector calculus and vector identities to rearrange the integrals. Using $v = \hbar^{-1}dE/dk$ and assuming $\mathbf{J} = -e\bar{v}n$, where \bar{v} is the average velocity, the resulting current continuity equation is given by

(see details in Ref. [52])

$$\nabla \cdot \mathbf{J}_n - e \frac{\partial n}{\partial t} = eR. \quad (2.2)$$

In particular, here all the interband scattering processes are accounted for using a net recombination rate density R . For steady-state solutions, the carrier density does not vary with time and Eq. (2.2) is solved using $\partial n / \partial t = 0$.

The drift-diffusion equation, on the other hand, can be obtained by multiplying the BTE of Eq. (2.1) with \mathbf{v} and integrating over \mathbf{k} . Calculating the integrals is relatively straightforward but requires many steps as detailed, e.g., in Ref. [52]. Assuming that the energy bands are parabolic, $E = \hbar^2 k^2 / (2m_c^*)$, and that carriers follow Boltzmann statistics, the resulting drift-diffusion equation is given by (see details in Ref. [52])

$$\mathbf{J}_n = -e\mu_n n \nabla \phi + eD_n \nabla n, \quad (2.3)$$

where ϕ is the electrostatic potential related to \mathcal{E} by $E = -\nabla \phi$, D_n is the diffusion constant, and the electron mobility is given by $\mu_n = q\tau_n / m_c^*$, τ_n being the average time between successive intraband scattering events. The equation can also be written using the quasi-Fermi level E_{Fn} as

$$\mathbf{J}_n = \mu_n n \nabla E_{Fn}. \quad (2.4)$$

To formulate the complete drift-diffusion model, Eq. (2.4) is substituted to Eq. (2.2), a similar equation is written for holes, and the equations are complemented with Poisson's equation to calculate the electrostatic force:

$$\begin{aligned} \nabla \cdot (-\varepsilon \nabla \phi + \mathbf{P}_{tot}) &= e(p - n + N_d - N_a) \\ \nabla \cdot \mathbf{J}_n &= \nabla \cdot (\mu_n n \nabla E_{Fn}) = eR \\ \nabla \cdot \mathbf{J}_p &= \nabla \cdot (\mu_p p \nabla E_{Fp}) = -eR, \end{aligned} \quad (2.5)$$

where ε is the permittivity, \mathbf{P}_{tot} includes the spontaneous and piezoelectric polarizations discussed in Subsection 1.3.2 and parametrized in Subsection 2.1.3, and N_d and N_a are the ionized donor and acceptor densities, respectively.

The assumptions of the drift-diffusion model imply that its validity is limited to situations where quantum transport and hot-carrier effects are not important. Furthermore, as the drift-diffusion model assumes perfect thermalization of carriers, it typically cannot be used to calculate detailed energy or velocity distributions of carriers, especially close to abrupt het-

erjunctions. Nevertheless, the drift-diffusion model has been found to reproduce experimental device-level characteristics of III-N LEDs to a good accuracy [13, 53, 54].

The largest error in the drift-diffusion model comes from the material parameters, which are based on semiempirical and experimental values. However, accurate values for spontaneous and piezoelectric polarization, band offset ratios, and recombination coefficients cannot be directly measured and are still under debate. The feasibility of using drift-diffusion model specifically in III-N LEDs is discussed in more detail in Ref. [54], where Bulashevich *et al.* show that the drift-diffusion model can generally be used to reproduce device-level measurement results such as current-voltage curves at intermediate and moderately high currents. At very low current densities the current is dominated by tunneling through defects in the MQW region. Publications IV and V also provide information regarding the applicability of the drift-diffusion model at intermediate and high current densities by comparing results from the drift-diffusion model and Monte Carlo simulations of the BTE.

2.1.3 Drift-diffusion model parameters

To give a concise but complete summary of the drift-diffusion model, this Subsection lists the quantities and parameters required for solving the model. In the drift-diffusion model, the distribution of electrons follows the Fermi-Dirac distribution, given by

$$f(E, E_{Fn}) = \frac{1}{\exp\left(\frac{E-E_{Fn}}{k_B T}\right) + 1}, \quad (2.6)$$

where E_{Fn} is the quasi-Fermi level (chemical potential) of the conduction band, k_B is Boltzmann's constant, and T is the temperature. Knowing the Fermi-Dirac distribution and E_{Fn} , the density of electrons in the conduction band is given by

$$n = \int_{E_c}^{\infty} f(E, E_{Fn}) g_c(E) dE, \quad (2.7)$$

where the 3-dimensional density of states for the conduction band resulting from the parabolic band approximation is given by

$$g_c(E) = \frac{1}{2\pi^2} \left(\frac{2m_c^*}{\hbar^2}\right)^{3/2} \sqrt{E - E_c}. \quad (2.8)$$

Equation (2.7) can be integrated numerically or by using properties of Fermi integrals and their tabulated values. By using the Fermi integral

of the order 1/2, given by

$$\mathcal{F}_{1/2}(\eta) = \frac{1}{\Gamma(3/2)} \int_0^\infty \frac{x^{1/2}}{1 + \exp(x - \eta)} dx, \quad (2.9)$$

where Γ is the Gamma function satisfying $\Gamma(3/2) = \sqrt{\pi}/2$, Eq. (2.7) can be rewritten as

$$n = N_c \mathcal{F}_{1/2} \left(\frac{E_{Fn} - E_c}{k_B T} \right). \quad (2.10)$$

Here N_c is a constant known as the effective density of states, given by

$$N_c = 2 \left(\frac{m_c^* k_B T}{2\pi \hbar^2} \right)^{3/2}. \quad (2.11)$$

In the case where the quasi-Fermi level is inside the bandgap separated from the band edge by more than $\sim k_B T$, the distribution function in the band is very close to a Boltzmann distribution. In that case, $\mathcal{F}_{1/2}$ is very accurately approximated by

$$\mathcal{F}_{1/2} = \exp \left(\frac{E_F - E_c}{k_B T} \right). \quad (2.12)$$

Holes are empty states in the conduction band, and therefore the hole density follows the distribution $1 - f(E, E_{Fp})$ or, equivalently,

$$p = N_v \mathcal{F}_{1/2} \left(\frac{E_v - E_{Fp}}{k_B T} \right), \quad (2.13)$$

where N_v is given by Eq. (2.11), using the effective hole mass for the valence band.

Spontaneous and piezoelectric polarization, represented in Poisson's equation (2.5) by \mathbf{P}_{tot} , are calculated in Refs. [55–57] for binary and ternary III-N alloys using density functional theory. Theoretical values for the spontaneous polarization for AlGa_xIn_{1-x}N alloys along the [0001] direction are given by

$$\begin{aligned} P_{sp}^{Al_xGa_{1-x}N} &= -0.090x - 0.034(1-x) - 0.019x(1-x) \\ P_{sp}^{In_xGa_{1-x}N} &= -0.042x - 0.034(1-x) + 0.038x(1-x), \end{aligned} \quad (2.14)$$

where $x \in [0, 1]$ is the molar fraction and P is in units of C/m². Furthermore, the piezoelectric polarization of a ternary III-N alloy along the [0001] direction can be calculated as a linear interpolation between the values for binary alloys, given by

$$\begin{aligned}
P_{pz}^{AlN} &= -1.808\chi + 5.624\chi^2 \text{ for } \chi < 0 \\
P_{pz}^{AlN} &= -1.808\chi - 7.888\chi^2 \text{ for } \chi \geq 0 \\
P_{pz}^{GaN} &= -0.918\chi + 9.541\chi^2 \\
P_{pz}^{InN} &= -1.373\chi + 7.559\chi^2,
\end{aligned} \tag{2.15}$$

where χ is the strain calculated in the [0001] plane [57]. The total internal polarization to be used in device calculations is defined here as $\mathbf{P}_{tot} = \mathbf{P}_{sp} + \mathbf{P}_{pz}$.

Values of the polarization have a significant effect on device simulations, since they strongly affect the bandedges and electric fields in III-N heterostructures. Publication II uses the values given by Eqs. (2.14)-(2.15) for calculation of polarization, whereas other Publications use values scaled by 0.5 due to experimental evidence suggesting smaller polarization values than those given in Eqs. (2.14)-(2.15) [58, 59]. Also other recently published computational studies of III-N devices have used scaled values for polarization [60, 61]. However, updated first principles calculations of the spontaneous and piezoelectric polarizations based on calculated first- and second-order piezoelectric coefficients have been provided in Ref. [62] and successfully employed in recent III-N LED simulations [63] but not yet used in the Publications of this thesis.

2.1.4 Monte Carlo model

To describe systems where the energy bands are not in internal equilibrium, the BTE of Eq. (2.1) must be solved directly. The general form of the BTE with many different scattering processes does not typically allow for analytical solutions. Moreover, due to many different scattering processes included in the right-hand side of Eq. (2.1), direct solution of the distribution function from the BTE is very complicated. An accurate numerical solution to the BTE for a semiconductor device can typically be obtained by simulation of a large number of carriers, subjected to the semiconductor bandstructure, electrostatic forces, and scattering probabilities calculated from quantum mechanics. As the effect of the collision term on the right-hand side of Eq. (2.1) can be modeled with independent probabilities for different scattering processes, methods using random numbers have proven most effective to generate numerical estimates for the full carrier distribution function.

The Monte Carlo (MC) method, described in detail e.g. in Refs. [64–66], is the most widely used method. Monte Carlo method has become very

popular, because it is relatively straightforward to implement and provides results that are easy to interpret physically. The MC method implements the physics included in the BTE by following the trajectories of a large number of carriers using their classical equation of motion and by employing random numbers to generate scattering events. Presenting the full mathematical basis and details of implementation of the Monte Carlo method is out of the scope of this thesis due to the large number of separately treated scattering processes. These can, however, be found in Refs. [64–66] that give a complete and comprehensible treatment. Nevertheless, the basic constituents of a Monte Carlo simulation are summarized in the following paragraphs, and calculation of the scattering rates is illustrated in Subsection 2.2.4.

In the MC method, free flights of each carrier between scattering events are simulated by numerically solving the classical equation of motion for the crystal momentum $\hbar\mathbf{k}$, given by

$$\hbar \frac{d\mathbf{k}}{dt} = -e\mathcal{E}. \quad (2.16)$$

Parallel to the equation of motion, also Poisson’s equation is solved periodically to update the \mathcal{E} field. Equation (2.16) and the associated initial values of positions and momenta of the carriers determine their paths between scattering events. The time and nature of the stochastic scattering event taking place at the end of each free flight are described by the Monte Carlo approach. The free-flight time, the scattering process, and the new value of \mathbf{k} are generated using random numbers as described below. The use of random numbers ensures that the scattering rates of carriers between different Bloch states follow from their physics-based rates, which are calculated for all the relevant interactions between carriers and the rest of the system, as explained in Section 2.2. The scattering rates of individual scattering processes are typically calibrated with experimental data.

Free-flight times depend on the scattering rates to be discussed in Subsection 2.2. However, generally the total scattering rate $W_{tot}(\mathbf{k})$, calculated by summing over all the separate scattering processes, depends on \mathbf{k} , and therefore generating free flights is complicated. By introducing a concept of self-scattering, describing a virtual non-scattering event, free-flight times can be generated from the homogeneous Poisson distribution. Using a constant scattering rate W_{max} that satisfies $W_{tot}(\mathbf{k}) < W_{max}$ at each \mathbf{k} , the scattering probability is constant and the free-flight time dis-

tribution depends exponentially on t , so that free-flight times t_{ff} can be generated by using random numbers $r_{ff} \in [0, 1]$ as

$$t_{ff} = \frac{1}{W_{max}} \ln(r_{ff}). \quad (2.17)$$

After each free flight, another random number $r_s \in [0, 1]$ is generated, multiplied with W_{max} , and used to choose a scattering process based on the separate scattering rates calculated for an electron with the wavevector \mathbf{k} . More specifically, the factor $W_{max}r_s$ is used to select a scattering process from the scattering ladder, which is constructed from the cumulative scattering rates as explained, e.g., in Ref. [66]. In particular, the rate of self-scattering is given by

$$W_{ss}(\mathbf{k}) = W_{max} - W_{tot}(\mathbf{k}). \quad (2.18)$$

In the case of self-scattering ($W_{max}r_s > W_{tot}$), the state of the electron remains unchanged and its free flight is continued according to Eq. (2.16). If a real scattering process is selected ($W_{max}r_s < W_{tot}$), the energy and \mathbf{k} vector of the electron are changed according to the selection rules, which depend on the scattering process and energy and momentum exchange between the electron and the rest of the system. After the scattering process, another free flight is generated with the new \mathbf{k} value as the initial state.

Monte Carlo method can be used to simulate the motion of carriers that on average satisfy the BTE and follow the distribution function $f(\mathbf{k}, \mathbf{r}, t)$. The accuracy of the resulting distribution function is only limited by the accuracy of the material parameters used in the BTE and the amount of simulation data. Typically the Monte Carlo method is used to obtain steady-state average solutions $f_{ave}(\mathbf{k}, \mathbf{r})$ at a given bias voltage. The simulation is started from selected initial conditions, e.g., values from a drift-diffusion simulation, and run until the electrostatic potentials and electron densities have reached steady state. After that, the simulation is continued to collect statistics for $f_{ave}(\mathbf{k}, \mathbf{r})$ by calculating the time averages of carrier densities, carrier energy distributions, and other relevant parameters.

2.2 Carrier scattering

Carrier scattering strongly affects the transport of electrons and holes in electronic devices. Interband scattering transfers electrons between conduction and valence band states and results in, e.g., emission of light, absorption of light, and generation of high-energy electrons through Auger processes. Intraband scattering, on the other hand, transfers electrons (holes) between conduction (valence) band states, reducing their mobility and driving the system towards equilibrium. Basic theory of interband and intraband scattering is discussed here briefly to justify the semiempirical scattering models used to simulate carrier transport in this work. Radiative interband scattering, or radiative recombination, is the basis for the operation of LEDs, and its most important physical constituents will be described using a semiclassical approach. Nonradiative interband processes can be treated using similar techniques but the calculations are usually more complex even in the lowest-order approximation. For them we only show the typical semiempirical parametrizations. Intraband scattering, on the other hand, is usually nonradiative and will be described by summarizing the most important points.

The device simulations performed in this thesis apply semiempirical models for scattering, and the model parameters are determined either experimentally or by combining experimental data and information from computational models. The simplified derivations of this Subsection are only meant to provide an overview of the most important physical processes behind scattering, and they are not used to calculate scattering parameters. For this purpose it is sufficient to consider the lowest-order treatment. In the lowest-order treatment, the rates of the different scattering processes can be derived from time-dependent perturbation theory resulting in Fermi's golden rule, which gives the scattering rate as [67]

$$W = \frac{2\pi}{\hbar} |\langle f | H' | i \rangle|^2 \delta(\Delta E), \quad (2.19)$$

where i and f denote the initial and final unperturbed states of the system, H' is the perturbing Hamiltonian that causes the transition, and the Kronecker delta ensures energy conservation.

2.2.1 Radiative interband scattering

Radiative interband scattering constitutes of processes where electrons and holes interact with photons. Accounting for all the details of light-

matter interaction requires sophisticated many-body methods such as semiconductor Bloch equations (SBE) and semiconductor luminescence equations (SLE) [68–70]. However, in this thesis all the device simulations make use of well-known and well-established semiempirical models for calculating the emission rate from electron and hole densities (see, e.g., Ref. [17]). Parameters for these semiempirical models are taken from experiments, and thereby the models include implicitly also the contributions from excitonic effects.

To illustrate the basic physics behind the semiempirical models and to give the reader a general idea of the basic light-matter interaction processes in semiconductor structures, below we summarize the processes using the lowest-order semiclassical approximation. In the semiclassical approximation, light is treated as a classical electromagnetic field that modifies the full Hamiltonian in Eq. (1.1) to $H = 1/(2m_0)(\mathbf{p} - e\mathbf{A})^2 + V(\mathbf{r})$, where \mathbf{A} is the vector potential. When the terms including \mathbf{A} are considered as a perturbation and \mathbf{A} is assumed to have the plane wave form, $H'(\mathbf{r}, t)$ is given by [41]

$$H'(\mathbf{r}, t) = \mathcal{H}'(\mathbf{r}) \exp(-i\omega t) + h.c., \quad (2.20)$$

where $h.c.$ denotes the Hermitian conjugate and

$$\mathcal{H}'(\mathbf{r}) = -\frac{eA_0 \exp(i\mathbf{k}_p \cdot \mathbf{r})}{2m_0} \hat{\mathbf{a}} \cdot \mathbf{p}, \quad (2.21)$$

where A_0 is the amplitude of the vector potential at a given photon energy $\hbar\omega$, \mathbf{k}_p is the photon wavevector, $\hat{\mathbf{a}}$ is the unit polarization vector of the light, and \mathbf{p} is the momentum operator of the electron. The term including A^2 has been neglected in Eqs. (2.20)-(2.21), since it is much smaller than the other terms for optical field densities relevant for LED devices [41].

Absorption

Using the Fermi's golden rule, the absorption rate for light with photon energy $\hbar\omega$ by an electron in the initial valence band Bloch state v is given by

$$W_{abs} = \frac{2\pi}{\hbar} |\langle c | \mathcal{H}' | v \rangle|^2 \delta(E^c - E^v - \hbar\omega), \quad (2.22)$$

where c is the final conduction band Bloch state, \mathcal{H}' is given by Eq. (2.21), $\hbar\omega$ is the energy of the photon, and E^c and E^v are the energies of the conduction and valence band states, respectively. Typically the optical

wavelengths are also long enough to allow using the dipole approximation where $\exp(i\mathbf{k}_p \cdot \mathbf{r}) \approx 1$, and the matrix element of Eq. (2.22) can be written as

$$|\mathcal{H}'_{cv}|^2 = |\langle c|\mathcal{H}'|v\rangle|^2 = \frac{e^2 A_0^2}{4m_0^2} |\hat{\mathbf{a}} \cdot \langle c|\mathbf{p}|v\rangle|^2 \approx \frac{e^2 A_0^2}{4m_0^2} |\hat{\mathbf{a}} \cdot \mathbf{p}_{cv}|^2 \delta(\mathbf{k}_c, \mathbf{k}_v), \quad (2.23)$$

where \mathbf{p}_{cv} depends only on the periodic parts of the Bloch functions for the conduction and valence band as

$$\mathbf{p}_{cv} = \langle u_{c\mathbf{k}}(\mathbf{r})|\mathbf{p}|u_{v\mathbf{k}}(\mathbf{r})\rangle, \quad (2.24)$$

integrated over the unit cell. Only the electronic states are included in the \mathbf{k} conservation, with the usual approximation $\mathbf{k}_c, \mathbf{k}_v \gg \mathbf{k}_p$.

Equation (2.22) accounts for absorption by a single pair of conduction and valence band states, assuming that the initial state is occupied and the final state is vacant. The probabilities that states v and c are occupied are given by values of the distribution function $f(E^v)$ and $f(E^c)$. Note that in the Monte Carlo simulations, the distribution functions are not necessarily Fermi functions but represent the more general case where electron and hole distributions can be out of quasi-equilibrium. All the possible \mathbf{k}_v and \mathbf{k}_c values contribute to the absorption, and therefore the total absorption rate per unit volume is given by

$$R_{abs} = \frac{2}{V} \sum_{\mathbf{k}_c, \mathbf{k}_v} \frac{2\pi}{\hbar} |\mathcal{H}'_{cv}|^2 \delta(E^c - E^v - \hbar\omega) (1 - f(E^c)) f(E^v), \quad (2.25)$$

where summation is performed over values for $\mathbf{k}_c = \mathbf{k}_v$ that provide the energy difference $\hbar\omega$, and spin degeneracy is included. Note that both distribution functions in Eq. (2.25) are written for electrons. Assuming parabolic bands and replacing the sum over \mathbf{k} with the three-dimensional joint density of states of the conduction and valence bands, the absorption rate per unit volume can be expressed as

$$R_{abs} = \frac{\pi}{\hbar} \frac{e^2 A_0^2}{2m_0^2} |\hat{\mathbf{a}} \cdot \mathbf{p}_{cv}|^2 g_r (\hbar\omega - E_g) (1 - f(E^c)) f(E^v), \quad (2.26)$$

where g_r is the joint density of states between the conduction and valence band, given by

$$g_r(\hbar\omega - E_g) = \frac{1}{2\pi^2} \left(\frac{2m_r^*}{\hbar^2} \right)^{3/2} (\hbar\omega - E_g)^{1/2}, \quad (2.27)$$

m_r^* being the reduced effective mass, given by

$$\frac{1}{m_r^*} = \frac{1}{m_e^*} + \frac{1}{m_h^*}. \quad (2.28)$$

The vector potential A_0 in Eq. (2.26) is related to the spectral intensity $\mathcal{P}(\hbar\omega)$ through the Poynting theorem as $\mathcal{P}(\hbar\omega) = n_r c \varepsilon_0 \omega^2 A_0^2 / 2$. On the other hand, writing $\mathcal{P}(\hbar\omega)$ using the photon density of states $N(\hbar\omega) = n_r^3 (\hbar\omega)^2 / (\pi^2 \hbar^3 c^3)$ and the photon number n_{ph} (following Bose-Einstein distribution for thermal radiation) and equating with Poynting's theorem, A_0 is given by

$$A_0 = \sqrt{\frac{2\hbar^2}{n_r^2 \varepsilon_0 \hbar \omega} n_{ph} N(\hbar\omega)} \quad (2.29)$$

This results in the absorption rate expressed as a function of the photon number per unit volume and energy interval,

$$R_{abs} = \frac{\hbar \pi e^2}{m_0^2 n_r^2 \varepsilon_0} \frac{1}{\hbar \omega} |\hat{\mathbf{a}} \cdot \mathbf{p}_{cv}|^2 g_r(\hbar\omega - E_g) (1 - f(E^c)) f(E^v) n_{ph} N(\hbar\omega). \quad (2.30)$$

The total absorption rate per unit volume is obtained by integrating the spectral R_{abs} over $\hbar\omega$.

We can also use the rate of Eq. (2.26) to define the absorption coefficient α_P as

$$\alpha_P = -\frac{1}{\mathcal{P}} \frac{d\mathcal{P}}{dx}. \quad (2.31)$$

Performing the differentiation and reorganizing, Eq. (2.31) results in

$$\mathcal{P}(x) = \exp(-\alpha_P x) \mathcal{P}(0), \quad (2.32)$$

which is the Beer-Lambert law for a homogeneous medium. The spectral intensity is related to R_{abs} as $d\mathcal{P}/dx = (d\mathcal{P}/dt)(1/c) = -R_{abs} \hbar\omega$. Substituting this to Eq. (2.31), the total absorption coefficient for photon energy $\hbar\omega$ describing only the contribution of absorption processes (emission processes will be considered separately in the following paragraphs) is given by

$$\alpha_P(\hbar\omega) = \frac{\hbar \pi e^2}{n_r c \varepsilon_0 m_0^2} \frac{1}{\hbar \omega} |\hat{\mathbf{a}} \cdot \mathbf{p}_{cv}|^2 g_r(\hbar\omega - E_g) (1 - f(E^c)) f(E^v). \quad (2.33)$$

Emission

The emission of light can take place through stimulated emission, which forms the basis of laser operation, or spontaneous emission, which is the

most important process for LEDs. Stimulated emission is the inverse process of absorption, and therefore the total rate of stimulated emission per unit volume and energy interval can be written by replacing $(1 - f(E^c))f(E^v)$ in Eq. (2.30) with $f(E^c)(1 - f(E^v))$, resulting in

$$R_{st} = \frac{\hbar\pi e^2}{m_0^2 n_r^2 \varepsilon_0} \frac{1}{\hbar\omega} |\hat{a} \cdot \mathbf{p}_{cv}|^2 g_r (\hbar\omega - E_g) f(E^c) (1 - f(E^v)) n_{ph} N(\hbar\omega) \quad (2.34)$$

The net rate of stimulated emission is obtained as $R_{st} - R_{abs}$. Therefore the net gain of the semiconductor is given by

$$g(\hbar\omega) = \frac{\hbar\pi e^2}{n_r c \varepsilon_0 m_0^2} \frac{1}{\hbar\omega} |\hat{a} \cdot \mathbf{p}_{cv}|^2 g_r (\hbar\omega - E_g) (f(E^c) - f(E^v)). \quad (2.35)$$

The net gain becomes positive at population inversion, where $f(E^c) - f(E^v)$, and in this case the optical field grows as given by Eq. (2.32), with $-\alpha_P$ replaced by g .

Spontaneous emission rate can be derived from quantum theory of light or by using detailed balance considerations and Einstein's coefficients. Absorption and the stimulated and spontaneous emission rates, written using Einstein's B_{vc} (absorption), B_{cv} (stimulated emission), and A_{cv} (spontaneous emission) coefficients, are given by

$$R_{abs} = B_{vc} n_{ph} f(E^v) (1 - f(E^c)), \quad (2.36)$$

$$R_{st} = B_{cv} n_{ph} f(E^c) (1 - f(E^v)), \quad (2.37)$$

and

$$R_{sp} = A_{cv} f(E^c) (1 - f(E^v)). \quad (2.38)$$

In thermal equilibrium, there is only one Fermi level and the detailed balance condition requires emission and absorption to be equal, giving

$$R_{abs} = R_{st} + R_{sp}. \quad (2.39)$$

Writing this with Eqs. (2.36)-(2.38) and rearranging the equation, it can be shown that it holds only if

$$A_{cv} = B_{vc} = B_{cv}. \quad (2.40)$$

Therefore also the rates R_{st} and R_{sp} satisfy

$$\frac{R_{st}}{R_{sp}} = n_{ph}, \quad (2.41)$$

and the rate of spontaneous emission per unit volume and energy interval is given by

$$R_{sp} = \frac{\hbar\pi e^2}{m_0^2 n_r^2 \varepsilon_0} \frac{1}{\hbar\omega} |\hat{\mathbf{a}} \cdot \mathbf{p}_{cv}|^2 g_r(\hbar\omega - E_g) f(E^c) (1 - f(E^v)) N(\hbar\omega). \quad (2.42)$$

The total emission rate per unit volume is again obtained by integrating over $\hbar\omega$.

It can be shown (e.g. Refs. [71, 72]) that when electrons and holes follow Boltzmann statistics, the spontaneous emission rate is proportional to the product of n and p . Most parametrized device models therefore calculate the radiative recombination of LEDs using a net recombination rate density given by

$$R_{rad} = B(np - n_i^2), \quad (2.43)$$

where B is the net radiative recombination coefficient and n_i is the intrinsic carrier concentration of the material. This model will be used also in most of the calculations presented in this work. Publication IX uses a modified version of this model, where the B coefficient is scaled by the overlap factor of the confined QW states to account for the quantum-confined Stark effect (QCSE), as explained in Subsection 2.2.3. Numerical value of B depends on the details of the bandstructure as well as the QCSE and optical environment, but typically the values reported for In-GaN QWs are of the order of $10^{-17} \text{ m}^3/\text{s}$ [73–75].

Experimental reports suggest that Eq. (2.43) agrees well with experimental data at carrier densities relevant for typical LED operating conditions, but the value of the B coefficient starts to decrease at strongly degenerate conditions, i.e., at very high carrier concentrations [17]. Also theoretical reports based on the semiconductor luminescence equations suggest that the model of Eq. (2.43) does not hold at carrier densities required for laser operation mainly due to phase-space filling, i.e., the decreasing availability of initial and final states to provide the transition [76, 77]. In addition to the phase-space filling, the effect of Coulomb interaction can be significant at strongly degenerate conditions and decrease the validity of Eq. (2.43). Effect of Coulomb interaction on the spontaneous emission spectra and lifetimes in III-N QWs has been calculated based on semiconductor luminescence equations in Ref. [78], where Chow *et al.* reported that Coulombic effects contribute to the details of the emission spectrum.

2.2.2 Nonradiative recombination

In addition to interband radiative recombination described in the previous subsections, the most important interband recombination processes in LEDs are Shockley-Read-Hall (SRH) recombination, which takes place through localized trap states in the bandgap, and Auger recombination, which excites a third carrier to a high-energy state. Typically the energy released in these processes ends up heating the device. Impact ionization is the inverse process of Auger recombination and an important generation process in power devices, but not usually significant in optoelectronic applications. This Subsection summarizes the semiempirical models for these nonradiative recombination processes.

SRH recombination involves the relaxation of an electron from conduction to valence band through isolated energy states within the bandgap created, e.g., by impurities and other lattice imperfections. SRH recombination processes were studied by Shockley, Read, and Hall in Refs. [79,80], where they showed that for nondegenerate semiconductors, it can be calculated as

$$R_{srh} = \frac{np - n_i^2}{\tau_p(n + n_1) + \tau_n(p + p_1)}, \quad (2.44)$$

where τ_n and τ_p are SRH lifetimes, and n_1 and p_1 are the electron and hole densities in the case where the Fermi level coincides with the energy level of the trap state responsible for SRH recombination. The lifetimes depend on the material quality, and for typical GaN-based materials they are of the order of 10^{-7} s [81].

Auger recombination processes involve three carriers or three carriers and a phonon, and the energy released in the recombination of an electron-hole pair excites a third carrier to a high-energy state. The rates for direct and phonon-assisted Auger recombination in the bulk and QWs can be estimated to first order by using Auger coefficients C_n and C_p for electrons and holes [82]. The Auger recombination rate density is then parametrized as

$$R_{aug} = (C_n n + C_p p) (np - n_i^2). \quad (2.45)$$

Numerical values for the C_n and C_p coefficients are calculated from first principles e.g. in Refs. [22,83], where direct, phonon-assisted, and alloy scattering assisted Auger processes have been considered. Auger coefficients have also been measured for quasi-bulk InGaN layers using a pho-

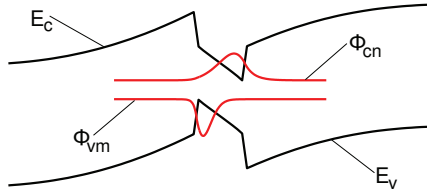


Figure 2.1. Conduction and valence band edges and the ground state ($m, n = 1$) envelope wave functions in a QW and the surrounding bulk material. Due to the nonzero electric field in the QW caused by spontaneous and piezoelectric polarization, the peaks of the wave functions occur at different positions.

toluminescence technique [84] and for lasers where InGaN QWs provide the gain, using large signal modulation measurements [73]. These methods suggest values of C_n and C_p in the range of 10^{-43} to 10^{-42} m⁶/s.

2.2.3 Interband transitions in QWs

Envelope wave functions in QWs

The interband recombination rates in the previous subsection were considered only for transitions between bulk Bloch functions. In a QW, electrons and holes are confined in the direction perpendicular to the QW plane and interband transitions occur mainly between these confined states. Figure 2.1 shows a typical band diagram of an InGaN QW surrounded by GaN. When the crystal potential is already accounted for by the free-electron approximation and the effective mass, Schrödinger's equation in the z direction for free-electron states in the conduction band is given by [41]

$$\left[-\frac{\hbar^2}{2m_c^*} \frac{d^2}{dz^2} + U_{ext}(z) \right] \phi_{cn}(z) = E_n \phi_{cn}(z), \quad (2.46)$$

where U_{ext} is the conduction band edge as a function of z , $\phi_{cn}(z)$ is the envelope wave function of the n th QW state (also called subband), and E_n is the corresponding eigenenergy. In the bulk case, $U_{ext} = 0$, E_n is not quantized and $\phi_{cn}(z)$ are plane waves.

The envelope wave function modulates the wave functions in the Bloch's theorem, so that the general solution to Schrödinger's equation corresponding to the n th QW subband can be written as

$$\psi_{cn}(\mathbf{r}) = u_{c\mathbf{k}}(\mathbf{r}) \frac{\exp(i\mathbf{k}_t \cdot \mathbf{r})}{\sqrt{A_{qw}}} \phi_{cn}(z), \quad (2.47)$$

where A_{qw} is the cross-section area of the QW and k_t is the component of

the wavevector parallel to the QW interface. The dispersion relation of each conduction subband is given by

$$E = E_n + \frac{\hbar^2 k_t^2}{2m_c^*}. \quad (2.48)$$

Similar expressions are obtained for the valence band wave functions ψ_{vm} , envelopes ϕ_{vm} , and eigenenergies. In quantum wires and quantum dots, the states are confined in two or three perpendicular directions, but this is not relevant for the structures considered in this work. In the more general case, a sum of the single band envelopes (2.47) is taken to include typically two conduction bands (spin degeneracy) and six valence bands (magnetic subbands). These states are then mixed by diagonalizing the total electronic Hamiltonian.

Modifications to interband transition rates

With the general solutions to Schrödinger's equation in the QWs given by Eq. (2.47) for the conduction band and a similar equation for the valence band, the matrix element of Eq. (2.23) is modified to

$$H'_{cv} = -\frac{eA_0}{2m_0} \hat{a} \cdot \langle c|\mathbf{p}|v\rangle \approx -\frac{eA_0}{2m_0} \hat{a} \cdot \mathbf{p}_{cv} \delta(\mathbf{k}_{tc}, \mathbf{k}_{tv}) I_{cv}, \quad (2.49)$$

where \mathbf{k}_{tc} and \mathbf{k}_{tv} are the wave vector components of the conduction and valence bands parallel to the QW interface, and I_{cv} is the overlap integral between the envelope wave functions, given by

$$I_{cv} = \langle \phi_{cn} | \phi_{vm} \rangle = \int_{-\infty}^{\infty} \phi_{cn}^*(z) \phi_{vm}(z) dz. \quad (2.50)$$

The net radiative recombination coefficient B is proportional to the square of the momentum matrix element and therefore the modified coefficient B of a quantum well is related to the bulk material coefficient B_0 as

$$B = |I_{cv}|^2 B_0. \quad (2.51)$$

In symmetric wells with zero electric field, $I_{cv} \approx 1$ and B is very close to B_0 . In InGaN QWs surrounded by GaN, the quantum-confined Stark effect is large, reducing B with respect to B_0 and making it dependent on the operating point.

Despite the more complex dependencies of SRH and Auger recombination on the states involved, arguments in Ref. [24] suggest that the A and C coefficients follow a similar dependence in QWs, i.e.,

$$A = |I_{cv}|^2 A_0 \quad (2.52)$$

and

$$C = |I_{cv}|^2 C_0, \quad (2.53)$$

where A_0 and C_0 are the SRH and Auger coefficients for bulk material, respectively.

The reasoning behind Eqs. (2.52) and (2.53) presented in Ref. [24] is summarized as follows. The rate of SRH recombination is proportional to $|\langle \psi_{cn} | \psi_{trap} \rangle \langle \psi_{trap} | \psi_{vm} \rangle|^2$, where ψ_{trap} is the wave function of the trap state caused by a defect. The wave function of the trap state extends spatially only to a few bond lengths from the defect center, causing the recombination rate of a specific trap to be proportional to the squared electron-hole wave function overlap calculated at the defect position. If the defects are assumed to be spread randomly throughout the QW, the total SRH recombination rate of the QW can be calculated by multiplying the bulk SRH coefficient with the squared envelope wave function overlap as in Eq. (2.52). This is further supported by experimental evidence that the A coefficient in InGaN QWs has a monotonic dependence on the overlap factor [85].

The matrix element for Auger recombination in the QWs, on the other hand, contains the overlap of the envelope functions of the four states taking part in the Auger process. The overlap factor of the envelope functions of these states can be reduced to I_{cv} , since (1) the wave function of the Auger-excited state is not confined in the QW and therefore its envelope function is a plane wave, and (2) the initial envelope wave function of the excited carrier overlaps completely with the envelope wave function of the recombining carrier. As the Auger recombination rate is proportional to the square of the matrix element, with these arguments the Auger coefficient in a QW reduces to that given by Eq. (2.53).

2.2.4 Intraband scattering

While the previous subsections discussed interband scattering where electrons transfer between conduction and valence band states, this Subsection summarizes the main aspects of intraband scattering. In an intraband scattering processes, the electronic state of a carrier changes through interactions with phonons, photons, or other lattice imperfec-

tions, but the final electronic state is still within the same band as the initial state. Intraband scattering processes are further divided into intravalley and intervalley processes, where the initial and final states are within the same valley and different valleys, respectively.

Intraband scattering is predominantly caused by interaction with phonons, other carriers, impurities, and other distortions in the periodic lattice. As for interband scattering, intraband scattering probability per unit time for a carrier in a given state characterized by its energy, wavevector, and band can be calculated from Fermi's golden rule, given by

$$W(\mathbf{k}, \mathbf{k}') = \frac{2\pi}{\hbar} |\langle \mathbf{k}', l' | H' | \mathbf{k}, l \rangle|^2 \times \delta[E(\mathbf{k}', l') - E(\mathbf{k}, l)] \quad (2.54)$$

where \mathbf{k} and \mathbf{k}' are initial and final \mathbf{k} vectors of the carrier and l and l' are the initial and final states of the rest of the system. Integrating over \mathbf{k}' (and l, l') provides scattering rates $W(E[\mathbf{k}])$ for each process as a function of the electron's initial energy, and the state after the scattering is chosen based on the details of $W(\mathbf{k}, \mathbf{k}')$.

Detailed forms of $W(\mathbf{k}, \mathbf{k}')$ for the large number of different intraband scattering processes are well known and provided, e.g., in Refs. [64–67] and references therein. Presenting the full mathematical basis and details of intraband scattering in semiconductor device simulation is out of the scope of this thesis, but e.g. Refs. [65, 67] give a detailed treatment of intraband scattering. Below we only illustrate how the scattering probabilities and rates used within Monte Carlo are calculated from the probabilities, using as an example the acoustic and optical phonon scattering caused by deformation potentials. For intraband scattering processes other than those caused by phonons through deformation potential interaction, we only summarize the main points and refer the reader to Refs. [64–67].

Deformation potential phonon scattering is caused by deformations in the lattice and the resulting changes in the energy bands. For deformation potential scattering, the perturbing Hamiltonian is given by $H' = \sum_{ij} E_{ij} 1/2(\partial y_i / \partial r_j + \partial y_j / \partial r_i)$, where E_{ij} is the deformation potential tensor, $\partial y_i / \partial r_j$ is the deformation of the crystal, and i and j are coordinate indices. The general form for deformation potential scattering probability due to phonons with angular frequency ω_q and polarization ξ is given by [65]

$$W(\mathbf{k}, \mathbf{k}') = \frac{\pi}{\rho V \omega_q} \binom{N_q}{N_q + 1} \mathcal{G}(\mathbf{k}, \mathbf{k}') \left| \sum_{ij} E_{ij} q_j \xi_i \right|^2 \delta[E(\mathbf{k}') - E(\mathbf{k}) \mp \hbar \omega_q], \quad (2.55)$$

where ρ is the density of the material, V is the volume, N_q is the phonon occupation number (upper symbol for absorption, lower for emission), \mathcal{G} is the squared overlap integral of $u_{n\mathbf{k}}$ and $u_{n\mathbf{k}'}$, and q is the phonon wavenumber.

For intravalley scattering by acoustic phonons, the deformation potential is diagonal and the factor $|\sum_{ij} E_{ij} q_j \xi_i|^2$ in Eq. (2.55) reduces to $E_{11}^2 q^2$, where E_{11} is the diagonal element of the deformation potential. Furthermore, the overlap factor \mathcal{G} is approximately one due to small differences between the initial and final \mathbf{k} values. The resulting scattering probability is given by [65]

$$W(\mathbf{k}, \mathbf{k}') = \frac{\pi q E_{11}^2}{V \rho u_l} \binom{N_q}{N_q + 1} \delta[E(\mathbf{k}') - E(\mathbf{k}) \mp \hbar q u_l], \quad (2.56)$$

where u_l is the velocity of longitudinal acoustic phonons. After integrating over \mathbf{k}' and accounting for acoustic phonon dispersion and density of states, the scattering rate for emission and absorption is given by [65]

$$W(E[\mathbf{k}]) = \frac{(m^*)^{1/2} (k_B T)^3 E_{11}^2}{2^{5/2} \pi \hbar^4 u_l^4 \rho} E^{-1/2} \left\{ \begin{array}{l} F_1(E(\mathbf{k})) - F_1(E(\mathbf{k})) \\ G_1(E(\mathbf{k})) - G_1(E(\mathbf{k})) \end{array} \right\}, \quad (2.57)$$

where the functions F_1 and G_1 account for the phonon distribution, as specified in Ref. [65].

For intravalley scattering by optical phonons, the term $|E_{ij} q_j \xi_i|^2$ is replaced by an optical coupling constant $(D_t K)^2$. Due to the dispersion relation of optical phonons, the phonon energy $\hbar \omega_{op}$ and the phonon number N_q are approximately constant. As a result, the scattering probability is given by [65]

$$W(\mathbf{k}, \mathbf{k}') = \frac{\pi (D_t K)^2}{\rho V \omega_{op}} \binom{N_{op}}{N_{op} + 1} \delta[E(\mathbf{k}') - E(\mathbf{k}) \mp \hbar \omega_{op}]. \quad (2.58)$$

For spherical parabolic bands the integration over \mathbf{k}' and the phonon states yields [65]

$$W(E[\mathbf{k}]) = \frac{(D_t K)^2 (m^*)^{3/2}}{2^{1/2} \pi \hbar^3 \rho \omega_{op}} \binom{N_{op}}{N_{op} + 1} (E \pm \hbar \omega_{op})^{1/2}. \quad (2.59)$$

Equations (2.57) and (2.59) are directly proportional to the probability of intervalley scattering events caused by acoustic and optical phonons,

respectively, and used with corresponding equations for other scattering processes to determine which scattering event takes place in the Monte Carlo simulation after the free flight, as described in Subsection 2.1.4. After choosing the scattering mechanism, the final state is then generated so that the distribution of k' corresponds to Eqs. (2.56) and (2.58) or the corresponding equations for other scattering mechanisms.

In addition to deformation potential, polar, and piezoelectric phonon scattering, the most important intraband scattering processes are ionized impurity, carrier-carrier, alloy disorder, and surface roughness scattering [64–67]. Ionized impurity scattering, caused by Coulombic interaction, is usually considered elastic and is most important in doped materials. In bipolar devices, carrier-carrier scattering includes electron-electron, electron-hole, and hole-hole collisions, and the rates are calculated from Coulombic interaction using the carrier distribution functions. Alloy disorder scattering accounts for modifications in the band structures of ternary or quaternary alloys due to inhomogeneity in the material. Finally, surface roughness scattering accounts for distortions to transport at material interfaces due to either specular or diffusive reflection mechanisms.

Since the publications use Monte Carlo methods only for studying electron transport, we discussed the intraband scattering rates only for electrons. The formulas were also shown only for spherical parabolic bands for simplicity. For ellipsoidal and/or nonparabolic bands used in Publications IV and V the main points are similar but the resulting equations are more complex [65].

2.3 Efficiency of III-N LEDs

Several complex effects contribute to the LED efficiency, such as charge transport, recombination, optical losses, and light extraction. As a result, understanding the contributions and interplay of different processes in the efficiency of LEDs is very challenging, as exemplified by the prolonged discussion of the origin of the efficiency droop. To separate between different effects, many definitions for the figures of merit to describe aspects of the efficiency have been suggested. The remainder of this Section is devoted to discussing these effects, related definitions, and models for the efficiency droop.

2.3.1 Efficiency definitions

The key figure of merit of a light emitter is the wall-plug efficiency describing the overall efficiency of the LED and defined as the ratio of the optical output power P_{out} and the electrical input power, given by

$$\eta_{WPE} = \frac{P_{out}}{IV_a}, \quad (2.60)$$

where I is the injection current and V_a is the applied bias voltage. However, the wall-plug efficiency is affected by numerous electrical and optical phenomena as well as the material quality of the active region, and therefore it is useful to divide it into specific efficiency figures, each including only a few important factors. We factor η_{WPE} in a similar way as in Ref. [86], resulting in

$$\eta_{WPE} = \eta_{VTG} \times \eta_{EQE} = \eta_{VTG} \times \eta_{IQE} \times \eta_{EXE}, \quad (2.61)$$

where the voltage efficiency, defined as $\eta_{VTG} = \hbar\omega/(eV_a)$, describes the ratio of the average photon energy and the average electrical energy needed to compensate the energy loss of an electron, passing through the device. Moreover, η_{EQE} is the external quantum efficiency describing the efficiency to convert electron-hole pairs to extracted photons and defined as the number of extracted photons divided by the number of electrons injected to the device, and η_{IQE} is the internal quantum efficiency describing the efficiency of converting electron-hole pairs to photons within the semiconductor and defined as the net number of emitted photons divided by the number of injected electrons. Finally, η_{EXE} is the light extraction efficiency describing the efficiency of extracting the generated photons out from the LED and defined as the number of photons extracted from the device divided by the net number of emitted photons under steady-state conditions. Therefore η_{EXE} accounts for optical losses outside the active region of the LED. When characterizing the efficiency of white-light emitters, the spectral output power is further weighted by the human eye sensitivity function to calculate the luminous efficiency, which gives the luminous flux divided by the electrical input power and has the unit of lumens per watt.

In the definition of Eq. (2.61), the external quantum efficiency η_{EQE} is further broken down to the product of the extraction efficiency η_{EXE} and the internal quantum efficiency η_{IQE} , given by

$$\eta_{EXE} = \frac{P_{out}/\hbar\omega}{\mathcal{R}_{rad}} \quad (2.62)$$

and

$$\eta_{IQE} = \eta_{INJ} \times \eta_{RAD} = \frac{\mathcal{R}_{rec}}{I/q} \times \frac{\mathcal{R}_{rad}}{\mathcal{R}_{rec}}, \quad (2.63)$$

where η_{INJ} is the injection efficiency describing the ability of the active region to capture electron-hole pairs for recombination and defined as the net recombination rate \mathcal{R}_{rec} divided by the total carrier injection rate I/e , I being the total injection current. The radiative efficiency of the device, η_{RAD} , is defined as the net radiative recombination rate \mathcal{R}_{rad} divided by the net recombination rate. The term net recombination here implies that terms \mathcal{R}_{rad} and \mathcal{R}_{rec} also account for photon recycling, i.e., the generation of electron-hole pairs due to reabsorption of the emitted photons.

When qV_a is smaller than the bandgap energy of the AR, η_{VTG} is larger than one and enables electroluminescent cooling if η_{EQE} is high enough. Theoretical studies of LEDs with efficiencies exceeding unity have been reported by Heikkilä *et al.* in Refs. [71, 87], and the first experimental demonstration of electroluminescent cooling was reported by Santhanam *et al.* in Ref. [88], where the voltages were of the order of 70 μV and the photon energies were roughly 0.5 eV, corresponding to η_{VTG} of the order of several thousands.

2.3.2 Models for efficiency droop

By the efficiency droop we understand the decrease of the LED efficiency from its peak value as the input current is increased. The efficiency droop is a critical problem, as it limits the output power of the LED. The most frequently suggested causes to the efficiency droop include nonradiative recombination, current leakage, and reduction of radiative recombination at high carrier densities.

It is instructive to write the external quantum efficiency as

$$\eta_{EQE} = \frac{\eta_{EXE} \times \mathcal{R}_{rad}}{I/e} = \frac{\eta_{EXE} \times \mathcal{R}_{rad}}{\mathcal{R}_{rad} + \mathcal{R}_{nr} + I_{leak}/e}, \quad (2.64)$$

where I_{leak} is the part of the current that does not result in recombination and \mathcal{R}_{nr} is the total rate of nonradiative recombination. The extraction efficiency η_{EXE} is typically assumed to be constant and therefore does not contribute to droop.

The ABC model, applied e.g. in Refs. [13,17,19,22,27], is the most widely used model for the efficiency droop. In addition to its physical origin, it can be thought of as the total current density J expanded as a power series of the excess carrier density n in the active region. Considering only the three lowest terms, the current density is given by $J = ed(An + Bn^2 + Cn^3)$, where d is the effective thickness of the active region and A , B , and C are constants. Further assuming that the radiative recombination is fully represented by the n^2 term, the external quantum efficiency in the simple ABC model is given by

$$\eta_{EQE} = \eta_{EXE} \frac{Bn^2}{An + Bn^2 + Cn^3}. \quad (2.65)$$

Assuming charge neutrality and $n \gg (n_i, n_1, p_1)$ (see Subsections 2.2.1-2.2.2), the A , B , and C coefficients of the ABC model directly represent the SRH, radiative, and Auger recombination coefficients. Therefore the ABC model phenomenologically describes the radiative and nonradiative recombination processes, where Bn^2 describes radiative recombination and the An and Cn^3 terms correspond to nonradiative SRH and Auger recombination, respectively. The simple ABC model qualitatively reproduces the droop and the dependence of the efficiency on the carrier density close to the peak efficiency. The most important assumptions of the ABC model represented by Eq. (2.65) are that (i) the total LED current can be represented by the three lowest powers of the excess carrier density of the active region, and (ii) the n^2 -dependent term includes only radiative recombination. The model usually fails at very high current densities where its most important underlying assumptions no longer hold.

Writing \mathcal{R}_{rad} and \mathcal{R}_{nr} of Eq. (2.64) with help of the ABC model, Eq. (2.64) can be expressed as

$$\eta_{EQE} = \frac{\eta_{EXE} \times Bn^2}{An + Bn^2 + Cn^3 + J_{leak}/(ed)}, \quad (2.66)$$

where J_{leak} is the leakage current density. Compared to the simple ABC model of Eq. (2.65), in Eq. (2.66) the ABC model is complemented with an additional factor for the carrier leakage losses.

Despite being possibly the simplest available model, Eq. (2.66) already gives an idea of the complexity of the droop phenomenon. Even at simplest, the efficiency is affected by a large number of intertwined factors ranging from material quality (mainly the A coefficient) to the geometry (mainly the B coefficient, extraction efficiency, and leakage) and optical properties. Furthermore, each of the loss factors in Eq. (2.66) is

extremely difficult to measure individually, partly explaining why theories for the droop remain controversial. Recent compelling experimental results highlighting the role of Auger recombination [26, 27] may soon clarify the problem, although accepting Auger recombination as the main cause would still require resolving the contradicting results for the C coefficient and the theoretical works suggesting that Auger recombination might not be the only possible explanation for the measurements [89, 90]. In addition to nonradiative recombination, reduction of the radiative B coefficient due to phase-space filling effects has also been suggested to significantly contribute to droop [17].

Leakage current represented by J_{leak} in Eq. (2.66) is also considered as a possible contributor for the droop [28]. It has typically been suggested to result from thermionic emission of electrons from the QWs or from overflow of electrons, where part of electrons flowing to the QWs flow directly to the p-GaN without relaxing to the confined states of the QW. Schubert *et al.* suggest that the leakage current would have third- and fourth-order dependences on the carrier density [91]. On the other hand, drift-diffusion simulations that distinguish between the bound and continuum carrier populations of the QWs suggest that Auger recombination together with the Auger-generated leakage current could provide a sufficient explanation for the droop even with the smaller Auger coefficients reported in the literature [23].

In addition to Auger recombination and different forms of leakage current, density-activated defect recombination (DADR) has been suggested to contribute to the efficiency droop. Hader *et al.* [20, 21] have proposed that the defect-related loss current density can be estimated from the carrier density as

$$J_{DADR} = \begin{cases} 0, & \text{for } n < n_0 \\ \frac{ed}{\tau_{DADR}} \frac{(n-n_0)^2}{2n_0}, & \text{for } n > n_0, \end{cases} \quad (2.67)$$

where d is the thickness of the active region, τ_{DADR} the density-activated defect recombination lifetime, and n_0 is the threshold carrier density. Both τ_{DADR} and n_0 must both be determined by fitting Eq. (2.67) to experimental data.

Generalizing Eq. (2.66) to account for all the additional losses listed above, the formula for η_{EQE} will include loss processes with 1-, 2-, 3-, and 4-order dependences of the carrier density. Some of these loss processes also overlap with each other as well as the n^2 -dependent radiative

recombination rate. Some of the models may also lose their validity at high input powers due to phase space filling [77]. These challenges call for further theoretical and experimental work using models which clearly distinguish between different possible causes for the efficiency droop, or reliably study the contribution of only selected effects. The challenge is to reliably determine the contributions of the dominant recombination and other loss mechanisms to enable more reliable tracking of the origin of the efficiency droop.

3. Results and discussion

The work and results leading to this thesis can be divided into two parts: (1) properties and challenges of present-day LEDs and (2) unconventional structures and their feasibility to be used in new device concepts. Results for the first part are presented in Subsection 3.1, while new devices are studied in Subsection 3.2.

3.1 Performance of typical III-N LEDs

This Subsection discusses the operation and efficiency of typical MQW LEDs to identify the key factors affecting the LED performance. Subsection 3.1.1 reviews Publications II and I, identifying and analyzing current transport losses preventing ideal carrier spreading in InGaN QWs. In the drift-diffusion simulations these losses are observed as quasi-Fermi losses, and the simulations predict a possible solution to reduce them by direct lateral current injection.

Subsection 3.1.2 is based on Publication III, and it introduces and demonstrates a technique to approximate the internal quantum efficiency and light extraction efficiency from an electroluminescence measurement as well as obtain order-of-magnitude estimates for the recombination coefficients of the ABC model.

Subsection 3.1.3 is based on Publications IV and V, describing a Monte Carlo–drift-diffusion simulation model used to study the physics of Auger recombination and hot electrons as well as their contribution to the efficiency droop of typical III-N LED structures.

3.1.1 Current transport in heterostructures

In III-N MQW structures, drift-diffusion equations predict significant voltage losses that are not purely resistive. These voltage losses are ob-

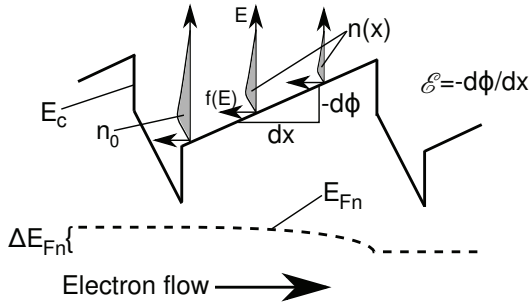


Figure 3.1. Schematic conduction band edge of two quantum wells and the barrier material between them. Electron flow is directed from left to right, and electric current flows in the opposite direction. The quasi-Fermi level changes in the barrier between the quantum wells due to the constant current flowing between them and the opposing electric field in the barrier material.

served as spatial changes in the quasi-Fermi levels, denoted as quasi-Fermi losses. Quasi-Fermi losses show up in practically all computational studies of electron and hole transport in MQW LEDs [13, 15, 53, 63, 92, 93] but they are usually not studied in detail. However, comparison to experiments shows that such effects are needed to explain why adding more quantum wells to a MQW LED increases the forward voltage as shown experimentally in Ref. [50] and why typically only one QW dominates the emission in a MQW stack [94]. This suggests that at least phenomenologically, the quasi-Fermi losses are a real physical effect, even though the basic drift-diffusion model probably does not include all the relevant physical effects to quantitatively model them. To decrease the quasi-Fermi losses, transverse-vertical junction (TVJ) LEDs are studied and compared to conventional structures using simulations in Publications II and I.

Figure 3.1 shows a schematic illustration of the conduction band edge and its quasi-Fermi level for two quantum wells and the barrier material between them. The quasi-Fermi loss between the two QWs is marked in the figure as ΔE_{Fn} . The figure also illustrates the electron density $n(x)$ and the approximately constant electric field \mathcal{E} in the barrier material. Numerical solutions of the drift-diffusion equations typically predict quasi-Fermi losses corresponding to the example in the figure, and more specifically, when electron current flows into a potential well, the quasi-Fermi level changes abruptly in the barrier material before the material interface. Similar effect is present for valence band holes flowing through the MQW region.

The quasi-Fermi loss ΔE_{Fn} between successive QWs can be solved analytically assuming negligible recombination and constant electric field

in the barrier layers between the QWs. We show the resulting equations here for conduction band electrons, but similar results follow trivially for valence band holes. Under normal operating conditions the polarization difference between GaN and InGaN together with the applied bias voltage creates an approximately constant electric field \mathcal{E} in the GaN barriers. Assuming a constant current density J in the barriers, the quasi-Fermi loss ΔE_{Fn} between different ends of the barrier can be derived as

$$\Delta E_{Fn} = -k_B T \ln \left\{ \frac{J}{\mu_n n_0 \mathcal{E} e} \left[\exp \left(\frac{e \mathcal{E} x}{k_B T} \right) - 1 \right] + 1 \right\}, \quad (3.1)$$

where k_B is Boltzmann's constant, T is temperature, μ_n is the electron mobility, n_0 is the electron density at the left end of the barrier, and x is the position. Equation (3.1) has a singular point x_s at

$$x_s = \frac{k_B T}{e \mathcal{E}} \ln \left(1 - \frac{e \mu_n n_0 \mathcal{E}}{J} \right). \quad (3.2)$$

The quasi-Fermi loss given by Eq. (3.1) is small for a barrier thickness much less than x_s , but it increases strongly for barrier thicknesses close to x_s . This indicates that if an electron current density J ($J < 0$) is to be carried over a potential barrier with an electric field \mathcal{E} , the barrier thickness should be significantly smaller than x_s . Essentially x_s represents the barrier thickness where the change in the quasi-Fermi level needed to pass a current J over the barrier approaches infinity. In MQW LEDs this phenomenon leads to very nonuniform light emission from different QWs as well as elevated input voltages for added QWs, both phenomena observed experimentally [50, 94]. Similar equations can also be derived for barriers with zero electric field (typical to nonpolar structures), but their quasi-Fermi loss is significantly smaller except for very large band discontinuities. More detailed derivations can be found in Publication I.

Results of Eq. (3.1) and numerical solutions of the drift-diffusion equations are compared with each other in Fig. 3.2, where (a) shows the simulated conduction band edge and quasi-Fermi level and (b) shows the the quasi-Fermi level calculated analytically from Eq. (3.1) with values for n_0 , electric field, and current density taken from the simulation data. Results given by the numerical and the analytical model are very close to each other, confirming the analytical expression for the quasi-Fermi losses.

Quasi-Fermi losses limit the current that can pass through the LED for a given voltage. Therefore the presence of quasi-Fermi losses increases the voltages required to reach the desired output power. Increasing the voltage required for a certain output power directly decreases the wall-

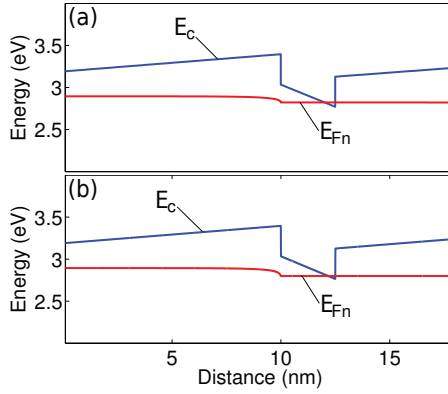


Figure 3.2. Conduction band edge and the conduction band quasi-Fermi level in a structure with one 2.5 nm thick QW sandwiched between 10 nm thick GaN barriers. (a) shows the simulated band diagram and (b) shows the simulated conduction band edge and the quasi-Fermi level calculated analytically from Eq. (3.1) with n_0 , E , and J taken from the simulation result. Reprinted from Publication I with publisher’s permission.

plug efficiency. While structure optimization has already led to some commercial samples with low turn-on voltages (indicating also small quasi-Fermi losses at small currents), better theoretical understanding of the phenomenon will enable more flexible engineering of heterostructure light emitters. In particular, this will enable MQW structures with an equal emission from all the QWs and a high wall-plug efficiency. Eventually this requires moving beyond the drift-diffusion model in the MQW and at material interfaces.

One possible solution to decrease quasi-Fermi losses studied in Publication I is to develop structures that use lateral current injection to the QWs from the side in addition to the typical perpendicular current through the MQW region. Lateral structures and a conventional reference structure are shown in Fig. 3.3. The thin-film flip-chip (TFFC) LED is a typical c-plane MQW LED introduced in Ref. [46], whereas the transverse-vertical junction (TVJ) LEDs are variations where a lateral current injection component to the quantum wells is added as in structures presented in Refs. [95, 96]. The lateral current injection present in the TVJ structures of Figs. 3.3(b) and 3.3(c) may significantly decrease the quasi-Fermi losses and improve the device operation. Note that the lateral width in the h-TVJ structure is 10 μm instead of 100 μm of the other two structures to compensate for the low mobility of holes, which limits their lateral spreading from the side to the MQW region. Detailed information about the structures and material parameters used in the calculations can be

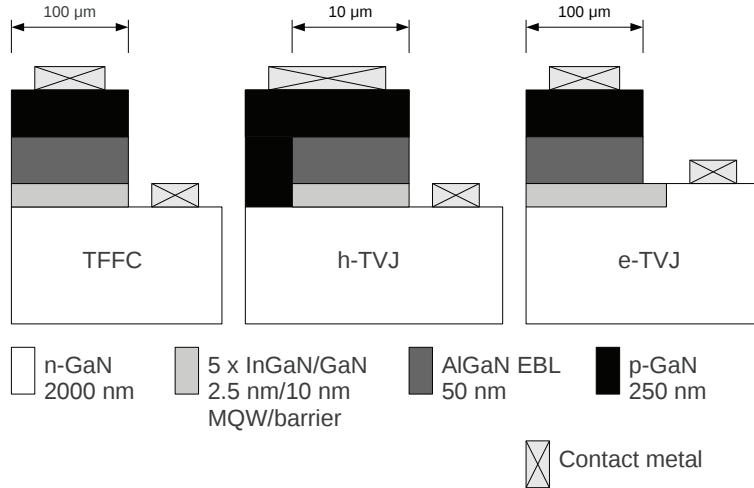


Figure 3.3. Thin-film flip-chip (TFFC) and transverse-vertical junction (TVJ) LED structures both for holes (h-TVJ) and electrons (e-TVJ). Quasi-equilibrium current transport is studied theoretically and numerically to demonstrate differences in current transport losses. Reprinted from Publication I with publisher's permission.

found in Publication I.

Figure 3.4 shows the band diagrams of the TFFC and TVJ LED structures at a current density that corresponds to the maximum efficiency of the h-TVJ structure. All the structures have five $\text{In}_{0.15}\text{Ga}_{0.85}\text{N}$ QWs with a bandgap ~ 2.7 eV and an $\text{Al}_{0.2}\text{Ga}_{0.8}\text{N}$ electron-blocking layer with a bandgap ~ 3.8 eV embedded in GaN with a bandgap ~ 3.4 eV. The figures also show the operating points. The quasi-Fermi losses are significantly smaller in both TVJ LEDs than in the TFFC LED, because the lateral current component facilitates the spreading of carriers in all the QWs. This is a fundamental difference between the TVJ and TFFC structures, but in experimental setups its magnitude may depend on the quality of the regrowth process needed to fabricate the more complex TVJ structures. Note that in Fig. 3.4(b) the valence band quasi-Fermi level is non-monotonous due to the lateral current injection to the QWs from the side.

Figure 3.5 shows the radiative recombination rate distribution of the LEDs using the same operating points as in Fig. 3.4. The smallest quasi-Fermi losses of the h-TVJ structure enabled by the direct hole injection lead to a significantly more uniform light output in all the five QWs than in the TFFC and e-TVJ structures. Further analysis of the results shows that the effective number of emitting QW in the h-TVJ structure is 3.8 at low current densities compared to 1.05 and 1.03 in TFFC and e-TVJ,

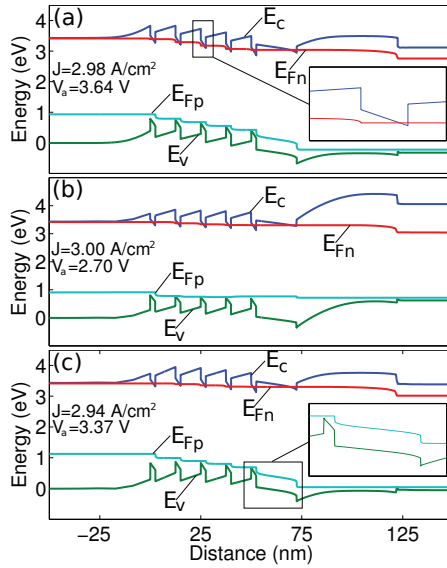


Figure 3.4. Band diagrams of the (a) TFFC structure, (b) h-TVJ structure, and (c) e-TVJ structure along a straight vertical line in Fig. 3.3 drawn in the middle of the structures, starting from n-GaN and ending in p-GaN. Band diagrams for the different structures have been plotted for similar current densities, and the operating points are marked in the figures. The inset in (a) shows a zoomed figure of the conduction band edge and quasi-Fermi level close to a QW, and the inset in (c) shows the valence band edge and quasi-Fermi level next to the EBL, both showing significant changes in the quasi-Fermi level. Reprinted from Publication I with publisher's permission.

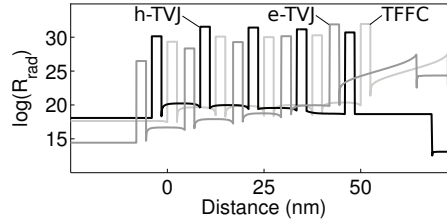


Figure 3.5. Radiative recombination rates as a function of position in the structures of Fig. 3.3 along a straight vertical line drawn in the middle of the structures, starting from n-GaN and ending in p-GaN. The operating points are the same as in Fig. 3.4. The curves have been shifted relative to each other to make the figures easier to read. Reprinted from Publication I with publisher's permission.

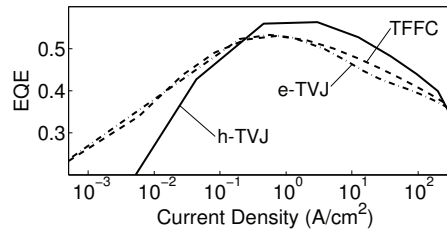


Figure 3.6. External quantum efficiency (EQE) of the TFFC, e-TVJ, and h-TVJ structure. Reprinted from Publication I with publisher's permission.

respectively. Even at large current densities, effectively 2.5 QWs emit light in the h-TVJ compared to 1.02 in both TFFC and e-TVJ structures.

Smaller quasi-Fermi losses in the h-TVJ structure lead to a more uniform emission from all the QWs than in the TFFC and e-TVJ structures. Most importantly this improves the predicted device efficiency. Figure 3.6 shows the external quantum efficiency (EQE) of the structures, taking into account nonradiative recombination, light extraction losses, and leakage current. Better carrier distribution between all the QWs in the h-TVJ structure results in a higher peak efficiency and higher corresponding current density than in the TFFC and e-TVJ. This difference between the structures is even larger in the wall-plug efficiency (not shown), because the smaller turn-on voltage of the h-TVJ structure also decreases the input power needed for a given current density.

Structures of Fig. 3.3 were also simulated in Publication I so that the bulk AlGaIn EBL was replaced by plain p-type GaN. Unexpectedly, the results show no leakage current despite the missing EBL. In structures that include the EBL, the large bias voltages needed to inject holes over the EBL increases the electron concentration in the p-type material at typical operating conditions and therefore enables a larger leakage. This indicates that using an unoptimized bulk AlGaIn EBL may even impair

the operation of the LED. III-N MQW LEDs without the AlGaIn EBL have also been reported experimentally to have a smaller efficiency droop as compared to samples with AlGaIn EBLs with different Al compositions [16].

The TVJ structure making use of lateral current injection is one possible way of decreasing the quasi-Fermi losses and significantly improving the device performance. Other carefully engineered 2- or 3-dimensional device architectures are expected to have a similar beneficial effect.

3.1.2 Measurement of internal efficiencies

Measuring the external quantum efficiency (η_{EQE}) of an LED is fairly straightforward, but many separate factors contribute to the η_{EQE} . Most importantly, the η_{EQE} is affected by the internal quantum efficiency η_{IQE} and the light extraction efficiency η_{EXE} . The internal quantum efficiency is mainly dependent on nonradiative recombination in the active region. The light extraction efficiency, on the other hand, depends on the probability by which the photons can escape from the LED. Direct measurement of η_{IQE} and η_{EXE} would be attractive, as it allows for comparing different active region designs, growth conditions, and surface finishings on the resulting device characteristics.

Typically the η_{IQE} and η_{EXE} are measured by comparing the photoluminescence (PL) or electroluminescence (EL) at low temperature and room temperature [97, 98]. However, this requires a low-temperature measurement setup and assumes unity η_{IQE} at low temperatures. Light extraction efficiency η_{EXE} can also be estimated by simulation and used to deduce η_{IQE} from the measured η_{EQE} [99, 100]. This method is limited to simple structures where η_{EXE} can be simulated reliably. Rate equation based models can also be fitted to PL measurements to estimate η_{IQE} , but this typically requires approximations such as ignoring Auger recombination [101].

Figs. 3.7(a) and (b) show the main quantities needed to break down the LED efficiency to its constituents: (1) the radiative recombination in free space R_0 (assuming ideal extraction and no photon reabsorption), (2) the net radiative recombination rate R taking into account photon reabsorption and the optical environment, (3) the generation rate G of new electron-hole pairs resulting from photon reabsorption, (4) the nonradiative recombination rate X , and (5) the photon output rate O .

Figure 3.7(c) shows two ways of defining η_{IQE} and η_{EXE} based on these

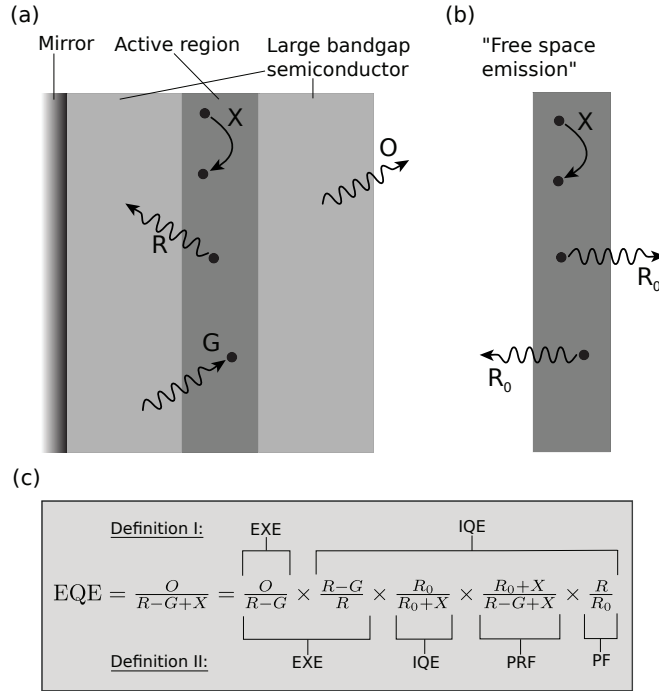


Figure 3.7. (a) An illustration of the most important factors contributing to the η_{EQE} in a general simplified LED cavity. R is the net radiative recombination rate, G is the generation rate, X is the nonradiative recombination rate, and O is the photon output rate. (b) shows the recombination rate R_0 of the active region material with ideal extraction and no photon reabsorption. (c) shows two alternative definitions for η_{EXE} and η_{IQE} found in the literature, if injection efficiency is not accounted for. Reprinted from Publication III with publisher's permission.

processes. In definition I, η_{IQE} is defined as the ratio of the net radiative recombination rate and net recombination rate, and η_{EXE} is defined as the photon output rate divided by the net recombination rate. In Definition II, η_{EXE} is defined using the total radiative recombination rate, and η_{IQE} is the total radiative recombination rate divided by the total recombination rate, therefore being purely a material property with no dependence on the LED structure itself. Photon recycling factor (PRF) and Purcell factor (PF) account for photon recycling and spontaneous emission enhancement or suppression. Usually definition I is preferred in experimental works due to its simplicity [97, 98, 101], whereas definitions more similar to definition II are used in theoretical works for better physical description [87, 99, 100].

Publication III investigates a direct measurement method for the η_{IQE} and η_{EXE} in the context of definition I. The method relies on measuring the optical output power vs. the injection current using a current source

and a calibrated photodetector or integrating sphere. The current density through the LED can then be expressed as a third order Taylor series as a function of the active region's excess electron density n as

$$J = ed (An + Bn^2 + Cn^3), \quad (3.3)$$

where e is the elementary charge, d is the thickness of the active region (AR), and A , B , and C are the Taylor coefficients. If the leakage current is small and if radiative recombination is proportional to n^2 , A , B , and C correspond to Shockley-Read-Hall (SRH), net radiative, and Auger recombination coefficients, respectively. The photocurrent density of the LED (current density responsible for emitting extracted photons) then depends on n as

$$P = \eta_{EXE} \times edBn^2, \quad (3.4)$$

where η_{EXE} is the extraction efficiency according to definition I. Solving for n , writing the η_{EQE} as $P/J(P)$ and differentiating twice with respect to P results in [18]

$$\eta_{EXE} = \eta_{EQE,m}^2 / (\eta_{EQE,m} + 4P_m^2 D_2), \quad (3.5)$$

where $\eta_{EQE,m}$ is the maximum η_{EQE} , P_m is the photocurrent density corresponding to $\eta_{EQE,m}$, and D_2 is the second derivative of η_{EQE} at P_m . After calculating η_{EXE} from Eq. (3.5), η_{IQE} can be obtained from the η_{EQE} as $\eta_{IQE} = \eta_{EQE}/\eta_{EXE}$. Furthermore, on a logarithmic scale the $\eta_{EQE}(P)$ forms a parabola centered at $\log_{10} P_m$.

Extracting the η_{IQE} and η_{EXE} using the method presented here does not require any external input parameters. However, one can also use Eqs. (3.3) to solve two of the Taylor coefficients as a function of the third one. If we choose to solve A and B as a function of C , we obtain

$$A = \left(\frac{(1 - \eta_{EQE,m}/\eta_{EXE})P_m}{ed \cdot \eta_{EQE,m}} \right)^{2/3} \sqrt[3]{\frac{C}{4}} \quad (3.6)$$

and

$$B = \left(\frac{2 \cdot \eta_{EQE,m} \cdot C}{1 - \eta_{EQE,m}/\eta_{EXE}} \right)^{2/3} \sqrt[3]{\frac{P_m}{ed}} \cdot \frac{1}{\eta_{EXE}}. \quad (3.7)$$

Eqs. (3.6) and (3.7) show that calculating the values of A and B from the measurements requires knowledge of the active region thickness and of the C coefficient, which can be assumed to be equal to the Auger recombination coefficient. The equations can also be written, e.g., for B and

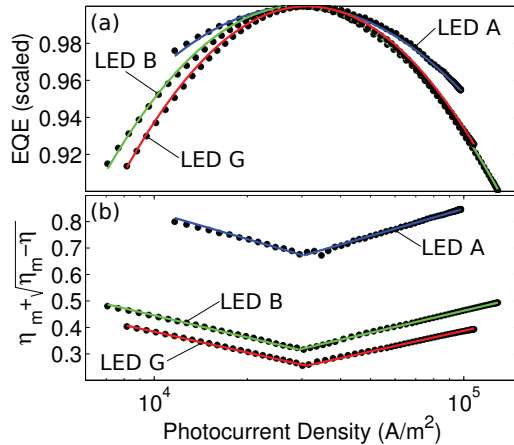


Figure 3.8. (a) Measured η_{EQE} (dots) and fitted second-order polynomials (lines) scaled with the maximum values vs. measured photocurrent density. (b) square-rooted transformed measured η_{EQE} (dots) and fitted linear curves. Both figures show LEDs A, B, and G, and their maxima are 0.67, 0.32, and 0.26, respectively. Reprinted from Publication III with publisher's permission.

C , if A is determined from small-signal measurement as in Ref. [17] and Publication X.

In Publication III we measured η_{EQE} for commercial LEDs and unpackaged samples grown at Aalto University. The measurements were performed using pulsed current to avoid LED heating, and the measurements were restricted to relatively low currents to avoid high injection level effects on the radiative recombination. Figure 3.8(a) shows the measured η_{EQE} and fitted parabolas for a commercial sample A and samples B and G grown for Publication III. The data and curves are scaled by dividing with the peak efficiencies to highlight their parabolic forms. The parabolas fit very well to the measured efficiencies, supporting the assumption of the n^2 dependency of radiative recombination leading to Eq. (3.4). Figure 3.8(b) shows the same data transformed as $\eta_{EQE,m} + \sqrt{\eta_{EQE,m} - \eta_{EQE}}$, which enables easier reading of the second derivative needed in Eq. (3.5).

Table 3.1 shows the η_{EXE} and maximum η_{IQE} calculated from the measurement of η_{EQE} for the commercial sample A and planar samples B-G grown by the authors of Publication III. Order-of-magnitude estimates for the A and B parameters are also listed, using $C = 1.5 \times 10^{-42} \text{ m}^6/\text{s}$ as input [73, 84]. The Table also shows information of depositing a SiN interlayer within the n-GaN layer, which has been reported to improve light extraction [102]. The 74 % maximum η_{IQE} and 91 % η_{EXE} of the commercial blue-emitting sample A are comparable with 63 % and 80 % reported for a near-UV sample using the low temperature PL method in

Table 3.1. Efficiencies obtained from the transformed data of Fig. 3.8(b) and fitted linear curves. Table shows the emission wavelength (λ), estimated extraction efficiency (η_{EXE}), measured maximum η_{EQE} ($\eta_{EQE,m}$), and estimated maximum η_{IQE} ($\eta_{IQE,m}$) for all the measured LEDs.

	λ (nm)	η_{EXE}	$\eta_{EQE,m}$	$\eta_{IQE,m}$	A (10^6 1/s)	B (10^{-17} m ³ /s)
Commercially packaged LED						
LED A	450	0.91	0.67	0.74	3.0	1.2
Planar LEDs with SiN interlayer						
LED B	417	0.50	0.32	0.64	5.6	1.0
LED C	417	0.54	0.34	0.63	5.7	0.98
LED D	417	0.55	0.31	0.56	7.2	0.87
Planar LEDs, no SiN interlayer						
LED E	405	0.38	0.23	0.61	6.5	0.97
LED F	405	0.36	0.22	0.61	6.5	1.0
LED G	405	0.43	0.26	0.60	6.9	0.95

Ref. [97]. The high extraction efficiency of sample A indicates very small optical losses in the packaged LED and efficient photon recycling.

The unpackaged samples B-G, on the other hand, have significantly smaller extraction efficiencies than the commercial sample A. Their η_{IQE} is also lower than in sample A most probably due to less optimized material quality or unoptimal location of the active region within the emitter cavity, thus leading to emission to nonextracting modes. The unpackaged samples with (samples B-D) and without (E-G) the SiN interlayer also show very little variation in the efficiencies between each other. However, samples B-D with the SiN interlayer have a significantly higher η_{EXE} than samples E-G without the SiN interlayer, which is in line with results of Ref. [102]. Thus, the method to measure η_{IQE} and η_{EXE} allows for very useful comparisons between samples fabricated with different growth recipes.

The order-of-magnitude estimates for A appear to have a weak reverse correlation to the estimates of $\eta_{IQE,m}$ as expected, but further measurements would be needed to confirm if the method reliably reproduces the A coefficient. The estimated values of B , on the other hand, are very similar between all the samples. Estimates for A and B can be compared, e.g., to empirical values presented in Refs. [73].

In measuring η_{EXE} and η_{IQE} with the method presented here, one has to assume that radiative recombination depends quadratically on the carrier density and that it is the dominant process with such a dependence

in the LED. This is typically considered a reasonable assumption at the relatively low carrier density regime, whereas e.g. Refs. [17, 77] demonstrate that this assumption breaks down at high currents. If the method is used to estimate SRH, radiative, and Auger recombination coefficients, one further assumes that they are equal to the Taylor coefficients of Eq. (3.3).

3.1.3 Auger recombination, hot electrons and droop

Auger recombination is frequently suggested to be the main reason behind the efficiency droop of LEDs. Recent studies have also highlighted a secondary effect of Auger recombination in addition to annihilating conduction band electrons in the QWs, namely the generation of hot carriers that can escape the QW. Hot electron emission through Auger recombination in the QWs was predicted theoretically by Deppner *et al.* in Ref. [23], and hot electrons have been measured by electron emission spectroscopy [26] and photoluminescence techniques [27].

Direct accurate measurements of hot electron generation inside LED devices are very hard to perform, and the measurements of Iveland *et al.* have started a dynamic debate of the origins of hot electrons in their measurements [89]. Further theoretical work is therefore needed to interpret measurements of Auger recombination and hot carriers. In Publications IV and V, transport of electrons is studied for the LED structure shown in Fig. 3.9 using Monte Carlo simulations to solve the BTE. In addition to showing the LED structure, Fig. 3.9 also illustrates some of the most important processes that can be simulated using Monte Carlo methods, such as the hot electron generation and sidevalley electron transport. A Monte Carlo–drift-diffusion model described below was developed to perform a self-consistent study of hot electrons while also accounting for quasi-equilibrium hole transport.

The Monte Carlo–drift diffusion (MCDD) model combines the MC method of solving the Boltzmann transport equation and the DD model to enable modeling electron energy distributions and transport with the MC method while still retaining the simplicity of the DD model for holes. Figure 3.10 shows a schematic illustration of the simulation model, where the DD equations are first solved for both electrons and holes. After solving the DD equations, the hole density from DD is used as a fixed background charge in the MC simulation for electrons, while the electron and recombination rate densities from DD are used as initial values to achieve faster

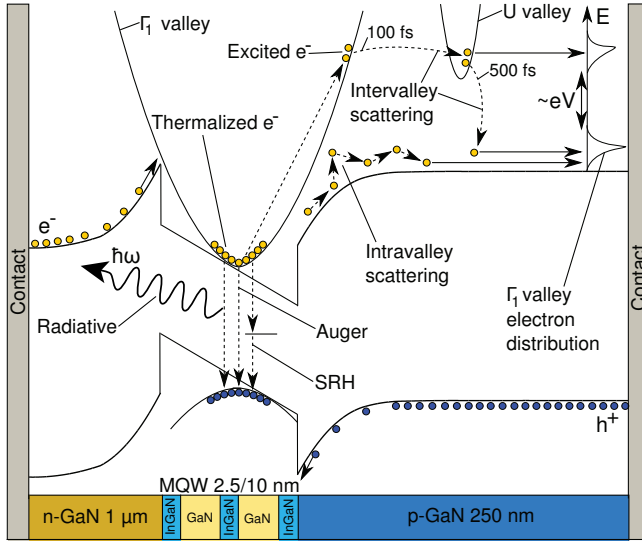


Figure 3.9. Schematic illustration of a typical MQW LED structure with three InGaN QWs, its band diagram (with a single QW for simplicity), and the most important mechanisms governing its operation and efficiency: band-to-band recombination, intraband scattering, and electron leakage. The experimentally measured high-energy electron leakage of Ref. [26] cannot be modeled only using the DD model, but direct methods to solve the BTE are required. Reprinted from Publication V with publisher's permission.

convergence.

The MC and DD steps use the same material parameters as Publication I where applicable. The MC simulation also considers all important intravalley and intervalley scattering mechanisms discussed in [64–67]. Intravalley phonon scattering results mainly from the deformation potential caused by low-energy acoustic phonons or longitudinal optical phonons (LO) with an energy of 92 meV, as piezoelectric scattering is negligible at 300 K. The intervalley phonon scattering is due to deformation potentials caused by optical phonons of 65 meV. In addition to scattering by phonons, the MC model considers ionized impurity scattering caused by dopant atoms, alloy disorder scattering in the InGaN QWs, electron-electron and electron-hole Coulomb interactions, and net recombination of electrons due to SRH, radiative, and Auger processes. In this work, the DD simulation of electrons only accounts for the lowest Γ_1 valley using a parabolic approximation with an effective mass of $0.2m_0$, whereas the MC simulation considers five separate valleys of the conduction bandstructure as described in Ref. [44] and Publications IV and V.

The inclusion of interband scattering processes in the same level of accuracy as the intraband processes is challenging, as it requires the an-

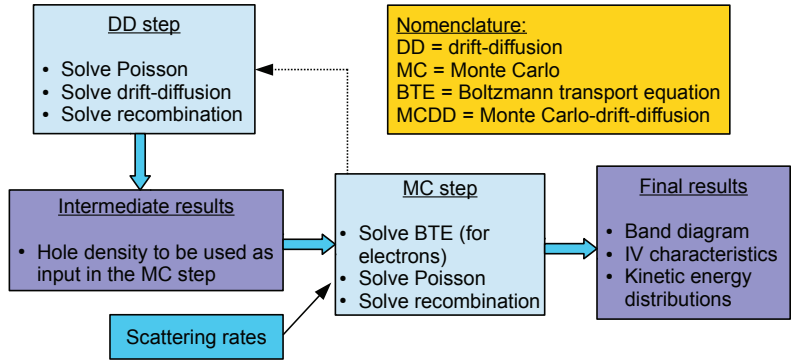


Figure 3.10. Schematic illustration of the Monte Carlo–drift-diffusion (MCDD) simulation model. The simulation starts by performing the DD simulation for electrons and holes. Hole density from the DD simulation is used as a fixed background charge for solving Poisson’s equation and recombination during the MC simulation. Final results contain device-level characteristics such as the IV characteristics, and also characteristics that the DD model cannot provide, such as the kinetic energy distributions of electrons. The dashed line denotes iteration between the DD and MC steps (not yet implemented in Publications IV and V) for more accurate results.

nihilation rates $W(E(\mathbf{k}))$ of electrons as well as the high energy electron generation probabilities $W(\mathbf{k}, \mathbf{k}')$ of the Auger processes, which are both difficult to obtain from theoretical and experimental data. In the MCDD model we use the semiquantitative ABC parametrization of recombination presented in Subsection 2.2.1. As the majority of the carriers is located within a narrow energy range near the bottom of the conduction band, they are assumed to have an equal probability of recombination. Also, the probabilities of the final states of the Auger-excited electrons are assumed to be independent of the initial wavevector, as most of the Auger events are indirect and involve phonons [22]. Based on these arguments, we use the rates obtained from the ABC model and the average n and p densities to annihilate randomly chosen electrons within a 100 meV energy band from the conduction band minimum. The Auger rate of hot electron generation is approximately given by $C_n n^2 p$, and it is also used to excite electrons within the same low-energy band.

Figure 3.11(a) compares the conduction band edges calculated for the III-N MQW LED of Fig. 3.9 either with the MCDD model (solid red curve) and by only using the DD model (blue dashed curve) at weak injection. The band edges are very close to each other, indicating that at weak injection levels the impact of hot electrons is small and the DD model suffi-

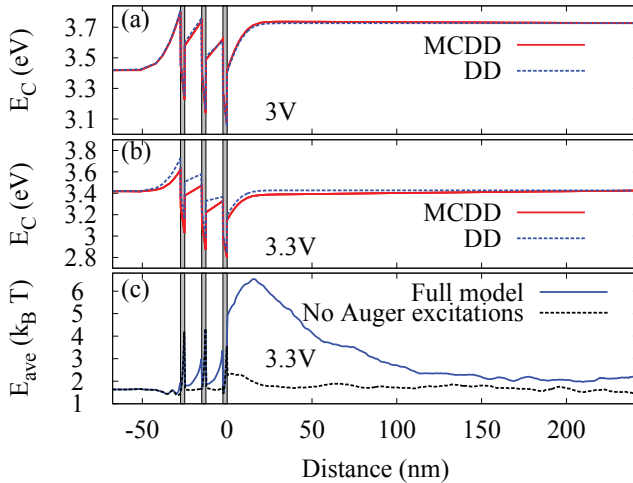


Figure 3.11. The conduction band edges calculated from the MCDD and DD models at (a) weak and (b) strong injection. (c) Average energy of electrons calculated from the conduction band minimum at strong injection, so that hot electron generation is either included or not included in the MCDD simulation. The QWs are marked with a grey background and the n- and p-sides are on the left and right sides of the MQW, respectively. Reprinted from Publication V with publisher's permission.

ciently describes the operation of the LED. On the other hand, Fig. 3.11(b) shows the conduction band edge from MCDD and DD models at high injection. The band edges are notably different from each other, revealing that there is a hot-electron population that affects the device operation. Figure 3.11(c) shows the average energy of electrons measured from the bottom of the conduction band at strong injection. The solid blue curve depicts results where Auger recombination is used to excite electrons, and the dashed black curve shows results where Auger-excited electrons are not accounted for. The figure indicates that Auger recombination generates a significant population of hot electrons in the device.

To study the spectral and spatial hot electron distribution at strong injection in more detail, Fig. 3.12(a) maps the distribution function of the electrons in the p-GaN layer next to the MQW. The distance in the y axis is measured from the top of the QWs, and the x axis shows the energy measured from the bottom of the conduction band, using the same scale as in Fig. 3.12(b). The U sidevalley minimum is located approximately at 1.5 eV, and the Γ_3 valley minimum is approximately at 1.75 eV. Figure 3.12(a) shows that there is a very large density of sidevalley electrons close to the MQW region, and it also shows that a significant part of the sidevalley electrons are able to travel to the p-contact without relaxing to the Γ valley. This confirms that there is a clear relative change in the high-energy

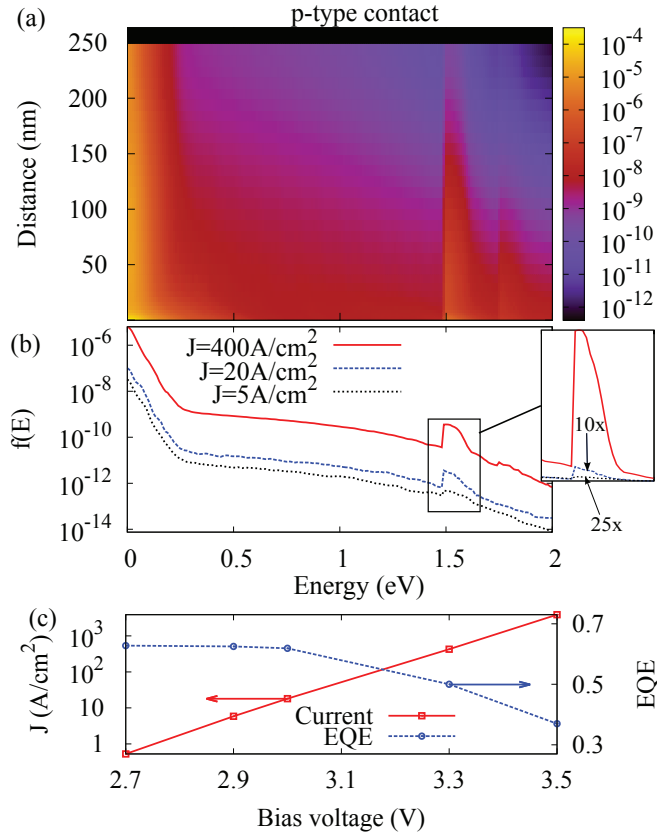


Figure 3.12. (a) Map of the electron distribution function in p-GaN as a function of the electron energy (x axis) and distance from the QWs (y axis). The U sidevalley is located approximately at 1.5 eV, and the Γ_3 valley is approximately at 1.75 eV. (b) The electron distribution function at the p-contact 250 nm from the QWs at weak injection close to the onset of the droop (5 A/cm^2 and 20 A/cm^2) and at strong injection (400 A/cm^2). Distribution functions around the minimum energy of the U valley are shown in the inset. (c) Current density (left y axis) and the EQE (right y axis) calculated using an extraction efficiency of 0.75 as a function of the applied bias voltage. Reprinted from Publication V with publisher's permission.

electron distribution at the p-contact due to Auger recombination, supporting the conclusions of Ref. [26]. However, quantitative comparison to measurements of Ref. [26] would require more detailed information about the cesiated surface and the sensitivity of the measurement setup. Figure 3.12 shows a 1-dimensional snapshot of the distribution function at different operating points at the p-contact located 250 nm from the MQW region. It shows that the sidevalley population of electrons at the p-contact emerges only at current densities corresponding roughly to the onset of the droop (cf. Fig. 3.12(c)). Figure 3.12(c) shows the IV characteristics and EQE calculated from the MCDD simulations.

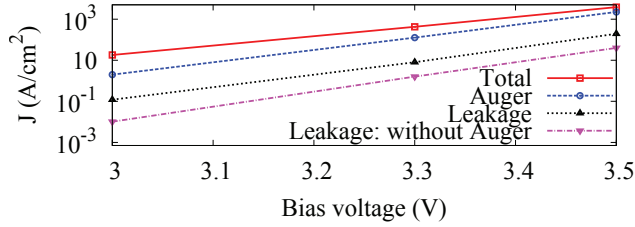


Figure 3.13. Total injection current, electron current created by Auger recombination in the QWs, and p-contact leakage current from simulations with and without including hot electron generation through Auger recombination. Reprinted from Publication V with publisher's permission.

As can be seen in Fig. 3.12, Auger recombination creates a leakage current component that travels towards the p-contact. To compare different loss currents obtained from the MCDD simulations, Fig. 3.13 shows the total electron current, part of the electron current created by Auger recombination, and the electron leakage current to the p-contact with and without accounting for electron generation through Auger recombination. Auger recombination increases significantly the leakage current which, however, is still significantly smaller than the recombination current created directly by Auger recombination. The leakage current is relatively small because only around half of all the Auger events excite electrons (other half exciting holes), and because many hot electrons scatter quickly and return to the QWs, where they can recombine again.

The Monte Carlo method is not subject to low-field and near-equilibrium approximations limiting the drift-diffusion model, and therefore it accounts for thermionic leakage and overflow of electrons. The results presented here strongly support the conclusion that major part of the efficiency droop is caused by Auger recombination rather than thermionic leakage or electron overflow. Auger recombination decreases the LED efficiency primarily by annihilating carriers nonradiatively in the QWs and secondarily by exciting secondary carriers to high-energy states where they can leak out from the QWs. Figure 3.13 shows that according to Monte Carlo simulations, the nonradiative current generated by Auger recombinations is significantly larger than hot electron leakage caused by Auger recombination. Due to the relatively small mobility of holes, the hole leakage current caused by Auger recombination not considered here is expected to be notably smaller than electron leakage.

3.2 Physics of new III-N devices

This Subsection and Publications VI-IX study unconventional device structures to improve the efficiency and functionality of III-N LEDs. The studies focus on two promising unconventional device concepts: structures utilizing bipolar diffusion injection with active regions located outside the pn junction, and devices using polarization doping to mimic pn junctions. Such structures may enable, e.g., efficient LEDs with very large unbroken emission areas, freestanding nanowire structures with no top contacts, higher hole densities in p-GaN, reduced transport losses in the barrier layers, and improved carrier distributions in active regions.

3.2.1 Current injection by bipolar diffusion

III-N light-emitting structures based on nanowires, plasmonic gratings, and other near-surface nanostructures are expected to improve light extraction and tunability of the emission spectrum, and also to decrease the efficiency droop [103–110]. However, if the ARs of such devices are excited electrically using the conventional 1-dimensional current injection scheme used in LEDs, the nanowires need to be contacted from top and the plasmonic gratings need to be located very close to electrical contacts, resulting in inefficient carrier injection. Publications VI-VIII present a concept of bipolar diffusion injection to demonstrate an alternative solution to these challenges.

The conventional current injection to LEDs relies on the AR being sandwiched between p- and n-type regions, so that electrons and holes enter it from different sides. However, in Publications VI and VII we carry out theoretical and numerical calculations of current transport in unconventional structures where the AR is placed on the device surface outside the pn junction. More specifically, we study current transport in freestanding nanowire emitter structures (NWR) shown in Fig. 3.14. Publication VIII also presents the first experimental demonstration of light-emitting QWs that are excited by bipolar diffusion. These results suggest that bipolar diffusion injection may enable overcoming many of the limitations of the conventional current injection scheme.

Before discussing numerical results, we show using analytical considerations how the electrons and holes are diffused from the depletion region to the wires in the NWR structures. For current transport in the n-NWR structure of Fig. 3.14, the electron leakage current to the p-contact can

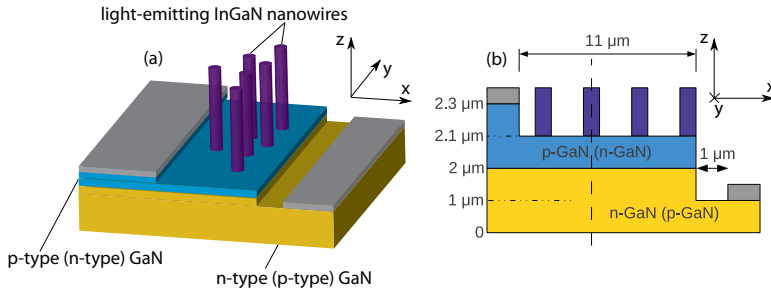


Figure 3.14. (a) Freestanding n-type (p-type) nanowire emitter structure. The structure is referred to as n-NWR (p-NWR), where n (p) denotes the polarity of the minority carriers that need to diffuse to the wires through a potential barrier of opposite doping. (b) shows the dimensions used in the simulations. Reprinted from Publication VII with publisher's permission.

be approximated by the short diode law (see, e.g., Ref. [111]), that can be written as

$$I = eA_p \frac{D_n}{L_p} n_p \left(\exp \left[\frac{eV_a}{k_B T} \right] - 1 \right), \quad (3.8)$$

where A_p is the cross-section area of the p-contact, L_p is the distance between the edge of the p-side depletion region and the p-contact, and n_p is the minority electron density at the edge of the depletion region at zero bias. Due to the smaller bandgap and the large density of holes next to the wires, recombination in the wires acts as a similar drain for electrons as the p-contact. Therefore the electron diffusion current to the wires resulting in recombination can be approximated by a similar short diode like equation, but A_p and L_p must be replaced by the total cross-section area of the wires and the distance between the wires and the edge of the p-side depletion region, respectively. Hole leakage to the n-contact is typically negligible due to the geometry and small hole mobility, but hole diffusion to the wires is not similarly limited due to the p-type doping next to the wires.

Accounting for relevant currents in the n-NWR structure, its injection efficiency can be approximated as

$$\eta_{INJ} = \frac{A_{ar}/L_{ar}}{A_{ar}/L_{ar} + A_p/L_p}, \quad (3.9)$$

where A_{ar} is the cross-sectional area of the wires and L_{ar} is the distance between the wires and the edge of the depletion region (see Publication VI). It is seen that the injection efficiency can be high if the areas of the p-contact and the wires are optimized and if the wires are closer than the contacts to the pn junction. Similar arguments can be used to derive

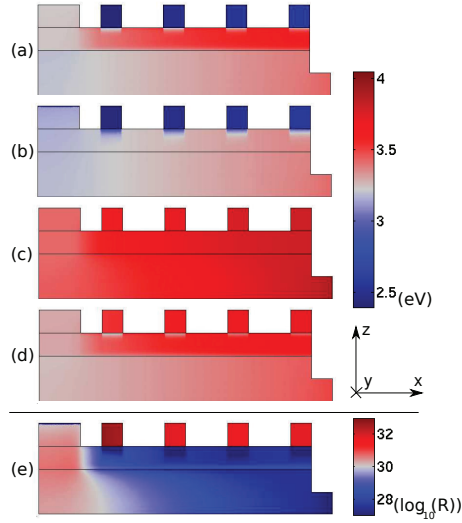


Figure 3.15. Maps of the (a) conduction band edge E_c , (b) conduction band quasi-Fermi level E_{F_n} , (c) valence band quasi-Fermi level $E_{F_p} + eV_a$ shifted by an energy corresponding to the applied voltage $V_a = 3.5$ V, (d) shifted valence band edge $E_v + eV_a$, and (e) 10-base logarithm of the recombination rate in the n-NWR structure. Figures (a) and (b) show that E_c and E_{F_n} are very close to each other everywhere except for the p-GaN layer, indicating that electrons are indeed diffusing to the wires. Figure (e) shows that most of the recombination takes place in the wires. Reprinted from Publication VII with publisher's permission.

the injection efficiency of the p-NWR structure, and it also contains the doping densities and diffusion constants.

Equation (3.9) is based on simple arguments, and numerical simulations are needed to study bipolar diffusion in more detail. We have simulated current transport in the 2D equivalent of the NWR structures shown in Fig. 3.14 using the drift-diffusion model described in Chapter 2. Figure 3.15 shows a map of the (a) conduction band minimum E_c , (b) conduction band quasi-Fermi level E_{F_n} , (c) shifted valence band quasi-Fermi level $E_{F_p} + eV_a$, (d) shifted valence band maximum $E_v + eV_a$, and (e) 10-base logarithm of the recombination rate in the n-NWR structure at 3.5 V. Figures 3.15(a) and (b) show that E_c and E_{F_n} are very close to each other everywhere except for the p-GaN layer, indicating that electrons are indeed diffusing to the wires. E_{F_p} and E_v are also close to each other in the wires, indicating that holes transport there from the adjacent p-type layer. The high voltage of 3.5 V is chosen to show that at high injection, there are resistive losses resulting in horizontal gradients in the bands and seen as color gradients in the maps.

Figure 3.16(a) shows the total current density and the part of the cur-

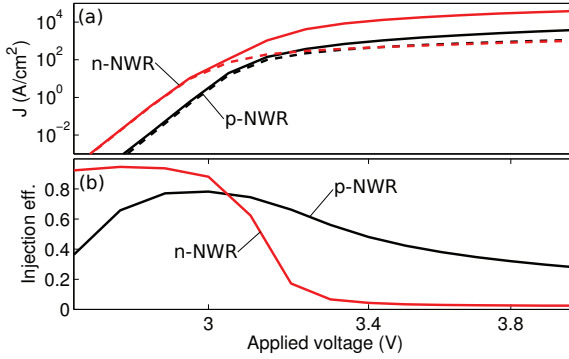


Figure 3.16. (a) Current density (solid lines) and recombination current density (dashed lines), and (b) injection efficiency vs. applied voltage in the NWR structures. Reprinted from Publication VII with publisher's permission.

rent density that results in recombination in the wires. The two current components start to deviate from each other roughly at voltages larger than the built-in potential of the structure, which is 3.29 V. Up to that voltage, the bias voltage increases the diffusion of carriers to the wires and contacts according to the short diode law of Eq. (3.8). On the other hand, voltages larger than the built-in potential mainly enhance the lateral electric field seen in Figs. 3.15 and carrier leakage but they do not increase diffusion to the wires. Figure 3.16(b) shows the injection efficiency of the NWR structures. The maximum injection efficiency is higher in the n-NWR structure due to larger mobility of electrons, but both curves show relatively high injection efficiencies. Engineering of the bands is expected to result in injection efficiencies close to unity, as long as the diffusion lengths, polarization-induced potential barriers, and leakage current paths are carefully considered.

Publication VIII presents an experimental demonstration of a III-N MQW LED, where the QWs are excited through bipolar diffusion. The structure is shown in Fig. 3.17, and the MQW responsible for blue light emission is located roughly 100 nm below the pn junction. For blue light emission, holes have to diffuse through the n-type GaN to reach the QWs.

Figure 3.18 (a) shows the measured spectrum of the LED of Fig. 3.17 at two different injection currents, and the inset shows the optical power as a function of the injection current. At an injection current of 160 mA the spectrum peaks strongly at the wavelength of approx. 450 nm, which corresponds to the bandgap of the InGaN QWs and indicates that practically all the light is emitted from them. The QWs are only excited through bipolar diffusion, and therefore the emission spectrum confirms

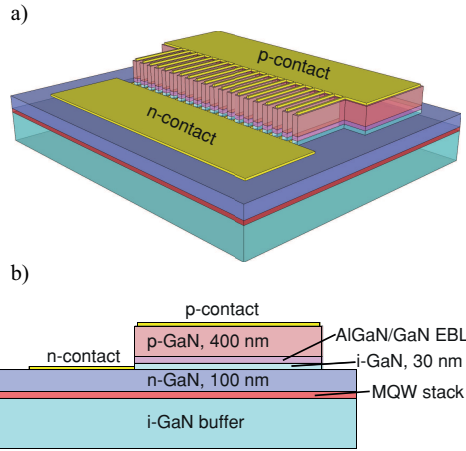


Figure 3.17. (a) Schematic illustration and (b) layer structure of the MQW LED of Publication VIII excited by bipolar diffusion. The light-emitting QWs are located roughly 100 nm below the pn junction. Reprinted from Publication VIII with publisher's permission.

that holes diffuse through n-type GaN to the QWs. Emission at 20 mA has a broad yellow band, which can result from several different phenomena, e.g., shallow dopants in n-GaN, carbon impurities in i-GaN, or gallium vacancy complexes in i-GaN. Figure 3.18(b) shows an optical microscope image of the LED at low injection current, where the emitted light is predominantly yellow. Figure 3.18(c) shows the LED at a high injection current, where it emits blue light from the QWs.

Figure 3.19 shows the electron and hole densities for the LED structure of Fig. 3.17 obtained from 2-dimensional drift-diffusion simulations. The densities are calculated for the maximum IQE condition. The hole density decreases in the n-type GaN as a function of the distance from p-type GaN. However, the MQW region has a significant density of holes, enabling radiative recombination and light emission. Carrier densities in the unintentionally doped i-GaN region below the MQW are very small, and simulations confirm that neither electron nor hole current is circulated through the i-GaN region.

The results presented here were calculated for semiconductor structures with homogeneous layers and abrupt material interfaces. The bipolar injection concept could, however, benefit from using graded layers of wurtzite GaN to introduce polarization doping and to decrease potential barriers, as described in the next Subsection.

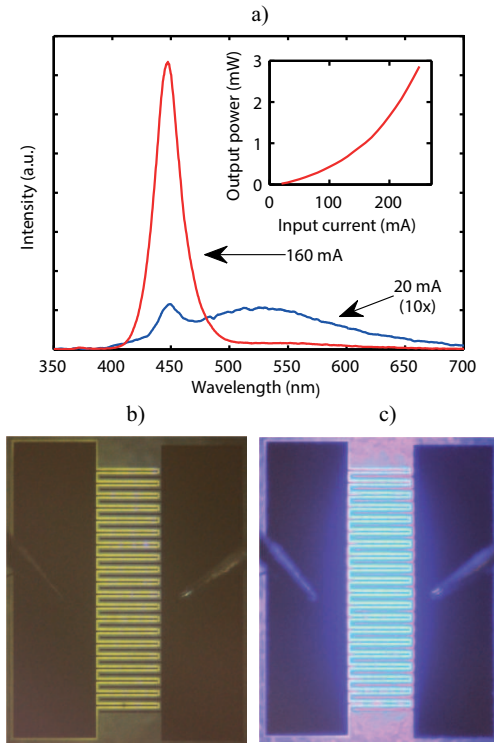


Figure 3.18. (a) Electroluminescence spectra of the MQW LED shown in Fig. 3.17 at two different injection currents, and optical output power as a function of the injection current shown in the inset. Optical microscope images of the LED at (b) low and (c) high injection current. Reprinted from Publication VIII with publisher’s permission.

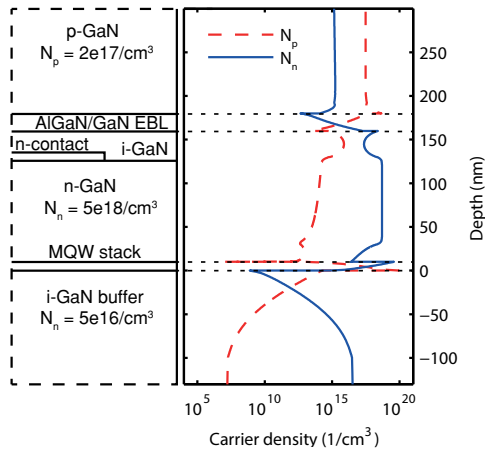


Figure 3.19. Electron (N_n) and hole (N_p) densities obtained from the simulations at the current density corresponding to the maximum IQE. The schematic layer structure is shown on the left together with ionized doping levels. Reprinted from Publication VIII with publisher’s permission.

3.2.2 Polarization-doped LED structures

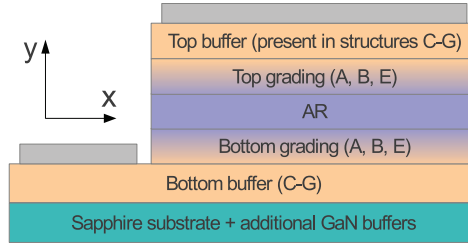
In this Subsection we analyze III-N LED structures where part or even all of the impurity doping is replaced by polarization-induced doping. Example structures A, B, and E shown in Fig. 3.20 contain graded material layers, which in polar wurtzite GaN material results in a similar creation of free carriers as the typical impurity doping. Polarization doping has been previously reported to induce free carriers in III-N structures [112–116] and even used to fabricate pn diodes without any impurity doping [107, 117, 118], but simulations of polarization-doped LEDs have only discussed the advantages of large hole densities enabled by polarization [119].

In Publication IX, the operation of LEDs shown in Fig. 3.20 was simulated. The AlGaIn/GaN structures A and B have no impurity doping, and their free carriers are generated purely through the polarization gradient in the 100 nm thick graded regions. The corresponding impurity-doped structures C and D, on the other hand, only have homogeneous layers. Structure E has graded layers of only 10 nm, since thicker InGaIn layers are very difficult to grow on GaN due to the large lattice mismatch. The corresponding structures F and G have impurity-doped GaN layers next to the AR. All the samples are assumed to be grown Ga-face in the [0001] direction, which is the typical case for LEDs grown on sapphire substrates.

To demonstrate analytically how compositional grading of a III-N material in the polar direction results in free electrons and holes, we use the equations provided in Ref. [57]. Based on the equations presented there, the intrinsic polarization including the spontaneous and piezoelectric contributions has a weakly nonlinear and monotonous dependence on the alloy composition. Assuming that the material is graded linearly in the y direction of Fig. 3.20 between two material compositions, the polarization has an approximately constant derivative dP_{tot}/dy . Poisson's equation can be written for the graded layer as

$$\frac{d}{dy} \left(-\varepsilon \frac{d}{dy} \phi \right) = e \left(p - n + N_d - N_a - \frac{1}{e} \frac{dP_{tot}}{dy} \right), \quad (3.10)$$

where the constitutive relation $\mathbf{D} = -\varepsilon \nabla \phi + \mathbf{P}_{tot}$ has been used, with ε accounting for the polarizability of the material and \mathbf{P}_{tot} containing the spontaneous and piezoelectric polarization. In Eq. (3.10), the polarization gradient provides an additional approximately constant charge density in



Sample	Bottom buffer	Bottom grading	AR	Top grading	Top buffer
	100 nm	100 nm	5 nm	100 nm	100 nm
A	N/A	GaN→AlGaN	GaN	AlGaN→GaN	N/A
B	N/A	AlGaN→GaN	GaN	GaN→AlGaN	N/A
C	n-AlGaN	N/A	GaN	N/A	p-AlGaN
D	p-AlGaN	N/A	GaN	N/A	n-AlGaN
	100 nm	10 nm	5 nm	10 nm	100 nm
E	p-GaN	GaN→InGaN	InGaN	InGaN→GaN	n-GaN
F	n-GaN	N/A	InGaN	N/A	p-GaN
G	p-GaN	N/A	InGaN	N/A	n-GaN

Figure 3.20. Schematic cross-section of the $\text{Al}_{0.3}\text{Ga}_{0.7}\text{N}/\text{GaN}$ and $\text{GaN}/\text{In}_{0.15}\text{Ga}_{0.85}\text{N}$ structures simulated to demonstrate the effects of polarization doping on the efficiency of light-emitting devices. The table shows the layer compositions and thicknesses of different samples. Samples A, B, and E contain graded layers which provide an additional charge density in addition to impurity doping. Reprinted from Publication IX with publisher's permission.

addition to the impurity doping. In the graded AlGaN/GaN structures A and B of Fig. 3.20, the absolute value of the polarization doping density $|dP_{tot}/(edy)|$ is approx. $6 \cdot 10^{23} \text{ 1/m}^3$, while in the graded GaN/InGaN structure E it is approx. $4 \cdot 10^{24} \text{ 1/m}^3$. The drift-diffusion simulations also included the overlap factor of the electron and hole ground state envelope wave functions, as discussed in Subsection 2.2.3.

Figure 3.21 shows the band diagrams of the AlGaN/GaN structures at zero bias (left panel) and at operating points corresponding to their maximum IQE (right panel). Structure A has a gradient in the bandgap in the graded layers, but due to the direction of grading it still has an abrupt band discontinuity next to the QW. Structure B, on the other hand does not have any abrupt changes in the QW and even not a well-defined QW. Structures C and D have band diagrams typical to impurity-doped LEDs, but their doping profiles are reversed with respect to one another. The right panel shows that structures A, C, and D have large polarization-induced electric fields in the AR which cause substantial electron-hole separation. Structures A and C also exhibit quasi-Fermi losses next to the AR. Structure B, on the other hand, has practically no electric field in its AR, which is expected to enhance its recombination rate as compared

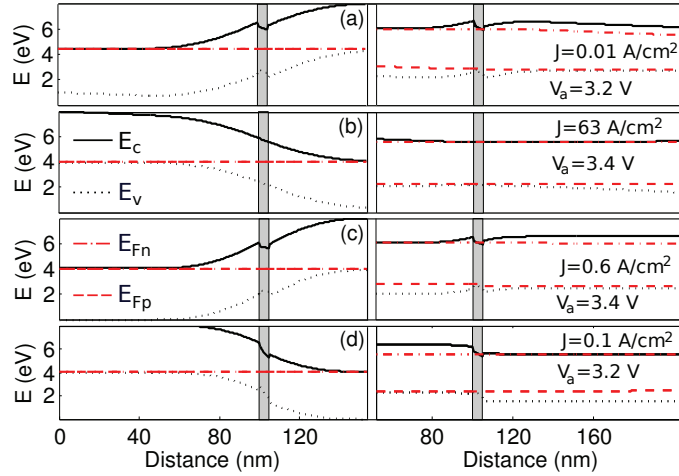


Figure 3.21. Band diagram of structure (a) A, (b) B, (c) C, and (d) D at zero applied bias (left panel) and at an operating point corresponding to the maximum IQE. Structures A and C have the n- and p-type regions on different sides than structures B and D. Operating points are indicated in the figures. Reprinted from Publication IX with publisher's permission.

to the other structures. Band diagrams of the GaN/InGaN structures are qualitatively similar to those in Fig. 3.21.

Electric field in the QW AR present in Figs. 3.21(a), (c), and (d) results in the ground state wave function of electrons (holes) to be shifted towards the minimum (maximum) of the conduction (valence) band in the QW. It also makes the emission wavelength dependent on the operating point because of the quantum-confined Stark effect (QCSE) and reduces the recombination rate. Figure 3.22 shows the QCSE for all the structures that have a QW AR (all the structures except B and E). The electric field and the corresponding separation of electron and hole ground states in the QWs causes the effective band gap to be notably smaller than the bulk bandgap (marked with a dashed line). Figure 3.22(b) shows the squared overlap factors in the GaN and InGaN QWs of structures A, C, D, and F, G for typical electric fields present in the simulations. The small overlap factors in these structures decrease the recombination rates and also the current density at which the IQE reaches its maximum. The inset of (b) shows the electron and hole ground state wave functions for a case where the squared overlap factor is approx. 0.1.

Figure 3.23 plots the IQE vs. injection current density for (a) structures A-D and (b) structures E-G. Polarization-doped structures B and E have notably larger injection currents corresponding to their maximum efficiency (i.e. smaller droop) than their impurity-doped counterparts. In

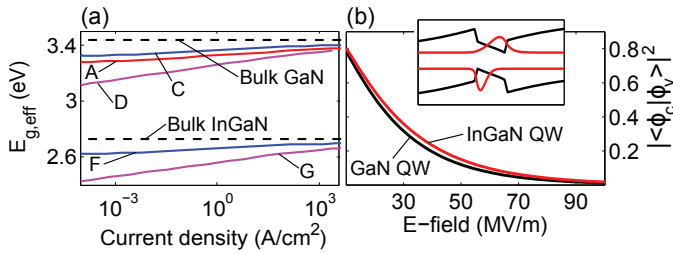


Figure 3.22. (a) Energy difference between the electron and hole ground states in the ARs of structures with QWs. Also shown is the band gap of the bulk material constituting the AR. (b) Squared overlap factor of electrons and holes in GaN and InGaN QWs as a function of the electric field, with the inset showing the electron and hole ground state wave functions in the QW of structure C at its maximum IQE. Based on the simulations, the electric fields in the QWs range from 10 MV/m at high injection currents to 100 MV/m at very low injection currents. Reprinted from Publication IX with publisher's permission.

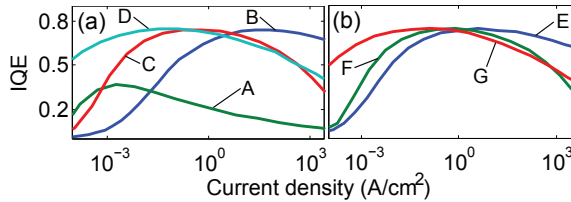


Figure 3.23. IQE of (a) structures A-D and (b) structures E-G. Structures B and E with polarization doping and small electric field in the AR have notably larger injection currents corresponding to their maximum IQE than other structures. Reprinted from Publication IX with publisher's permission.

structures A, C, D, F, and G, strong localization of electrons and holes to different sides of the QW and the resulting reduced overlap integral decreases the recombination rates and therefore also moves their peak IQE to smaller currents. Polarization-doped structure A also has a small peak IQE due to a large leakage current caused by the gradient in the conduction band at the p-side as seen in Fig. 3.21(a).

Polarization doping in LEDs has several benefits in terms of improved electron-hole wave function overlaps and smaller droop. These benefits could also prove very useful when combined with structures utilizing bipolar diffusion injection. Grading the material between the pn junction and the active region in bipolar diffusion injected devices might allow decreasing the potential barriers and facilitate bipolar diffusion to the active region.

3.3 Discussion

3.3.1 Implications and future research

The results of this work suggest that the efficiency droop of III-N LEDs is caused by very fundamental physical processes that cannot be completely removed by material quality improvements or structure optimization. Auger recombination seems to be a very large contributor to droop, mainly by providing a powerful nonradiative loss mechanism but to some extent also because it generates high-energy carriers that can leak out from the active regions. Based on our results, the most attractive way to minimize the effects of droop is to design structures where carriers are spread more evenly over larger active regions or larger number of QWs than in present-day structures. On the other hand, even though recent measurements and the results of this work favor Auger recombination as the largest single contributor to the efficiency droop, more detailed measurements and theoretical device models are still needed to understand the physics of the efficiency droop in enough detail. The self-consistent Monte Carlo–drift-diffusion model developed in this work is one of the steps in that direction.

The results also show that voltage losses inside LED device structures are a good candidate to explain the experimentally measured uneven emission from MQW active regions and elevated bias voltages. Even if the drift-diffusion simulations performed in this work might not include all the details needed to quantitatively model voltage losses inside MQW structures, the phenomenon seems to be real and have significant consequences in device operation. Analysis of measurement data by fitting the common ABC model can give intuitive and sometimes semi-quantitative relation between the current of an LED and its recombination rates. However, challenges of fitting theoretical current-voltage models to measurement data show that the current-voltage relationship of modern LEDs is not understood well enough even though it has notable effects on the device operation.

To reduce droop by evenly spreading carriers between all the QWs in LEDs, one needs full understanding of the details related to voltage losses for minimizing the effects of the droop. The unconventional device structures proposed in this thesis based on bipolar diffusion injection and polarization doping offer potential solutions to reduce the efficiency droop

and develop efficient and scientifically interesting functional next-generation LEDs. Bipolar diffusion injection may allow, e.g., efficient near-surface nanostructure emitters and large unbroken emitting/absorbing areas, and polarization doping may improve carrier transport and spreading. The initial experimental results of this work show that the bipolar diffusion injection principle works, but untangling and achieving the full potential of bipolar diffusion injection and polarization doping still requires extensive future work.

3.3.2 Reliability and accuracy of results

To balance the partly conflicting goals to provide fundamental insight and device-level understanding needed in designing new device concepts, the models in this work have been kept as simple as possible. Therefore most of the modeling is based on the well-known phenomenological drift-diffusion model together with semiempirical models for recombination. For studies of Auger recombination and high-energy electrons, the Monte Carlo model is used for accurate physical treatment. The results also contain inaccuracies mostly due to excluding quantum transport effects but also due to uncertainty in the material parameters especially in the values of polarization, band offsets, and semiempirical intra- and interband scattering rates.

Especially the quantitative reliability of the drift-diffusion model is in part undermined by the simplifications included. However, comparisons to available measurements suggest that the model reproduces phenomenologically correct behaviour. For example, dominant emission from QWs closest to the p-contact and elevated forward voltages with many QWs are observed experimentally and also reproduced by drift-diffusion simulations. On the other hand, also comparison with results from Monte Carlo simulations and experiments show that the drift-diffusion model generally gives qualitatively and in some cases even quantitatively reliable predictions. It is, however, clear that the multiphysics approach integrating the drift-diffusion and Monte Carlo methods with first-principle bandstructure models and scattering rates should be the long term goal in the device physics of LEDs.

4. Conclusions

The availability of affordable LED lamps with performance surpassing most traditional lighting technologies has started a solid-state lighting revolution, where almost all traditional light sources are gradually being replaced by LEDs. Combined with the development of the closely related technologies such as photovoltaics and integrated optics, LEDs will therefore play a major role in reducing the global dependence on fossil fuels and enabling new photonic applications. However, releasing the full potential of LEDs requires further optimization of materials and devices.

In this thesis, the operation of III-Nitride light-emitters was studied by using theoretical models and numerical simulations based on semiconductor transport equations and by analyzing measurement data and experiments. The models were used to investigate current transport losses and their effects in typical MQW structures, to characterize the internal parameters of LEDs, and to study the relationship between Auger recombination, hot electrons, and efficiency droop. In addition to conventional MQW LEDs, the operation and potential benefits of unconventional devices utilizing bipolar diffusion injection and polarization doping were studied by simulations and experiments.

The results of this work support the hypothesis that Auger recombination is the main cause of the efficiency droop. However, many other factors affect the efficiency droop as well, and detailed measurements connected to improved theoretical models are still needed to understand the detailed mechanisms of the droop. The results also suggest that efficient carrier transport and current spreading in LEDs is hampered by losses caused by transport over large potential barriers. These losses are also visible in experiments as uneven emission from MQW structures and elevated operating voltages resulting from additional QWs, and they are expected to become an important factor in optimizing LEDs after the quantum ef-

efficiency has increased close to its theoretical maximum.

The structures based on bipolar diffusion injection studied in this thesis are presently under early development, but in the future they may enable LEDs with very large emitting areas and efficient current injection to near-surface nanostructures. Combined with polarization doping, the new device concepts may also allow for very efficient current transport and optimized carrier spreading. The bipolar diffusion injection and polarization doping are also expected to have potential in highly efficient photovoltaic applications, where e.g. freestanding nanowires can be used for efficient trapping of the incoming light.

As the peak efficiency of LEDs is already quite close to its theoretical limits, future development of LEDs will rely on reducing the droop and increasing the efficiency of LEDs especially at high powers. For achieving these goals, experimental methods and detailed physical models need to be carefully combined. The Monte Carlo–drift-diffusion model developed in this thesis is one of the first steps towards detailed studies of the efficiency droop, and the prototype structure demonstrating bipolar diffusion injection is one example of successfully combining experimental and theoretical work to develop new solutions for fabricating devices that might not suffer from droop as strongly as conventional devices.

Bibliography

- [1] European Commission, *Energy Roadmap 2050*. Publications Office of the European Union, 2012.
- [2] S. Rahmlow, “Erneuerbare Energien erreichen neuen Rekordwert,” *BDEW Bundesverband der Energie- und Wasserwirtschaft*, July 2014.
- [3] G. Parkinson, “Renewables surge to 74% of German demand on Sunday,” *RenewEconomy*, May 2014.
- [4] G. Barbose *et al.*, *SunShot Vision Study*. U.S. Department of Energy, 2012.
- [5] U.S. Energy Information Administration, *Annual Energy Outlook 2014*. U.S. Department of Energy, 2014.
- [6] Navigant Consulting, Inc., *Energy Savings Potential of Solid-State Lighting in General Illumination Applications*. Solid-State Lighting Program, U.S. Department of Energy, 2012.
- [7] N. Bardsley, S. Bland, L. Pattison, M. Pattison, K. Stober, F. Welsh, and M. Yamada, *Solid-State Lighting Research and Development Multi-Year Program Plan*. U.S. Department of Energy, 2014.
- [8] S. Pimputkar, J. S. Speck, S. P. DenBaars, and S. Nakamura, “Prospects for LED lighting,” *Nat. Photonics*, vol. 3, pp. 180–182, 2009.
- [9] S. Nakamura and M. R. Krames, “History of Gallium–Nitride-Based Light-Emitting Diodes for Illumination,” *Proc. IEEE*, vol. 101, pp. 2211–2220, 2013.
- [10] T.-Y. Seong, J. Han, H. Amano, and H. Morkoc, *III-Nitride Based Light Emitting Diodes and Applications*. Springer, 2013.
- [11] SORAA, Inc., “Soraa develops the world’s most efficient LED; begins integration into large lamp line.” Press Release, February 2014.
- [12] Y.-L. Li, Y.-R. Huang, and Y.-H. Lai, “Efficiency droop behaviors of InGaN/GaN multiple-quantum-well light-emitting diodes with varying quantum well thickness,” *Appl. Phys. Lett.*, vol. 91, p. 181113, 2007.
- [13] M.-H. Kim, M. F. Schubert, Q. Dai, J. K. Kim, E. F. Schubert, J. Piprek, and Y. Park, “Origin of efficiency droop in GaN-based light-emitting diodes,” *Appl. Phys. Lett.*, vol. 91, p. 183507, 2007.

- [14] M. F. Schubert, J. Xu, J. K. Kim, E. F. Schubert, M. H. Kim, S. Yoon, S. M. Lee, C. Sone, T. Sakong, and Y. Park, "Polarization-matched GaInN/AlGaInN multi-quantum-well light-emitting diodes with reduced efficiency droop," *Appl. Phys. Lett.*, vol. 93, p. 041102, 2008.
- [15] X. Ni, Q. Fan, R. Shimada, U. Özgür, and H. Morkoc, "Reduction of efficiency droop in InGaN light emitting diodes by coupled quantum wells," *Appl. Phys. Lett.*, vol. 93, p. 171113, 2008.
- [16] S.-H. Han, D.-Y. Lee, S.-J. Lee, C.-Y. Cho, M.-K. Kwon, S. P. Lee, D. Y. Noh, D.-J. Kim, Y. C. Kim, and S.-J. Park, "Effect of electron blocking layer on efficiency droop in InGaN/GaN multiple quantum well light-emitting diodes," *Appl. Phys. Lett.*, vol. 94, p. 231123, 2009.
- [17] A. David and M. J. Grundmann, "Droop in InGaN light-emitting diodes: A differential carrier lifetime analysis," *Appl. Phys. Lett.*, vol. 96, p. 103504, 2010.
- [18] J. Oksanen and J. Tulkki, "Drooping as a simple characterization tool for extraction efficiency and optical losses in light emitting diodes," *Appl. Phys. Lett.*, vol. 97, p. 131105, 2010.
- [19] J. Piprek, "Efficiency droop in nitride-based light-emitting diodes," *Phys. Status Solidi A*, vol. 207, pp. 2217–2225, 2010.
- [20] J. Hader, J. V. Moloney, and S. W. Koch, "Density-activated defect recombination as a possible explanation for the efficiency droop in GaN-based diodes," *Appl. Phys. Lett.*, vol. 96, p. 221106, 2010.
- [21] J. Hader, J. V. Moloney, and S. W. Koch, "Temperature-dependence of the internal efficiency droop in GaN-based diodes," *Appl. Phys. Lett.*, vol. 99, p. 181127, 2011.
- [22] E. Kioupakis and P. Rinke and K. T. Delaney and C. G. Van de Walle, "Indirect Auger recombination as a cause of efficiency droop in nitride light-emitting diodes," *Appl. Phys. Lett.*, vol. 98, p. 161107, 2011.
- [23] M. Deppner, F. Römer, and B. Witzigmann, "Auger carrier leakage in III-nitride quantum-well light emitting diodes," *Phys. Status Solidi RRL*, vol. 6, pp. 418–420, 2012.
- [24] E. Kioupakis, Q. Yan, and C. G. V. de Walle, "Interplay of polarization fields and Auger recombination in the efficiency droop of nitride light-emitting diodes," *Appl. Phys. Lett.*, vol. 101, p. 231107, 2012.
- [25] A. Olsson, A. Aierken, J. Oksanen, S. Suihkonen, H. Lipsanen, and J. Tulkki, "Temperature dependence of droop onset in optically pumped intrinsic InGaAs/InP heterostructures," *Appl. Phys. Lett.*, vol. 102, p. 081123, 2013.
- [26] J. Iveland, L. Martinelli, J. Peretti, J. S. Speck, and C. Weisbuch, "Direct Measurement of Auger Electrons Emitted from a Semiconductor Light-Emitting Diode under Electrical Injection: Identification of the Dominant Mechanism for Efficiency Droop," *Phys. Rev. Lett.*, vol. 110, p. 177406, 2013.

- [27] M. Binder, A. Nirschl, R. Zeisel, T. Hager, H.-J. Lugauer, M. Sabathil, D. Bougeard, J. Wagner, and B. Galler, "Identification of nnp and npp Auger recombination as significant contributor to the efficiency droop in (GaIn)N quantum wells by visualization of hot carriers in photoluminescence," *Appl. Phys. Lett.*, vol. 103, p. 071108, 2013.
- [28] D. S. Meyaard, G.-B. Lin, J. Cho, E. F. Schubert, H. Shim, S.-H. Han, M.-H. Kim, C. Sone, and Y. S. Kim, "Identifying the cause of the efficiency droop in GaInN light-emitting diodes by correlating the onset of high injection with the onset of the efficiency droop," *Appl. Phys. Lett.*, vol. 102, p. 251114, 2013.
- [29] J. Piprek, "LED droop: a critical review and novel solution," *Compound Semiconductor*, July 2014.
- [30] S. Suihkonen, *Fabrication of InGaN quantum wells for LED applications*. PhD thesis, Helsinki University of Technology, 2008.
- [31] S. Nakamura and G. Fasol, "Background," in *The Blue Laser Diode*, pp. 7–20, Springer, 1997.
- [32] T. Paskova, D. A. Hanser, and K. R. Evans, "GaN Substrates for III-Nitride Devices," *P. IEEE*, vol. 98, pp. 1324–1338, 2010.
- [33] R. J. Molnar, W. Götz, L. T. Romano, and N. M. Johnson, "Growth of gallium nitride by hydride vapor-phase epitaxy," *J. Cryst. Growth*, vol. 178, pp. 147–156, 1997.
- [34] R. Dwilinski, R. Doradzinski, J. Garczynski, L. P. Sierzputowski, A. Puchalski, Y. Kanbara, K. Yagi, H. Minakuchi, and H. Hayashi, "Excellent crystallinity of truly bulk ammonothermal GaN," *J. Cryst. Growth*, vol. 310, pp. 3911–3916, 2008.
- [35] S. Pimputkar, S. Kawabata, J. S. Speck, and S. Nakamura, "Surface morphology study of basic ammonothermal GaN grown on non-polar GaN seed crystals of varying surface orientations from m-plane to a-plane," *J. Cryst. Growth*, vol. 368, pp. 67–71, 2013.
- [36] S. Pimputkar, S. Kawabata, J. S. Speck, and S. Nakamura, "Improved growth rates and purity of basic ammonothermal GaN," *J. Cryst. Growth*, vol. 403, pp. 7–17, 2014.
- [37] Y. Mori, M. Imade, K. Murakami, T. Takazawa, H. Imabayashi, Y. Todoroki, K. Kitamoto, M. Maruyama, M. Yoshimura, Y. Kitaoka, and T. Sasaki, "Growth of bulk GaN crystal by Na flux method under various conditions," *J. Cryst. Growth*, vol. 350, pp. 72–74, 2012.
- [38] F. Kawamura, M. Morishita, M. Tanpo, M. Imade, M. Yoshimura, Y. Kitaoka, Y. Mori, and T. Sasaki, "Effect of carbon additive on increases in the growth rate of 2 in GaN single crystals in the Na flux method," *J. Cryst. Growth*, vol. 310, pp. 3946–3949, 2008.
- [39] R. W. Robinett, *Quantum Mechanics : classical results, modern systems, and visualized examples*. Oxford University Press, 2006.
- [40] N. W. Ashcroft and N. D. Mermin, *Solid State Physics*. CBS Publishing, 1988.

- [41] S. L. Chuang, *Physics of Photonic Devices*. John Wiley & Sons, Inc., Hoboken, New Jersey, 2009.
- [42] R. Wang, P. P. Ruden, J. Kolnik, I. Oguzman, and K. F. Brennan, "Dielectric properties of wurtzite and zincblende structure gallium nitride," *J. Phys. Chem. Solids*, vol. 58, pp. 913–918, 1997.
- [43] M. Piccardo, L. Martinelli, J. Iveland, N. Young, S. P. DenBaars, S. Nakamura, J. S. Speck, C. Weisbuch, and J. Peretti, "Determination of the first satellite valley energy in the conduction band of wurtzite GaN by near-band-gap photoemission spectroscopy," *Phys. Rev. B*, vol. 89, p. 235124, 2014.
- [44] J. D. Albrecht, R. P. Wang, P. P. Ruden, M. Farahmand, and K. F. Brennan, "Electron transport characteristics of GaN for high temperature device modeling," *J. Appl. Phys.*, vol. 83, pp. 4777–4781, 1998.
- [45] N. C. George, K. A. Denault, and R. Seshadri, "Phosphors for Solid-State White Lighting," *Annual Review of Materials Research*, vol. 43, pp. 481–501, 2013.
- [46] O. B. Shchekin, J. E. Epler, T. A. Trottier, T. Margalith, D. A. Steigerwald, M. O. Holcomb, P. S. Martin, and M. R. Krames, "High performance thin-film flip-chip InGaN–GaN light-emitting diodes," *Appl. Phys. Lett.*, vol. 89, p. 071109, 2006.
- [47] Y. Narukawa, M. Ichikawa, D. Sanga, M. Sano, and T. Mukai, "White light emitting diodes with super-high luminous efficacy," *J. Phys. D: Appl. Phys.*, vol. 43, p. 354002, 2010.
- [48] H. Masui, S. Nakamura, S. P. DenBaars, and U. K. Mishra, "Nonpolar and Semipolar III-Nitride Light-Emitting Diodes: Achievements and Challenges," *IEEE T. Electron Dev.*, vol. 57, pp. 88–100, 2010.
- [49] Y. Zhao, S. Tanaka, C.-C. Pan, K. Fujito, D. Feezell, J. S. Speck, S. P. DenBaars, and S. Nakamura, "High-Power Blue-Violet Semipolar ($20\bar{2}1$) InGaN/GaN Light-Emitting Diodes with Low Efficiency Droop at 200 A/cm²," *Appl. Phys. Express*, vol. 4, p. 082104, 2011.
- [50] Y. Kawaguchi, C.-Y. Huang, Y.-R. Wu, Q. Yan, C.-C. Pan, Y. Zhao, S. Tanaka, K. Fujito, D. Feezell, C. G. V. de Walle, S. P. DenBaars, and S. Nakamura, "Influence of polarity on carrier transport in semipolar ($20\bar{2}1$) and ($20\bar{2}\bar{1}$) multiple-quantum-well light-emitting diodes," *Appl. Phys. Lett.*, vol. 100, p. 231110, 2012.
- [51] Y. Zhao, Q. Yan, C.-Y. H. S.-C. Huang, P. S. Hsu, S. Tanaka, C.-C. Pan, Y. Kawaguchi, K. Fujito, C. G. V. de Walle, J. S. Speck, S. P. DenBaars, S. Nakamura, and D. Feezell, "Indium incorporation and emission properties of nonpolar and semipolar InGaN quantum wells," *Appl. Phys. Lett.*, vol. 100, p. 201108, 2012.
- [52] K. F. Brennan, *The Physics of Semiconductors with applications to optoelectronic devices*. Cambridge University Press, Cambridge, 1999.
- [53] S.-C. Ling, T.-C. Lu, S.-P. Chang, J.-R. Chen, H.-C. Kuo, and S.-C. Wang, "Low efficiency droop in blue-green m-plane InGaN/GaN light emitting diodes," *Appl. Phys. Lett.*, vol. 96, p. 231101, 2010.

- [54] K. A. Bulashevich, V. F. Mymrin, S. Y. Karpov, I. A. Zhmakin, and A. I. Zhmakin, "Simulation of visible and ultra-violet group-III nitride light emitting diodes," *J. Comput. Phys.*, vol. 213, pp. 214–238, 2006.
- [55] F. Bernardini, V. Fiorentini, and D. Vanderbilt, "Spontaneous polarization and piezoelectric constants of III-V nitrides," *Phys. Rev. B*, vol. 56, p. R10024, 1997.
- [56] F. Bernardini and V. Fiorentini, "Nonlinear macroscopic polarization in III-V nitride alloys," *Phys. Rev. B*, vol. 64, p. 085207, 2001.
- [57] V. Fiorentini, F. Bernardini, and O. Ambacher, "Evidence for nonlinear macroscopic polarization in III-V nitride alloy heterostructures," *Appl. Phys. Lett.*, vol. 80, pp. 1204–1206, 2002.
- [58] H. Zhang, E. J. Miller, E. T. Yu, C. Poblenz, and J. S. Speck, "Measurement of polarization charge and conduction-band offset at $\text{In}_x\text{Ga}_{1-x}\text{N}/\text{GaN}$ heterojunction interfaces," *Appl. Phys. Lett.*, vol. 84, pp. 4644–4646, 2004.
- [59] W. S. Yan, R. Zhang, Z. L. Xie, X. Q. Xiu, P. Han, H. Lu, P. Chen, S. L. Gu, Y. Shi, Y. D. Zheng, and Z. G. Liu, "A thermodynamic model and estimation of the experimental value of spontaneous polarization in a wurtzite GaN," *Appl. Phys. Lett.*, vol. 94, p. 042106, 2009.
- [60] J. Piprek and Z. M. S. Li, "Sensitivity analysis of electron leakage in III-nitride light-emitting diodes," *Appl. Phys. Lett.*, vol. 102, p. 131103, 2013.
- [61] Y.-K. Kuo, Y.-H. Chen, J.-Y. Chang, and M.-C. Tsai, "Numerical analysis on the effects of bandgap energy and polarization of electron blocking layer in near-ultraviolet light-emitting diodes," *Appl. Phys. Lett.*, vol. 100, p. 043513, 2012.
- [62] J. Pal, G. Tse, V. Haxha, and M. A. Migliorato, "Second-order piezoelectricity in wurtzite III-N semiconductors," *Phys. Rev. B*, vol. 84, p. 085211, 2011.
- [63] J. Piprek and Z. M. S. Li, "Origin of InGaN light-emitting diode efficiency improvements using chirped AlGaN multi-quantum barriers," *Appl. Phys. Lett.*, vol. 102, p. 023510, 2013.
- [64] C. Jacoboni and L. Reggiani, "The Monte Carlo method for the solution of charge transport in semiconductors with applications to covalent materials," *Rev. Mod. Phys.*, vol. 55, pp. 645–705, 1983.
- [65] C. Jacoboni and P. Lugli, *The Monte Carlo Method for Semiconductor Device Simulation*. Springer-Verlag, Wien, 1989.
- [66] T. Sadi, *Electrothermal Monte Carlo Simulation of Heterostructure Field-Effect Transistors*. PhD thesis, The University of Leeds, 2007.
- [67] B. K. Ridley, *Quantum Processes in Semiconductors*. Clarendon Press, Oxford, 1999.
- [68] M. Lindberg and S. W. Koch, "Effective Bloch equations for semiconductors," *Phys. Rev. B*, vol. 38, p. 3342, 1988.

- [69] M. Kira, F. Jahnke, S. W. Koch, J. D. Berger, D. V. Wick, T. R. N. Jr., G. Khlitrova, and H. M. Gibbs, "Quantum Theory of Nonlinear Semiconductor Microcavity Luminescence Explaining "Boser" Experiments," *Phys. Rev. Lett.*, vol. 79, p. 5170, 1997.
- [70] M. Kira and S. W. Koch, *Semiconductor Quantum Optics*. Cambridge University Press, 2012.
- [71] O. Heikkilä, J. Oksanen, and J. Tulkki, "Ultimate limit and temperature dependency of light-emitting diode efficiency," *J. Appl. Phys.*, vol. 105, p. 093119, 2009.
- [72] J. Singh, *Semiconductor Devices. An Introduction*. McGraw-Hill, Inc., 1994.
- [73] Y. C. Shen, G. O. Mueller, S. Watanabe, N. F. Gardner, A. Munkholm, and M. R. Krames, "Auger recombination in InGaN measured by photoluminescence," *Appl. Phys. Lett.*, vol. 91, p. 141101, 2007.
- [74] A. Dmitriev and A. Oruzhenikov, "The rate of radiative recombination in the nitride semiconductors and alloys," *J. Appl. Phys.*, vol. 86, pp. 3241–3246, 1999.
- [75] W. G. Scheibenzuber, U. T. Schwarz, L. Sulmoni, J. Dorsaz, J.-F. Carlin, and N. Grandjean, "Recombination coefficients in GaN-based laser diodes," *J. Appl. Phys.*, vol. 109, p. 093106, 2011.
- [76] J. Hader, J. V. Moloney, and S. W. Koch, "Suppression of carrier recombination in semiconductor lasers by phase-space filling," *Appl. Phys. Lett.*, vol. 87, p. 201112, 2005.
- [77] J. Hader, J. V. Moloney, and S. W. Koch, "Beyond the ABC: carrier recombination in semiconductor lasers," *Proc. SPIE*, vol. 6115, p. 61151T, 2006.
- [78] W. Chow, M. Kira, and S. W. Koch, "Microscopic theory of optical nonlinearities and spontaneous emission lifetime in group-III nitride quantum wells," *Phys. Rev. B*, vol. 60, p. 1947, 1999.
- [79] W. Shockley and J. W. T. Read, "Statistics of the Recombinations of Holes and Electrons," *Phys. Rev.*, vol. 87, pp. 835–842, 1952.
- [80] R. N. Hall, "Electron-Hole Recombination in Germanium," *Phys. Rev.*, vol. 87, p. 387, 1952.
- [81] M. Meneghini, N. Trivellin, G. Meneghesso, E. Zanoni, U. Zehnder, and B. Hahn, "A combined electro-optical method for the determination of the recombination parameters in InGaN-based light-emitting diodes," *J. Appl. Phys.*, vol. 106, p. 114508, 2009.
- [82] A. Haug, "Phonon-Assisted Auger Recombination in Quantum Well Semiconductors," *Appl. Phys. A*, vol. 51, pp. 354–356, 1990.
- [83] K. T. Delaney, P. Rinke, and C. G. V. de Walle, "Auger recombination rates in nitrides from first principles," *Appl. Phys. Lett.*, vol. 94, p. 191109, 2009.
- [84] M. Zhang, P. Bhattacharya, J. Singh, and J. Hinckley, "Direct measurement of auger recombination in $\text{In}_{0.1}\text{Ga}_{0.9}\text{N}/\text{GaN}$ quantum wells and its impact on the efficiency of $\text{In}_{0.1}\text{Ga}_{0.9}\text{N}/\text{GaN}$ multiple quantum well light emitting diodes," *Appl. Phys. Lett.*, vol. 95, p. 201108, 2009.

- [85] A. David and M. J. Grundmann, "Influence of polarization fields on carrier lifetime and recombination rates in InGaN-based light-emitting diodes," *Appl. Phys. Lett.*, vol. 97, p. 033501, 2010.
- [86] J.-I. Shim, "Active Region Part B. Internal Quantum Efficiency," in *III-Nitride Based Light Emitting Diodes and Applications*, pp. 153–195, Springer, 2013.
- [87] O. Heikkilä, J. Oksanen, and J. Tulkki, "The challenge of unity wall plug efficiency: The effects of internal heating on the efficiency of light emitting diodes," *J. Appl. Phys.*, vol. 107, p. 033105, 2010.
- [88] P. Santhanam, D. J. G. Jr., and R. J. Ram, "Thermoelectrically Pumped Light-Emitting Diodes Operating above Unity Efficiency," *Phys. Rev. Lett.*, vol. 108, p. 097403, 2012.
- [89] F. Bertazzi, M. Goano, X. Zhou, M. Calciati, G. Ghione, M. Matsubara, and E. Bellotti, "Comment on "Direct Measurement of Auger Electrons Emitted from a Semiconductor Light-Emitting Diode under Electrical Injection: Identification of the Dominant Mechanism for Efficiency Droop","" *arXiv:1305.2512v3*, 2013.
- [90] J. Hader, J. V. Moloney, and S. W. Koch, "Microscopic many-body investigation of the efficiency droop in GaN based light emitting devices," *Proc. SPIE*, vol. 9003, p. 900311, 2014.
- [91] G.-B. Lin, D. Meyaard, J. Cho, E. F. Schubert, H. Shim, and C. Sone, "Analytic model for the efficiency droop in semiconductors with asymmetric carrier-transport properties based on drift-induced reduction of injection efficiency," *Appl. Phys. Lett.*, vol. 100, p. 161106, 2012.
- [92] Y.-K. Kuo, M.-C. Tsai, and S.-H. Yen, "Numerical simulation of blue InGaN light-emitting diodes with polarization-matched AlGaInN electron-blocking layer and barrier layer," *Opt. Commun.*, vol. 282, pp. 4252–4255, 2009.
- [93] C.-T. Liao, M.-C. Tsai, B.-T. Liou, S.-H. Yen, and Y.-K. Kuo, "Improvement in output power of a 460nm InGaN light-emitting diode using staggered quantum well," *J. Appl. Phys.*, vol. 108, p. 063107, 2010.
- [94] A. David, M. J. Grundmann, J. F. Kaeding, N. F. Gardner, T. G. Mihopoulos, and M. R. Krames, "Carrier distribution in (0001)InGaN/GaN multiple quantum well light-emitting diodes," *Appl. Phys. Lett.*, vol. 92, p. 053502, 2008.
- [95] J.-W. Shi, C.-C. Chen, C.-K. Wang, C.-S. Lin, J.-K. Sheu, W.-C. Lai, C.-H. Kuo, C.-J. Tun, T.-H. Yang, F.-C. Tsao, and J.-I. Chyi, "Phosphor-Free GaN-Based Transverse Junction White-Light Light-Emitting Diodes With Regrown n-Type Regions," *IEEE Photon. Technol. Lett.*, vol. 20, pp. 449–451, 2008.
- [96] J.-W. Shi, S.-H. Guol, C.-S. Lin, J.-K. Sheu, K.-H. Chang, W.-C. Lai, C.-H. Kuo, C.-J. Tun, , and J.-I. Chyi, "The Structure of GaN-Based Transverse Junction Blue LED Array for Uniform Distribution of Injected Current/Carriers," *IEEE J. Sel. Top. Quantum Electron.*, vol. 15, pp. 1292–1297, 2009.

- [97] S. Watanabe, N. Yamada, M. Nagashima, Y. Ueki, C. Sasaki, Y. Yamada, T. Taguchi, K. Tadatomo, H. Okagawa, and H. Kudo, "Internal quantum efficiency of highly efficient $\text{In}_x\text{Ga}_{1-x}\text{N}$ based near-ultraviolet light-emitting diodes," *Appl. Phys. Lett.*, vol. 83, pp. 4906–4908, 2003.
- [98] G. Chen, M. Craven, A. Kim, A. Munkholm, S. Watanabe, M. Camras, W. Götz, and F. Steranka, "Performance of high-power III-nitride light-emitting diodes," *Phys. Status Solidi A*, vol. 205, pp. 1086–1092, 2008.
- [99] A. Getty, E. Matioli, M. Iza, C. Weisbuch, and J. S. Speck, "Electroluminescent measurement of the internal quantum efficiency of light emitting diodes," *Appl. Phys. Lett.*, vol. 94, p. 181102, 2009.
- [100] E. Matioli and C. Weisbuch, "Direct measurement of internal quantum efficiency in light emitting diodes under electrical injection," *J. Appl. Phys.*, vol. 109, p. 073114, 2011.
- [101] Q. Dai, M. F. Schubert, M. H. Kim, J. K. Kim, E. F. Schubert, D. D. Koleske, M. H. Crawford, S. R. Lee, A. J. Fischer, G. Thaler, and M. A. Banas, "Internal quantum efficiency and nonradiative recombination coefficient of GaInN/GaN multiple quantum wells with different dislocation densities," *Appl. Phys. Lett.*, vol. 94, p. 111109, 2009.
- [102] R.-C. Tu, C.-C. Chuo, S.-M. Pan, Y.-M. Fan, C.-E. Tsai, T.-C. Wang, C.-J. Tun, G.-C. Chi, B.-C. Lee, and C.-P. Lee, "Improvement of near-ultraviolet InGaN/GaN light-emitting diodes by inserting an in situ rough SiN_x interlayer in n-GaN layers," *Appl. Phys. Lett.*, vol. 83, pp. 3608–3610, 2003.
- [103] J. Wallentin, N. Anttu, D. Asoli, M. Huffman, I. Åberg, M. H. Magnusson, G. Siefert, P. Fuss-Keiluweit, F. Dimroth, B. Witzigmann, H. Q. Xu, L. Samuelson, K. Deppert, and M. T. Borgström, "InP Nanowire Array Solar Cells Achieving 13.8% Efficiency by Exceeding the Ray Optics Limit," *Science*, vol. 339, pp. 1057–1060, 2013.
- [104] W. Guo, M. Zhang, P. Bhattacharya, and J. Heo, "Auger Recombination in III-Nitride Nanowires and Its Effect on Nanowire Light-Emitting Diode Characteristics," *Nano Lett.*, vol. 11, pp. 1434–1438, 2011.
- [105] H. P. T. Nguyen, S. Zhang, K. Cui, X. Han, S. Fatholouloumi, M. Couillard, G. A. Botton, and Z. Mi, "p-Type Modulation Doped InGaN/GaN Dot-in-a-Wire White-Light-Emitting Diodes Monolithically Grown on Si(111)," *Nano Lett.*, vol. 11, pp. 1919–1924, 2011.
- [106] H. P. T. Nguyen, K. Cui, S. Zhang, M. Djavid, A. Korinek, G. A. Botton, and Z. Mi, "Controlling Electron Overflow in Phosphor-Free InGaN/GaN Nanowire White Light-Emitting Diodes," *Nano Lett.*, vol. 12, pp. 1317–1323, 2012.
- [107] S. D. Carnevale, T. F. Kent, P. J. Phillips, M. J. Mills, S. Rajan, and R. C. Myers, "Polarization-Induced pn Diodes in Wide-Band-Gap Nanowires with Ultraviolet Electroluminescence," *Nano Lett.*, vol. 12, pp. 915–920, 2012.
- [108] E. Homeyer, P. Mattila, J. Oksanen, T. Sadi, H. Nykänen, S. Suihkonen, C. Symonds, J. Tulkki, F. Tuomisto, M. Sopanen, and J. Bellessa, "Enhanced light extraction from InGaN/GaN quantum wells with silver gratings," *Appl. Phys. Lett.*, vol. 102, p. 081110, 2013.

- [109] K. Okamoto, I. Niki, A. Shvartser, Y. Narukawa, T. Mukai, and A. Scherer, "Surface-plasmon-enhanced light emitted based on InGaN quantum wells," *Nat. Mater.*, vol. 3, pp. 601–605, 2004.
- [110] T. Sadi, J. Oksanen, and J. Tulkki, "Improving Light Extraction From GaN Light-Emitting Diodes by Buried Nano-Gratings," *IEEE J. Quantum Elect.*, vol. 50, pp. 141–147, 2014.
- [111] J. Singh, *Semiconductor Optoelectronics: Physics and Technology*. McGraw-Hill, New York, 1995.
- [112] J. Simon, A. Wang, H. Xing, S. Rajan, and D. Jena, "Carrier transport and confinement in polarization-induced three-dimensional electron slabs: Importance of alloy scattering in AlGaIn," *Appl. Phys. Lett.*, vol. 88, p. 042109, 2006.
- [113] J. Simon, V. Protasenko, C. Lian, H. Xing, and D. Jena, "Polarization-Induced Hole Doping in Wide-Band-Gap Uniaxial Semiconductor Heterostructures," *Science*, vol. 327, pp. 60–67, 2010.
- [114] S. Li, M. E. Ware, J. Wu, V. P. Kunets, M. Hawkrige, P. Minor, Z. Wang, Z. Wu, Y. Jiang, and G. J. Salamo, "Polarization doping: Reservoir effects of the substrate in AlGaIn graded layers," *J. Appl. Phys.*, vol. 112, p. 053711, 2012.
- [115] S. Li, T. Zhang, J. Wu, Y. Yang, Z. Wang, Z. Wu, Z. Chen, and Y. Jiang, "Polarization induced hole doping in graded Al_xGa_{1-x}In ($x = 0.7 \sim 1$) layer grown by molecular beam epitaxy," *Appl. Phys. Lett.*, vol. 102, p. 062108, 2013.
- [116] J. Verma, S. M. Islam, V. Protasenko, P. K. Kandaswamy, H. Xing, and D. Jena, "Tunnel-injection quantum dot deep-ultraviolet light-emitting diodes with polarization-induced doping in III-nitride heterostructures," *Appl. Phys. Lett.*, vol. 104, p. 021105, 2014.
- [117] S. Li, M. Ware, J. Wu, P. Minor, Z. Wang, Z. Wu, Y. Jiang, and G. J. Salamo, "Polarization induced pn-junction without dopant in graded AlGaIn coherently strained on GaN," *Appl. Phys. Lett.*, vol. 101, p. 122103, 2012.
- [118] S. D. Carnevale, T. F. Kent, P. J. Phillips, A. T. M. G. Sarwar, C. Selcu, R. F. Klie, and R. C. Myers, "Mixed Polarity in Polarization-Induced p–n Junction Nanowire Light-Emitting Diodes," *Nano Lett.*, vol. 13, pp. 3029–3035, 2013.
- [119] O. V. Khokhlev, K. A. Bulashevich, and S. Y. Karpov, "Polarization doping for III-nitride optoelectronics," *Phys. Status Solidi A*, vol. 210, pp. 1369–1376, 2013.



ISBN 978-952-60-5991-4 (printed)
ISBN 978-952-60-5992-1 (pdf)
ISSN-L 1799-4934
ISSN 1799-4934 (printed)
ISSN 1799-4942 (pdf)

Aalto University

Department of Biomedical Engineering and Computational Science

**BUSINESS +
ECONOMY**

**ART +
DESIGN +
ARCHITECTURE**

**SCIENCE +
TECHNOLOGY**

CROSSOVER

**DOCTORAL
DISSERTATIONS**